

# **Modellierung und Analyse von Akkretionsscheiben um kompakte Sterne**

**Zusammenfassung zur kumulativen Habilitation  
zur Erlangung der venia legendi  
für das Fach Astronomie und Astrophysik**

**vorgelegt von**

**Dr. Thorsten Nagel**

Institut für Astronomie und Astrophysik, Abteilung Astronomie  
Kepler Center for Astro and Particle Physics  
Fakultät für Mathematik und Physik  
Eberhard Karls Universität Tübingen

Tübingen, 2010



# Inhaltsverzeichnis

1 Einleitung	7
2 Akkretionsscheibenmodelle	11
3 Akkretionsscheiben in Binärsystemen	17
3.1 Kataklysmische Variable . . . . .	17
3.2 AM CVn Sterne . . . . .	26
3.3 Ultrakompakte Röntgendoppelsterne . . . . .	29
4 Akkretionsscheiben um Einzelsterne	33
4.1 Supernova-Fallback-Scheiben . . . . .	33
4.2 Debris-Scheiben um Weiße Zwerge . . . . .	35
5 Zusammenfassung und Ausblick	39
Literaturverzeichnis	41
Publikationsliste	47
A Accretion disk spectra for the dwarf nova SS Cygni	53
B Accretion-disk models for AM CVn systems	63
C Accretion disks in two ultra-compact X-ray binaries	73
D Non-LTE modeling of supernova-fallback disks	83
E Gaseous metal disks around DAZ white dwarfs	93



# Abbildungsverzeichnis

2.1	Radialer Verlauf der Effektivtemperatur in der Akkretionsscheibe . . . . .	12
2.2	Berechnete Spektren von vier Akkretionsscheibenringen in verschiedenen Abständen zum Primärstern . . . . .	15
2.3	Abhängigkeit des Linienprofils vom Inklinationswinkel . . . . .	16
3.1	Äquipotentialflächen im Rochepotential eines Doppelsternsystems . . . . .	18
3.2	Hertzsprung-Russell-Diagramm . . . . .	20
3.3	Künstlerische Darstellung eines kataklysmischen Variablen . . . . .	21
3.4	Darstellung des Verlaufs eines Zergnovaausbruchs . . . . .	24
3.5	Vergleich eines beobachteten Spektrums von CE 315 und zweier Modellspektren . . . . .	27
3.6	Vergleich eines beobachteten Spektrums von AM CVn und eines Modellspektrums . . . . .	28
3.7	Beobachtete Spektren der UCXB 4U 0614+091 und 4U 1626-67 . . . . .	30
4.1	Supernova SN 1987A . . . . .	34
4.2	Vergleich zweier Modellspektren eines Scheibenringes mit einem Schwarzkörperspektrum . . . . .	35
4.3	Vergleich eines Modellspektrums mit einem beobachteten Spektrum von SDSS J1228+1040 . . . . .	37



# Kapitel 1

## Einleitung

Akkretionsscheiben sind ein astrophysikalisches Phänomen, das in vielfältiger Form im Universum auftritt. So findet man Akkretionsscheiben beispielsweise am Beginn der Sternentstehung, wenn sich in einer Molekülwolke ein Protostern bildet. Diese Wolken bestehen aus Gas und Staub<sup>1</sup>, haben eine typische Ausdehnung von mehreren dutzend bis einigen hundert Lichtjahren<sup>2</sup> und Massen von einigen tausend bis Millionen Sonnenmassen<sup>3</sup>. Reichen die thermischen und magnetischen Druckkräfte in der Wolke nicht mehr aus, die nach innen gerichtete Schwerkraft zu kompensieren, kontrahiert die Wolke und fragmentiert. Druck und Temperatur in den kollabierenden Fragmenten steigen an, in ihren Zentren bilden sich Protosterne, deren Masse stetig wächst. Sind Temperatur und Druck hinreichend hoch, stellt sich ein Gleichgewicht zwischen Schwerkraft und thermischem Druck ein, der Kollaps wird unterbrochen. Das weiterhin aus der Molekülwolke einfallende Material sammelt sich um den Protostern in einer Akkretionsscheibe. In dieser sog. protoplanetaren Scheibe entwickelt sich innerhalb einiger Millionen Jahre ein Planetensystem. Der Protostern kontrahiert unterdessen weiter, bis in seinem Zentrum die Zündtemperatur für die Wasserstofffusion von etwa 10 Millionen Kelvin erreicht ist. Mit dem Einsetzen der Fusion von Wasserstoff zu Helium ist der ehemalige Protostern zu einem vollwertigen Stern geworden (siehe z.B. Kippenhahn & Weigert 1994). Sowohl protoplanetare Scheiben als auch extrasolare Planetensysteme wurden inzwischen vielfach entdeckt.

Akkretionsscheiben einer ganz anderen Größenordnung findet man in den Zentren von aktiven Galaxien<sup>4</sup>. Hierbei akkretieren supermassive Schwarze Löcher mit  $10^6 - 10^9$  Sonnenmassen Materie aus der sie umgebenden Akkretionsscheibe (z.B. Peterson 1997). Die bei der Akkretion stattfindende Umwandlung von gravitativer in thermische Energie ist neben der Kernfusion der effektivste Energiegewinnungs-

<sup>1</sup>Die wesentlichen Bestandteile von *Molekülwolken* sind neutraler und molekularer Wasserstoff, sowie Helium und zu einem geringen Teil schwerere Elemente und Moleküle, z.B. CO.

<sup>2</sup>Ein *Lichtjahr* ist die Strecke, die das Licht innerhalb eines Jahres zurücklegt, dies sind etwa  $9,461 \cdot 10^{15}$  m.

<sup>3</sup>Die *Masse*  $M_{\odot}$  *unserer Sonne* beträgt etwa  $1,9891 \cdot 10^{33}$  kg.

<sup>4</sup>active galactic nuclei AGN

mechanismus. Aktive Galaxien gehören dadurch zu den leuchtkräftigsten Objekten im Universum.

In engen Doppelsternsystemen spielen Akkretionsscheiben eine zentrale Rolle und zeichnen für eine Vielzahl von Phänomenen verantwortlich. So werden beispielsweise Zwergnovae einem plötzlichen Temperatur- und damit Helligkeitsanstieg der Akkretionsscheibe eines kataklysmischen Variablen zugeschrieben (siehe z.B. Warner 1995; Hellier 2001). Auch Novae und periodische oder quasi-periodische Helligkeitsschwankungen auf verschiedenen Zeitskalen hängen direkt oder indirekt mit Akkretionsscheiben in diesen Systemen zusammen, ebenso die zur kosmologischen Entfernungsmessung verwendeten Supernovae vom Typ Ia. In Kap. 3 werde ich auf die Entstehung und Eigenschaften von kataklysmischen Variablen und den mit ihnen verwandten Röntgendoppelsternen detaillierter eingehen und meine Forschungsergebnisse hierzu vorstellen.

Selbst am Ende des Daseins eines Einzelsterns kann eine Akkretionsscheibe auftreten, wie sich in den letzten Jahren gezeigt hat. Bei massereichen Sternen ist es denkbar, dass sich ein Teil des bei der Supernovaexplosion des Sterns ausgeworfenen Materials um das entstandene kompakte Objekt in Form einer Akkretionsscheibe (Supernova-Fallback-Scheibe) sammelt (siehe z.B. van Paradijs et al. 1995; Chatterjee et al. 2000; Alpar 2001) und möglicherweise verantwortlich ist für beobachtete Röntgenemission oder Pulsationen (siehe Kap. 4.1). Und sogar um einzeln stehende Weiße Zwerge, den Endstadien massearmer Sterne, wurden Staub- und Gassscheiben gefunden (z.B. Gänsicke et al. 2006, 2008; Farihi et al. 2009). Diese sind vermutlich die Überreste von Asteroiden oder anderen Objekten seines ehemaligen Planetensystems, die durch die Gezeitenkraft des Weißen Zerges zerrissen wurden, als sie ihm zu nahe kamen, und sich um den Weißen Zerg gesammelt haben. Erste Ergebnisse meiner Forschungsarbeiten hierzu werde ich in Kap. 4.2 näher ausführen.

Mit dieser Habilitationsschrift möchte ich meine Forschungsarbeit der letzten Jahre, in der ich mich mit Akkretionsscheiben in Doppelsternsystemen und um Einzelsterne beschäftigt habe, zusammenfassend vorstellen. Im Vordergrund meiner Arbeit steht die detaillierte Berechnung eines synthetischen Spektrums der Akkretionsscheibe mit dem Ziel, dies mit Spektren, die mit erdgebundenen Großteleskopen<sup>5</sup> oder Weltraumteleskopen wie z.B. dem Hubble Space Telescope (HST) gewonnen wurden, zu vergleichen. Auf diese Weise versucht man mittels Spektralanalyse möglichst viel über die Entstehung und Entwicklung der untersuchten Objekte zu lernen. Hierzu ist es notwendig, die in einer Akkretionsscheibe ablaufenden, komplexen physikalischen Vorgänge möglichst realistisch zu simulieren. Dies geschieht unter Verwendung des Programmpaketes AcDC, das ich bereits während meiner Doktorarbeit, aufbauend auf bewährten Programmen zur Berechnung von Sternatmosphären, entwickelt habe (Nagel 2003). Im an diese Einleitung anschließenden Kap. 2 werde ich die zu Grunde liegende Methodik genauer vorstellen. Der Vergleich

---

<sup>5</sup>Einige der von mir verwendeten Spektren wurden beispielsweise mit dem Very Large Telescope VLT der ESO in Chile aufgenommen. Dieses Observatorium umfasst vier 8,20 m Spiegelteleskope sowie eine Reihe kleinerer Hilfsteleskope.

des berechneten Spektrums mit dem beobachteten erlaubt es dann, Parameter wie z.B. radiale Ausdehnung und Neigungswinkel der Akkretionsscheibe, Massenakkretionsrate und chemische Zusammensetzung zu bestimmen. Da die chemische Komposition der Akkretionsscheibe im Doppelsternsystem derjenigen der äußeren Schichten des Donorsterns entspricht, ergeben sich so indirekt auch Erkenntnisse bzgl. des oft sehr leuchtschwachen Begleitsterns.

Im Anhang dieser Habilitationsschrift befinden sich meine bzgl. der Modellierung und Analyse von Akkretionsscheiben um kompakte Objekte wichtigsten Veröffentlichungen, auf die ich in den kommenden Kapiteln verweisen werde. Meine Arbeiten entstanden im wesentlichen in Zusammenarbeit mit Dr. Thomas Rauch (Universität Tübingen), der mir die für meine Arbeit unverzichtbaren Modellatome zu Verfügung gestellt hat, sowie Prof. Klaus Werner (Universität Tübingen), der mir mit vielen konstruktiven Diskussionen zur Seite stand. Generell ist mein Anteil an den Veröffentlichungen auf dem Gebiet der Modellierung und Analyse von Akkretionsscheiben um kompakte Objekte als (deutlich) mehr als 50% anzusehen, unabhängig von Erst- oder Zweitautorenschaft.

Neben meiner Forschung zu Akkretionsscheiben um kompakte Objekte habe ich mich in den letzten Jahren auch mit der Suche nach und Untersuchung von veränderlichen, insbesondere pulsierenden Sternen beschäftigt. Als Beobachtungsinstrument kam hierbei das institutseigene 80 cm Spiegelteleskop zum Einsatz. Im Rahmen eigener Projekte gelang z.B. die Entdeckung nicht-radialer Pulsationen in einem neu entdeckten PG 1159 Stern (Nagel & Werner 2004) sowie der Nachweis des ersten engen Doppelsternsystems mit einem PG 1159 Stern (Nagel et al. 2006). Dieses ungewöhnliche Doppelsternpaar ermöglicht erstmals die dynamische Massenbestimmung eines PG 1159 Sternes alternativ zu spektroskopischen oder asteroseismologischen Methoden. Hierzu haben wir im November 2009 zeitaufgelöste Spektren mit dem Very Large Telescope in Chile gewonnen, die nun ausgewertet werden. Des Weiteren habe ich an internationalen Beobachtungskampagnen des Whole Earth Telescope WET<sup>6</sup> teilgenommen (Provencal et al. 2009a,b; Thompson et al. 2010). Das Hauptinteresse liegt hierbei auf der asteroseismologischen Untersuchung pulsierender Weiße Zwerge. Im Rahmen des internationalen Langzeitprojekts EXOTIME<sup>7</sup> tragen unsere Beobachtungen zur Suche nach extrasolaren Planeten um sdB Sterne bei (Schuh et al. 2010). Da diese Arbeiten nur wenig direkten thematischen Bezug zum Inhalt dieser Habilitationsschrift haben, lege ich die entsprechenden Veröffentlichungen separat bei mit der Bitte, sie als Teil meiner Habilitationsleistungen zu berücksichtigen.

---

<sup>6</sup>Das *Whole Earth Telescope WET* ist ein 1986 vom Astronomiedepartment der Universität Texas gegründetes globales Netzwerk von Teleskopen. Die Beobachtung von Objekten durch das WET ermöglicht die Gewinnung unterbrechungsfreier Lichtkurven für eine Zeitdauer von mehreren Wochen und ermöglicht so eine sehr detaillierte Analyse multiperiodischer Sternosillationen. Beobachtungskampagnen des WET werden meist ein- bis zweimal jährlich durchgeführt, die Koordination erfolgt durch das Delaware Asteroseismic Research Center DARC.

<sup>7</sup>Im Rahmen des EXOTIME Projekts werden über viele Jahre hinweg Lichtkurven von pulsierenden sdB Sternen gewonnen, um überlagerte periodische Änderungen, die durch die Anwesenheit eines massearmen Begleiters verursacht werden, zu finden.



# Kapitel 2

## Akkretionsscheibenmodelle

Die Analyse beobachteter Spektren erfordert die Bereitstellung detaillierter, synthetischer Spektren. Die Objekte meiner Forschungsarbeiten lassen sich auf Grund ihrer Kompaktheit räumlich nicht auflösen. Dies führt dazu, dass sich ein beobachtetes Spektrum aus den Spektren mehrerer Komponenten zusammensetzt, beispielsweise der Akkretionsscheibe und des von ihr umgebenen Sterns. Da sich die Komponenten jedoch oft in ihrer Effektivtemperatur<sup>1</sup> unterscheiden, lassen sie sich durch Beobachtung in verschiedenen Wellenlängenbreichen bis zu einem gewissen Grad voneinander trennen<sup>2</sup>.

Die Berechnung der Struktur und des Spektrums einer Akkretionsscheibe unter Berücksichtigung möglichst vieler physikalischer Prozesse ist kompliziert und numerisch enorm aufwändig. Eine detaillierte, dreidimensionale Behandlung des Problems mittels Strahlungshydrodynamik ist wegen der dazu notwendigen Rechnerkapazitäten noch nahezu ausgeschlossen. Die Situation lässt sich jedoch vereinfachen, indem man die Berechnung von Vertikal- und Radialstruktur voneinander entkoppelt. Dies ist möglich im Falle geometrisch dünner (Scheibenhöhe  $H \ll$  Scheibenradius  $R$ ) Akkretionsscheiben, sog. Standard- $\alpha$ -Scheiben (Shakura & Sunyaev 1973). Der radiale Verlauf der Effektivtemperatur  $T_{\text{eff}}$ , dargestellt in Abb. 2.1, lässt sich dann schreiben als:

$$T_{\text{eff}}(R) = \left[ \frac{3GM_1\dot{M}}{8\pi\sigma R^3} \left( 1 - \sqrt{\frac{R_1}{R}} \right) \right]^{1/4}$$

Hierbei bezeichnen  $M_1$  und  $R_1$  Masse und Radius des Zentralobjektes,  $\dot{M}$  die Akkretionsrate,  $G$  die Gravitationskonstante und  $\sigma$  die Stefan-Boltzmann-Konstante. Im nächsten Schritt unterteilt man, unter der Annahme von Axialsymmetrie, die Akkre-

<sup>1</sup>Die *Effektivtemperatur* ist die Temperatur eines schwarzen Körpers mit der gleichen abgestrahlten Energie pro Zeit- und Flächeneinheit. Man kann sie sich grob als Oberflächentemperatur vorstellen.

<sup>2</sup>In einem *kataklysmischen Variablen* (siehe Kap. 3) dominieren der Primärstern meist im UV, die Akkretionsscheibe im optischen und der Sekundärstern im infraroten Spektralbereich.

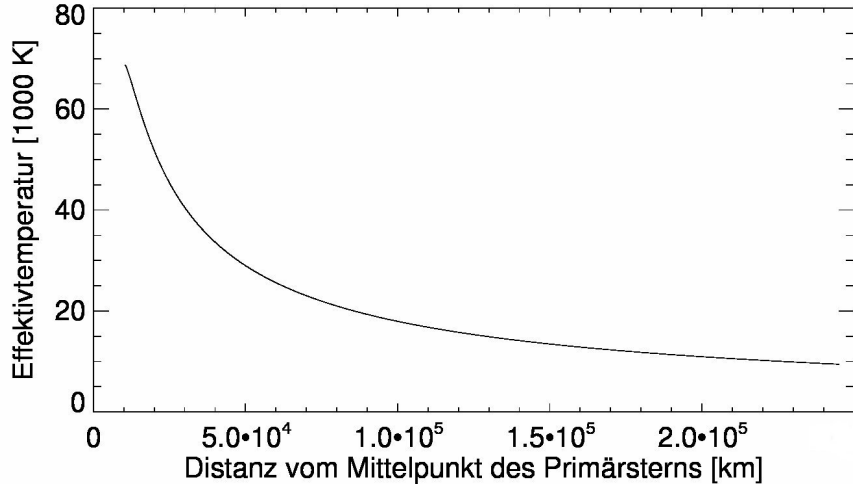


Abbildung 2.1: Radialer Verlauf der Effektivtemperatur in der Akkretionsscheibe bei einem Primärstern mit  $M_1 = 0.8 M_\odot$  und  $R_1 = 7\,000$  km sowie einer Akkretionsrate von  $\dot{M} = 10^{-8} M_\odot/\text{a}$ .

tionsscheibe in einen Satz konzentrischer Ringe<sup>3</sup>, äquidistant bzgl. Unterschieden in der Effektivtemperatur, und berechnet für jeden Scheibenring die Vertikalstruktur und das Spektrum.

In den Anfängen wurden hierfür einfache Sternatmosphärenmodelle, meist von Kurucz (1979), verwendet, so z.B. durch Kiplinger (1979) oder Mayo et al. (1980). Es zeigte sich jedoch bald, dass weder Schwarzkörperspektren noch Modellatmosphären das Spektrum der Akkretionsscheibe eines kataklysmischen Variablen adäquat wiedergeben (Wade 1988). Auch die von Meyer & Meyer-Hofmeister (1982), Cannizzo & Wheeler (1984) oder Cannizzo & Cameron (1988) verwendete Diffusionsnäherung zur Berechnung des Strahlungstransports stellte sich als problematisch heraus, da sich ihre Gültigkeit auf große optische Tiefen ( $\tau \gg 1$ ) beschränkt, die Spektrallinien des Spektrums jedoch in optischen Tiefen  $\tau \approx 1$  entstehen.

Fortschritte wurden erst erzielt, als die modernen Methoden, die inzwischen in die Theorie der Sternatmosphären Einzug gehalten hatten, auch zur Berechnung der Vertikalstruktur und des Strahlungstransports in Akkretionsscheiben von kataklysmischen Variablen (z.B. Kriz & Hubeny 1986; Shaviv & Wehrse 1986, 1989; Diaz et al. 1996; Nasser et al. 2001; Nagel et al. 2004) und aktiven Galaxienkernen (z.B. Störzer et al. 1994; Dörrer et al. 1996; Hubeny & Hubeny 1997) verwendet wurden. Das von mir verwendete und im Rahmen meiner Doktorarbeit entwickelte Programmpaket **ACDC**<sup>4</sup> beruht auf einem bewährten, state-of-the-art Programmpaket zur Berechnung von Sternatmosphärenmodellen (Werner et al. 2003), das erweitert wurde, um den besonderen Eigenschaften einer Akkretionsscheibe Rech-

<sup>3</sup>Abhängig vom Gradienten der Effektivtemperatur werden meist 15-20 Ringe benötigt.

<sup>4</sup>Kurzform für **Accretion Disc Code** (Nagel et al. 2004)

nung zu tragen. Ein wesentlicher Unterschied betrifft die Energiebilanz. Unterteilt man eine Sternatmosphäre bzw. einen Scheibenring vertikal in  $n$  Schichten, dann ist in der Sternatmosphäre der Fluss in jeder Tiefe derselbe (Flusskonstanz). In einer Akkretionsscheibe dagegen ändert sich der Fluss auf Grund viskoser Energieerzeugung. Des Weiteren ist die Oberflächenschwerebeschleunigung in Akkretionsscheiben tiefenabhängig<sup>5</sup>, in planparallelen Sternatmosphären jedoch konstant.

Um die Vertikalstruktur und das Spektrum eines Scheibenringes (siehe Abb. 2.2) zu berechnen ist es notwendig, das folgende System aus gekoppelten Integro- und Differentialgleichungen selbstkonsistent zu lösen:

- Strahlungstransportgleichung, die die Änderung der spezifischen Intensität  $I_\nu$  eines Strahls durch Absorption und Emission, vermittelt durch den Absorptionskoeffizienten  $\kappa_\nu$  (Opazität) und den Emissionskoeffizienten  $\eta_\nu$  (Emissivität), entlang seines Weges  $s$  durch das Plasma beschreibt:

$$\frac{dI_\nu}{ds} = -\kappa_\nu I_\nu + \eta_\nu$$

Die Absorptions- und Emissionskoeffizienten sind hierbei jeweils das Produkt des atomaren Wirkungsquerschnittes mit der Besetzungsichte des absorbiierenden bzw. emittierenden atomaren Niveaus zuzüglich des Beitrages der Thomsonstreuung an freien Elektronen<sup>6</sup> sowie Rayleigh-Streuung für Wasserstoff und Helium.

- Statistische Gleichungen, die im Falle des Non-LTE<sup>7</sup> (NLTE) die zeitliche Änderung der Besetzungsichte  $n_i$  des atomaren Niveaus  $i$  als Summe aller Be- und Entvölkerungsprozesse (durch Strahlung und Stöße verursachte An- und Abregungen sowie Ionisation und Rekombination) mittels der Raten  $P$  beschreiben. Für den statischen Fall gilt:

$$\frac{\partial n_i}{\partial t} = 0 = n_i \sum_{i \neq j} P_{ij} - \sum_{j \neq i} n_j P_{ji}$$

Die Raten  $P$  setzen sich hierbei aus Strahlungs- und Stoßraten zusammen.

---

<sup>5</sup>Ursache der Oberflächenschwerebeschleunigung ist das Gravitationsfeld des Primärsterns. Die Eigengravitation der Akkretionsscheibe wird vernachlässigt, da  $M_{\text{disk}} \ll M_1$ .

<sup>6</sup>Im Falle des Emissionskoeffizienten ist zur Berechnung der Thomsonstreuung die Kenntnis des Strahlungsfeldes  $J_\nu$  notwendig.

<sup>7</sup>Non-LTE bedeutet, dass ich das Plasma nicht im lokalen thermodynamischen Gleichgewicht (LTE) befindet, die Besetzungsahlen der atomaren Niveaus können deshalb nicht durch Lösung der Saha- und Boltzmanngleichungen berechnet werden.

- Hydrostatisches Gleichgewicht, das das Gleichgewicht zwischen Gasdruck, Strahlungsdruck und Schwerkraft beschreibt:

$$\underbrace{\frac{dP_{\text{gas}}}{dm}}_{\text{Gasdruck}} = \underbrace{\frac{G M_1}{R^3} z}_{\text{Schwerkraft}} - \underbrace{\frac{4\pi}{c} \int_0^\infty \frac{\kappa_\nu}{\rho(z)} H_\nu(z) d\nu}_{\text{Strahlungsdruck}}$$

Hierbei bezeichnen  $z$  die geometrische Tiefe,  $dm = -\rho dz$  die Massensäulendichte,  $\rho$  die Dichte und  $H_\nu$  den Eddingtonfluss<sup>8</sup>.

- Energiegleichgewicht zwischen viskos erzeugter Energie  $E_{\text{mech}}$  und abgestrahlter Energie  $E_{\text{rad}}$ , Konvektion wird hierbei vernachlässigt:

$$E_{\text{mech}} = E_{\text{rad}} (+ E_{\text{conv}})$$

wobei

$$E_{\text{mech}} = w \Sigma \left( R \frac{d\omega}{dR} \right)^2 \quad E_{\text{rad}} = 4\pi \int_0^\infty (\eta_\nu - \kappa_\nu J_\nu) d\nu$$

mit der Winkelgeschwindigkeit  $\omega$ , der Flächendichte  $\Sigma$  und der kinematischen Viskosität  $w$ .

- Ladungs- und Teilchenzahlerhaltung

Die Kopplung der Gleichungen erfolgt über das Strahlungsfeld  $J_\nu$ , das über die Strahlungsraten

$$R_{ij} = 4\pi \int_0^\infty \frac{\sigma_{ij}(\nu)}{h\nu} J_\nu d\nu \quad \text{mit } J_\nu = \frac{1}{2} \int_{-1}^1 I_\nu d\mu$$

in die Berechnung der Besetzungszahlen eingeht. Die Besetzungszahlen sind jedoch wiederum Voraussetzung für die Berechnung der Absorptions- und Emissionskoeffizienten, die zur Bestimmung des Strahlungsfeldes benötigt werden. Die Lösung des Gleichungssystems erfolgt deshalb iterativ (Werner et al. 2003). Die einzelnen Scheibenringe werden als voneinander unabhängig und in vertikaler Richtung planparallel angenommen.

Anschließend werden die Spektren der einzelnen Scheibenringe, gewichtet mit ihrem jeweiligen Flächenanteil, zum Gesamtspektrum der Akkretionsscheibe auf integriert. Hierbei wird auch die sich aus der Keplerrotation der Scheibe ergebende Ro-

---

<sup>8</sup>Der *Eddingtonfluss*  $H$  wird auch als das erste Moment der Intensität  $I_\nu$  bezeichnet, es gilt hierbei  $H_\nu = \frac{1}{2} \int_{-1}^1 I_\nu \mu d\mu$ , wobei  $\mu = \cos \theta$  und  $\theta$  der Winkel zwischen Strahlrichtung und Oberflächennormalen ist.

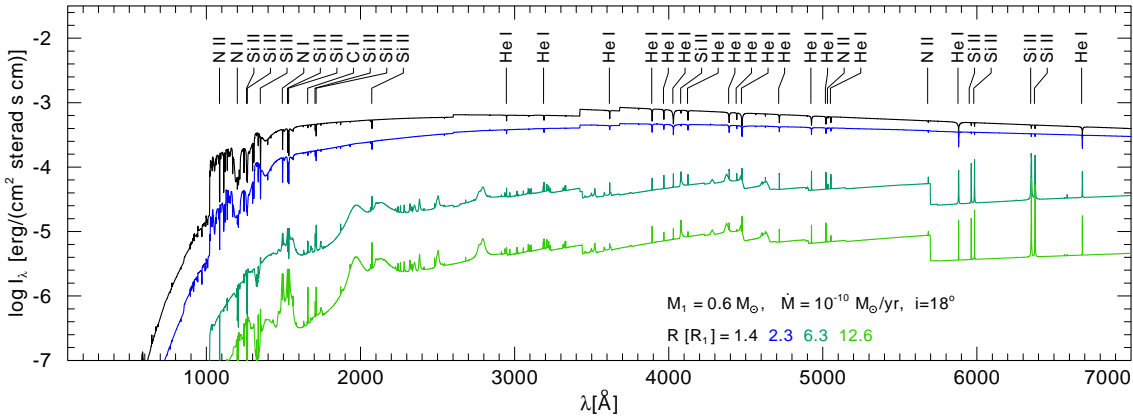


Abbildung 2.2: Berechnete Spektren von vier Akkretionsscheibenringen in verschiedenen Abständen zum Primärstern. Deutlich zu erkennen ist der Übergang von einem Absorptionslinienspektrum der inneren, heißen Ringe zu einem Emissionslinienspektrum im Falle der äußeren, kalten Ringe (Nagel et al. 2009, siehe Anhang B).

tationsverbreiterung berücksichtigt, die, abhängig vom Inklinationswinkel<sup>9</sup>, zu den typischen Doppelhöckern der Spektrallinien führt (siehe Abb. 2.3). Einstrahlung des Zentralobjekts auf die Akkretionsscheibe, sowohl in Form eines Schwarzkörperspektrums als auch eines speziell für das Zentralobjekt berechneten synthetischen Spektrums, kann ebenso berücksichtigt werden wie ein mitrotierender „heißer Fleck“<sup>10</sup>.

Um diese Berechnungen durchführen zu können, muss eine gewisse Anzahl an Inputparametern vorgegeben werden. Dies sind Masse  $M_1$  und Radius  $R_1$  des Zentralobjekts, Akkretionsrate  $\dot{M}$ , Reynoldszahl  $Re$  zur Beschreibung der Viskosität<sup>11</sup> sowie die chemischen Häufigkeiten der zu berücksichtigenden Elemente. Für Masse und Radius des Zentralobjektes werden, falls noch nichts genauereres bekannt ist, als

<sup>9</sup>Der *Inklinationswinkel* ist der Neigungswinkel, unter dem der Beobachter die Akkretionsscheibe sieht.  $0^\circ$  Inklination bedeutet, man blickt von oben (face-on) auf die Akkretionsscheibe, bei  $90^\circ$  Inklination blickt man auf die Kante (edge-on).

<sup>10</sup>Der *heisse Fleck* ist die Kollisionsregion des vom Sekundärsterns überströmenden Materiestroms mit der Akkretionsscheibe in einem kataklysmischen Variablen, siehe Kap. 3.

<sup>11</sup>Bei der in Akkretionsscheiben vorliegenden Viskosität handelt es sich nicht um die aus dem Alltag bekannte molekulare Viskosität, die z.B. das zähe Zerfließen des Honigs verursacht, sondern um ein Turbulenz-Phänomen, das durch die Wechselwirkung elektrisch geladener Teilchen mit schwachen Magnetfeldern hervorgerufen wird, der sog. *Balbus-Hawley-Instabilität* (Hawley & Balbus 1998) oder *Magnetorotationsinstabilität (MRI)*. Die differentielle Rotation der Akkretionsscheibe bewirkt eine Scherung des in der Scheibe vorliegenden, schwachen Magnetfeldes. Durch Kopplung des Magnetfeldes an die Materie werden die radial inneren Regionen abgebremst und die äußeren beschleunigt. Dadurch wird Drehimpuls in Richtung des Außenrandes der Akkretionsscheibe transportiert, während die Materie, die Drehimpuls abgegeben hat, nach innen auf den Primärstern zufließt.

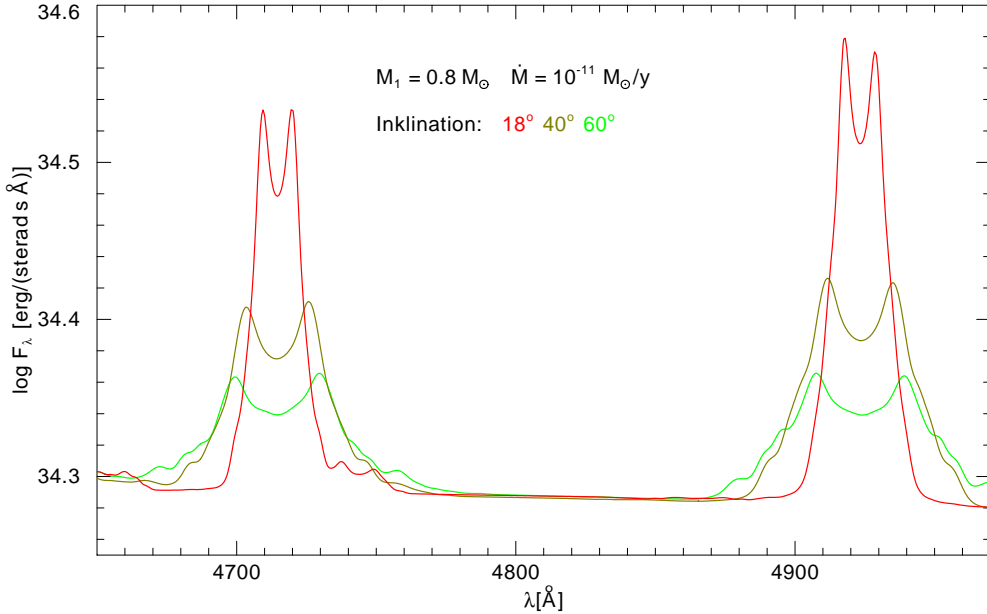


Abbildung 2.3: Abhangigkeit des Linienprofils vom Inklinationswinkel am Beispiel zweier He I Linien. Entsprechend des radialen Anteils der Keplerrotation werden die Spektrallinien dopplerverschoben. Da das Objekt raumlich nicht aufgelost ist, uberlagern sich die blau- und rotverschobenen sowie die nicht-verschobenen Anteile und resultieren in einem charakteristischen Doppelhockerprofil. Mit zunehmendem Inklinationswinkel werden die rotationsverbreiterten Spektrallinien breiter und flacher, die projizierte Radialgeschwindigkeit wird groer.

Startwerte kanonische Werte verwendet ( $0.6 M_\odot$  fur Weie Zwerge,  $1.4 M_\odot$  fur Neutronensterne), eine erste Nherung fr die Akkretionsrate folgt aus der Helligkeit des Objektes. Fr die chemische Zusammensetzung liefert ein erster Blick auf ein beobachtetes Spektrum sowie die vermutliche Entstehungsgeschichte des Systems einen ersten Anhaltspunkt. Durch den Vergleich mit einem beobachteten Spektrum konnen dann im Rahmen einer detaillierten Spektralanalyse sowohl diese Parameter prazisiert als auch beispielsweise die radiale Ausdehnung der Akkretionsscheibe und der Inklinationswinkel bestimmt werden. Eine eingehendere Beschreibung der Methodik und der Umsetzung im Programm paket AcDC findet sich in Nagel (2003) und Nagel et al. (2004).

# Kapitel 3

## Akkretionsscheiben in Binärsystemen

### 3.1 Kataklysmische Variable

Kataklysmische Variable (CV) sind enge Doppelsternsysteme, bei denen Materie von einem Stern auf den anderen überströmt<sup>1</sup>. Ihre Orbitalperioden bewegen sich im Allgemeinen zwischen 78 Minuten und einigen Stunden, wobei in einem Bereich von  $P_{\text{orb}} = 2\text{-}3 \text{ h}$  nur sehr wenige Systeme anzutreffen sind. Im folgenden werde ich auf die Entstehung und Entwicklung kataklysmischer Variabler und einige ihrer Eigenschaften näher eingehen. Eine detaillierte Beschreibung aller damit zusammenhängenden Phänomene würde den Rahmen dieser Arbeit jedoch sprengen, deshalb verweise ich für einen tieferen Einblick auf weiterführende Literatur wie z.B. Warner (1995) oder Hellier (2001), die auch diesem Abschnitt zugrunde liegt.

Am Anfang der Entwicklung eines kataklysmischen Variablen steht ein weites Doppelsternsystem, bei dem die beiden Komponenten einige hundert Sonnenradien voneinander getrennt sind und eine Orbitalperiode von größtenteils 10 Jahren besitzen. Berücksichtigt man die Gravitationspotentiale beider Sterne mit den Massen  $M_1$  und  $M_2$  und das Zentrifugalfeld, verursacht durch die Rotation, lässt sich im mitrotierenden Koordinatensystem das sog. Roche-Potential  $\Phi_R$  schreiben als

$$\Phi_R(\vec{r}) = -\frac{GM_1}{|\vec{r} - \vec{r}_1|} - \frac{GM_2}{|\vec{r} - \vec{r}_2|} - \frac{1}{2} (\vec{\omega} \times \vec{r})^2$$

Hierbei bezeichnen  $\vec{r}_1$  und  $\vec{r}_2$  die Position der Sterne und  $\vec{\omega}$  die Winkelgeschwindigkeit. Eine für kataklysmische Variable entscheidende Rolle spielt hierbei die daraus ableitbare erste gemeinsame Äquipotentialfläche (siehe Abb. 3.1), sie definiert das jeweilige Rochevolumen (Roche Lobe) beider Sterne. Für den Radius  $R_{\text{RV}}$  einer Kugel, deren Volumen dem Rochevolumen des Sekundärsterns entspricht, lässt sich

<sup>1</sup>griech. *κατακλυσμός*: Überschwemmung

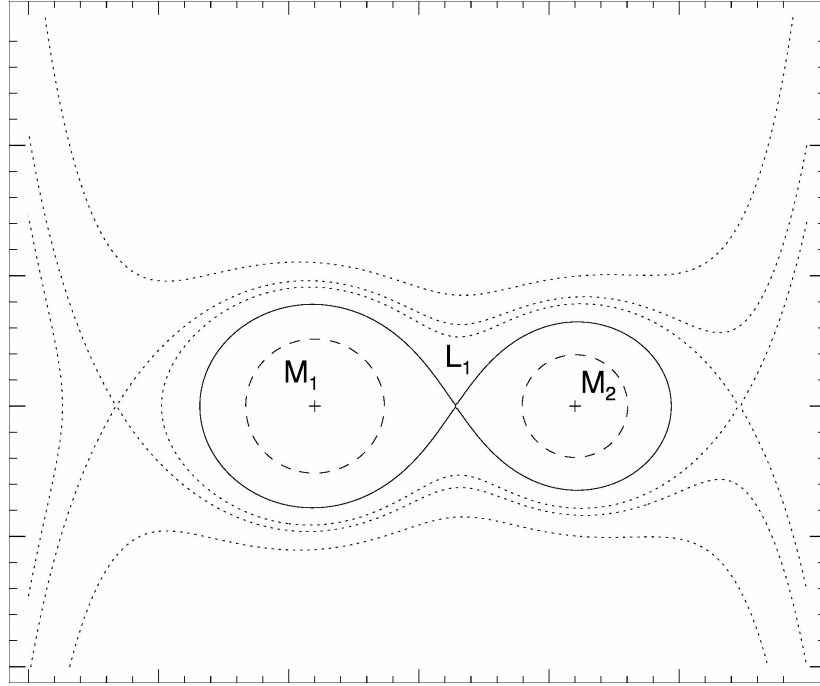


Abbildung 3.1: Äquipotentialflächen im Roche-Potential eines Doppelsternsystems mit Massenverhältnis  $q = M_2/M_1 = 0,6$ . Die durchgezogene Linie kennzeichnet die erste gemeinsame Äquipotentialfläche, ihr Schnittpunkt ist der Lagrangepunkt  $L_1$ .

(Warner 1995) schreiben

$$R_{\text{RV}} = a \cdot 0,462 \left( \frac{q}{1+q} \right)$$

wobei  $a$  die Separation beider Sterne und  $q = M_2/M_1$  das Massenverhältnis bezeichnen.

In einem weiten Doppelsternsystem verläuft die Entwicklung beider Sternkomponenten zunächst unabhängig voneinander ab<sup>2</sup>. Beide Sterne fusionieren in ihrem Kern Wasserstoff zu Helium. Bei Sternmassen von mehr als  $\approx 2 M_\odot$  geschieht dies über den sog. CNO-Zyklus<sup>3</sup>, bei geringerer Sternmasse über die pp-Ketten. Man spricht hierbei vom Hauptreihenstadium. Trägt man Sterne anhand ihrer Effektivtemperatur  $T_{\text{eff}}$  und Leuchtkraft  $L$  in ein Hertzsprung-Russell-Diagramm<sup>4</sup> ein (sie-

<sup>2</sup>Für einen detaillierten Einblick in die *Theorie der Sternentwicklung* möchte ich auf weiterführende Literatur wie z.B. Kippenhahn & Weigert (1994) verweisen.

<sup>3</sup>Beim CNO-Zyklus dienen die Elemente Kohlenstoff, Stickstoff und Sauerstoff als Katalysator bei der Wasserstofffusion.

<sup>4</sup>Das *Hertzsprung-Russell-Diagramm* (HRD) wurde Anfang des 20. Jhd. von Henry Norris Russell und Ejnar Hertzsprung entwickelt und ist inzwischen eines der fundamentalen Diagramme der Astrophysik. Meist wird dabei die absolute Helligkeit in  $y$  über den Spektraltyp in  $x$  aufgetragen. Dies führt zu einer nach links zunehmenden Temperatur auf der  $x$ -Achse. Alternativ lässt sich

he Abb. 3.2), befinden sich Sterne dieses Stadiums auf einer Diagonalen, die als Hauptreihe bezeichnet wird.

Der massereichere<sup>5</sup> Stern (im folgenden als Primärstern bezeichnet) entwickelt sich entsprechend der Theorie der Sternentwicklung zuerst. Nachdem der Wasserstoffvorrat im Kern erschöpft ist, verlagert sich die Wasserstofffusion in eine Brennschale um den Kern. Der Kern selbst, seiner Energiequelle beraubt, kontrahiert, während die Sternhülle expandiert. Der Stern beendet sein Hauptreihenstadium und wird zu einem Roten Riesen mit einem Durchmesser von einigen hundert Sonnenradien, im HRD wandert er jetzt nach rechts oben. Im kontrahierenden Kern steigen Druck und Temperatur an.

Besitzt der Stern mindestens eine Masse von  $0,4 M_{\odot}$ <sup>6</sup>, setzt bei etwa  $10^8$  K die Heliumfusion ein<sup>7</sup>, der Stern befindet sich jetzt auf dem Horizontalast. Mit dem Ende der zentralen Heliumfusion verlagert sich die Energiegewinnung in zwei Wasserstoff und Helium fusionierende Schalen, der Kern kontrahiert erneut bei gleichzeitiger Expansion der Hülle. Der Stern entwickelt sich wiederum zum Roten Riesen, dieses Mal entlang des asymptotischen Riesenastes im HRD.

Im Riesenstadium füllt der Primärstern sein Rochevolumen aus, seine äußere Hülle wird über den Lagrangepunkt  $L_1$  auf den Begleitstern transferiert. Da sich das Material weg vom Massenzentrum des Binärsystems bewegt, gewinnt es Drehimpuls. Die Separation der beiden Sterne nimmt infolgedessen etwas ab, damit der Gesamt-drehimpuls erhalten bleibt. Die Verringerung des Abstandes verringert gleichzeitig die Größe des Rochevolumens, der massereichere Stern überfüllt sein Rochevolumen noch mehr, so dass weiteres Material transferiert wird. Dies hat zur Folge, dass der Rote Riese seine gesamte Hülle lawinenartig innerhalb weniger Jahre auf den Begleiter überträgt. Der Begleitstern kann soviel Materie nicht aufnehmen, das Material überfüllt beide Rochevolumina in Form einer zirkumbinären Wolke, die sogenannte Common Envelope Phase bildet sich aus. Auf Grund der starken Reibung beim Umlauf um den gemeinsamen Schwerpunkt innerhalb der gemeinsamen Hülle verringert sich der Abstand der beiden Sterne im Laufe von etwa tausend Jahren von  $\approx 100 R_{\odot}$  auf  $\approx 1 R_{\odot}$ . Das Binärsystem wirkt auf die es umgebende Hülle wie ein Propeller und drückt sie in den interstellaren Raum, es entsteht ein Planetarischer Nebel. Der Primärstern hat sich inzwischen zu einem Weißen Zwerg<sup>8</sup> entwickelt und bildet ge-

---

auch die Leuchtkraft über die Effektivtemperatur aufzutragen. Eine weitere Variante des HRD ist das Farben-Helligkeitsdiagramm, bei dem die Helligkeit in einem Filter über die Differenz der Helligkeiten in zwei verschiedenen Filtern (in der Astrophysik als Farbe bezeichnet) aufgetragen wird.

<sup>5</sup>Die Masse sollte jedoch  $< 8 M_{\odot}$  sein, da er sich sonst anstatt zu einem Weißen Zwerg zu einem Neutronenstern oder Schwarzen Loch entwickelt und anstelle des kataklysmischen Variablen ein Röntgendoppelstern entsteht, siehe Abschnitt 3.3.

<sup>6</sup>Sterne mit weniger als  $0,1 M_{\odot}$  erreichen nicht einmal die für die Wasserstofffusion notwendige Kerntemperatur, sie werden nicht mehr als Sterne betrachtet sondern als Braune Zwerge.

<sup>7</sup>bei Sternmassen  $< 2,5 M_{\odot}$  geschieht dies explosiv als sog. Heliumflash, da der Kern entartet ist.

<sup>8</sup>Weiße Zwerge sind das Endstadium von Sternen mit einer Anfangsmasse von weniger als etwa  $8 M_{\odot}$ . Es handelt sich hierbei um den ausgebrannten Kern des Sterns, im wesentlichen bestehend

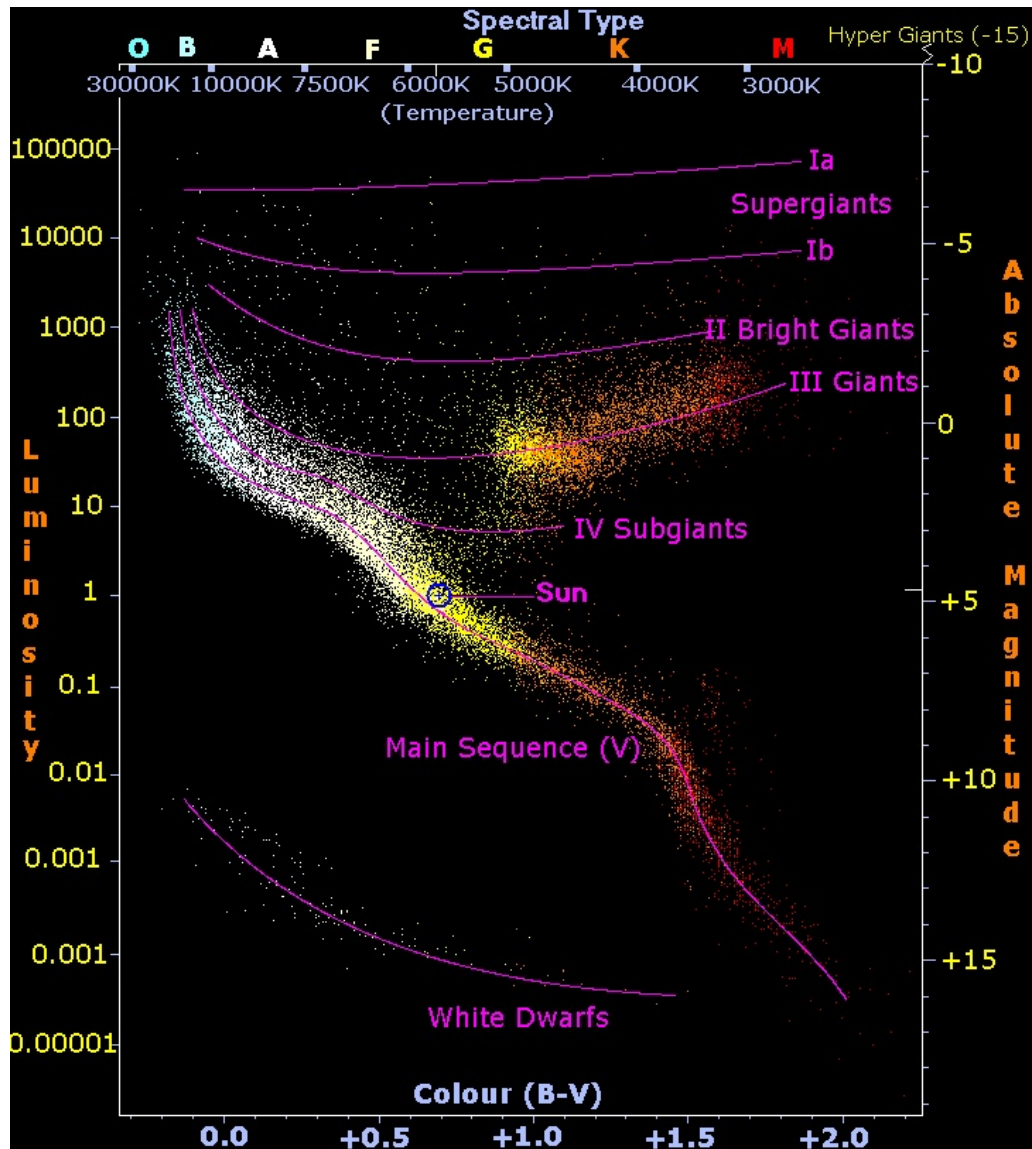


Abbildung 3.2: Hertzsprung-Russell-Diagramm von 22 000 Sternen des Hipparcos-Katalogs sowie 1 000 Sternen des Gliese Catalogue of Nearby Stars. Aufgetragen sind auf der  $x$ -Achse oben der Spektraltyp und die Effektivtemperatur sowie unten die Farbe  $B - V$ , auf der  $y$ -Achse links die Leuchtkraft (in Einheiten der Sonnenleuchtkraft) und rechts die absolute Helligkeit. Eingezeichnet sind die Hauptreihe (Main Sequence) sowie die Gebiete der Roten Riesen (Giants) und Weißen Zwerge (White Dwarfs) sowie die Position unserer Sonne. (Richard Powell, <http://commons.wikimedia.org>)

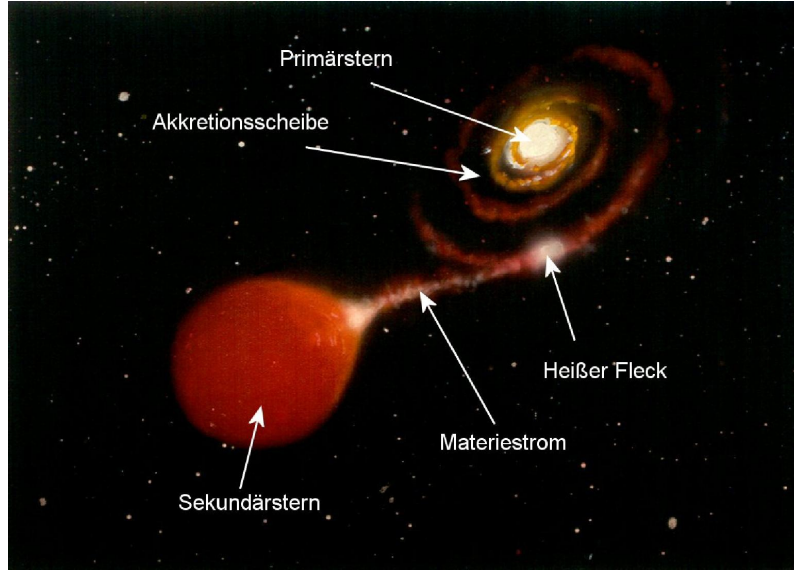


Abbildung 3.3: Künstlerische Darstellung eines kataklysmischen Variablen (http://psi.edu, bearbeitet).

meinsam mit dem noch unentwickelten Sekundärstern ein enges Doppelsternpaar.

Ist der Abstand beider Komponenten gering genug, füllt der Sekundärstern, der inzwischen auf Grund der Schwerkraft des Primärsterns seine sphärische Form verloren hat und einem Ellipsoid ähnelt, sein Rochevolumen aus und transferiert seine äußeren Schichten über  $L_1$  auf den Weißen Zwerg (Roche Lobe Overflow RLO), ein kataklysmischer Variabler ist entstanden (siehe Abb. 3.3). Ein stabiler Massentransfer kann in dieser Situation<sup>9</sup> nur gewährleistet werden, wenn das Gesamtsystem Drehimpuls abgibt. Denn das transferierte Material verliert Drehimpuls und als Reaktion darauf vergrößert sich die Separation, der Sekundärstern füllt sein dadurch größer gewordenes Rochevolumen nicht mehr aus und der Massentransfer kommt zum Erliegen. Gibt das Gesamtsystem jedoch Drehimpuls ab, wirkt dies einer zunehmenden Separation entgegen und ermöglicht einen konstanten Massentransfer<sup>10</sup>. Ein

---

aus Kohlenstoff und Sauerstoff bzw. im Falle massearmer Vorläufersterne aus Helium. Sämtliche Fusionsprozesse sind erloschen, es sind gewissermaßen auskühlende Sternleichen. Ihre Masse liegt in der Größenordnung der Sonnenmasse und kann maximal etwa  $1,44 M_{\odot}$  (Chandrasekhar-Grenzmasse) betragen. Ist die Masse größer, übertrifft die Schwerkraft den Druck des entarteten Elektronengases und das Objekt kollabiert. Da sie nur etwa den Durchmesser der Erde besitzen, sind ihre mittleren Dichten mit  $10^8 - 10^9 \text{ kg/m}^3$  etwa  $10^6$  mal höher als die mittlere Dichte der Sonne.

<sup>9</sup>Die Masse des Primärsterns ist trotz Verlust seiner äußeren Hälften größer als diejenige des Sekundärsterns, die überströmende Materie bewegt sich also zum Massenzentrum hin.

<sup>10</sup>Da ein solcher konstanter Massentransfer nur für  $q < 1$  möglich ist, gleichzeitig der Primärstern die Chandrasekhargrenzmasse nicht überschreiten kann, ergibt sich ein maximaler Orbit, bei dem der Sekundärstern noch sein Rochevolumen ausfüllt, entsprechend einer Orbitalperiode von etwa 12 h. Dies erklärt die starke Abnahme der Anzahl beobachteter CVs mit Perioden größer als 6 h. Die

Mechanismus zur Abgabe von Drehimpuls ist das sog. magnetische Bremsen, verursacht durch die Kombination von Sternwind und Magnetfeld des Sekundärsterns<sup>11</sup>. Eine andere Möglichkeit ist die Abstrahlung von Gravitationswellen (z.B. Misner et al. 1973), dies ist jedoch erst bei geringen Abständen zweier kompakter Objekte effektiv<sup>12</sup>. Meist wird am Beginn der Lebenszeit eines CV der stetige Massentransfer durch magnetisches Bremsen aufrecht erhalten. Im Laufe der Zeit wird dies jedoch immer ineffektiver, vermutlich auf Grund des schwächer werdenden Magnetfeldes des Sekundärsterns, und kommt meist bei Orbitalperioden von etwa 3 h ganz zum Erliegen. Dadurch endet auch der Materietransfer, der kataklysmische Variable ist nicht mehr als solcher beobachtbar. Erst wenn sich die Separation durch Abstrahlung von Gravitationswellen genügend verringert hat, meist bei Orbitalperioden von etwa 2 h, kommt der Sekundärstern wieder in Kontakt mit seinem Rochevolumen und der Materietransfer setzt von Neuem ein. Dies erklärt die Periodenlücke im Bereich von 2-3 h, in der kaum Systeme bekannt sind.<sup>13</sup> Ist nach dem Ende der Common Envelope Phase der Abstand beider Sterne zu groß für ein Einsetzen des Materietransfers, nähern sich beide Sterne durch magnetisches Bremsen solange einander an, bis der Sekundärstern sein Rochevolumen ausfüllt.

Das vom Sekundärstern in einem dünnen Strahl abfließende Material sammelt sich zuerst in einem Akkretionsring um den Primärstern am sog. Zirkularisationsradius  $r_{\text{circ}}$  (Warner 1995):

$$r_{\text{circ}} = a \cdot 0,0859 q^{-0,426} \quad \text{für } 0,05 < q < 1$$

Hier entspricht sein Drehimpuls dem Drehimpuls des Lagrangepunktes  $L_1$ . Viskose Wechselwirkung führt zu einem Zerfließen des Ringes und zur Ausbildung einer Akkretionsscheibe, die bei einem nicht-magnetischen Weißen Zwerg bis an die Oberfläche des Weißen Zwerges heranreichen kann. Da das Material der Akkretionsscheibe bis knapp an die Oberfläche des Weißen Zwerges mit Keplergeschwindigkeit rotiert (3 000 km/s), muss es auf die deutlich langsamere Rotation des Weißen Zwerges (300 km/s) abgebremst werden. Es bildet sich eine Übergangsschicht<sup>14</sup> aus, in der die kinetische Energie des abgebremsten Scheibenmaterials in thermische Energie

---

wenigen Systemen mit Perioden im Bereich einiger dutzend Stunden enthalten einen entwickelten Sekundärstern im Riesenstadium.

<sup>11</sup>Beim *magnetischen Bremsen* werden elektrisch geladene Teilchen des Sternwindes des Sekundärsterns entlang seines Magnetfeldes beschleunigt und ins All geschleudert. Hierbei nehmen sie einen Teil des Drehimpulses des Sekundärsterns mit, dies verlangsamt seine Rotation. Da er auf Grund der starken Gezeitenwechselwirkung mit dem Primärstern gebunden rotiert, geht sein Drehimpulsverlust zu Lasten des Orbits, die Separation verringert sich.

<sup>12</sup>Ein Beispiel des Energieverlustes eines engen Doppelsternsystems durch Gravitationswellenabstrahlung ist das Doppelpulsarsystem PSR 1913+16 (z.B. Weisberg & Taylor 2005). Seine Bahnperiode verkürzt sich um  $\dot{P} = (-2,40 \pm 0,09) \cdot 10^{-12} \text{ ss}^{-1}$  in guter Übereinstimmung mit dem von der allgemeinen Relativitätstheorie vorhergesagten Wert von  $\dot{P}_{\text{ART}} = (-2,403 \pm 0,002) \cdot 10^{-12} \text{ ss}^{-1}$ .

<sup>13</sup>Beobachtete Systeme innerhalb der Periodenlücke sind unter Umständen mit dieser Periode entstanden, d.h. der Sekundärstern kam bei dieser Periode in Kontakt mit seinem Rochevolumen.

<sup>14</sup>Diese *Übergangsschicht* (boundary layer) kann bei einer typischen Effektivtemperatur von  $\approx 200\,000 \text{ K}$  einen erheblichen Teil zur UV-Strahlung des Systems beitragen.

umgewandelt und abgestrahlt wird. Besitzt der Weiße Zwerg ein starkes Magnetfeld ( $> 1 \text{ MG}$ ), bildet sich um den Weißen Zwerg eine magnetisch dominierte Magnetosphäre aus, in der sich die Materie entlang der Magnetfeldlinien bewegt. Die Akkretionsscheibe endet dann am Magnetosphärenradius<sup>15</sup>. Im Falle eines sehr starken Magnetfeldes ( $> 10 \text{ MG}$ ) bildet sich keinerlei Akkretionsscheibe aus, der Materiestrom fließt von  $L_1$  kommend direkt entlang der Magnetfeldlinien auf die Pole des Weißen Zwerges<sup>16</sup>.

Der maximale äußere Rand der Akkretionsscheibe wird durch Gezeitenwechselwirkung mit dem Sekundärstern, wodurch Drehimpuls aus der Scheibe in die Orbitalbewegung transferiert wird, am Gezeitenradius  $r_{\text{tidal}}$  begrenzt (Warner 1995):

$$r_{\text{tidal}} = \frac{a \cdot 0,6}{1 + q} \quad \text{für } 0,03 < q < 1$$

Der vom Sekundärstern kommende Materiestrom trifft auf die voll ausgebildete Akkretionsscheibe, das Kollisionsgebiet heizt sich auf und bildet den sog. „heißen Fleck“. Bis zu etwa einem Drittel des gesamten Lichts eines kataklysmischen Variablen kann aus dieser Region stammen. In der Lichtkurve macht sich der heiße Fleck u. U. als „orbital humps“ bemerkbar, periodisch wiederkehrenden Helligkeitsanstiegen.

Die Akkretionsscheibe kann von Zeit zu Zeit eine thermische Instabilität durchlaufen (Osaki 1974). Dies führt zu sog. Zwergnovaausbrüchen, die sich durch einen schnellen, mehrtägigen Helligkeitsanstieg um bis zu 6 Magnituden, unter Umständen einer anschließenden Plateauphase von einer Woche oder mehr und einem mehrtägigen Helligkeitsabfall bemerkbar machen und sich mehr oder weniger regelmäßig wiederholen, im Falle von SS Cygni z.B. alle 4-10 Wochen für eine Dauer von 1-2 Wochen.

Durch den steten Massentransfer  $\dot{M}_2$  vom Sekundärstern sammelt sich im Laufe der Zeit immer mehr Materie in der Akkretionsscheibe an, die Oberflächenmassendichte  $\Sigma$  steigt, die Temperatur beginnt sich zu erhöhen. In einem Gebiet in der Scheibe<sup>17</sup> erreicht sie einen kritischen Wert  $\Sigma_{\text{max}}$ , bei dem Ionisation des Wasserstoffs einsetzt. In dieser jetzt teilweise ionisierten Region ist die Opazität stark abhängig von der Temperatur, die Materie wird nahezu undurchlässig für Strahlung und heizt sich stark auf. Ausgehend von dieser Region breitet sich eine sog. Heizwelle durch die Scheibe aus, dies ist der Beginn des Zwergnovaausbruchs. Die Heizwelle kann hierbei radial von außen nach innen (outside-in) oder umgekehrt (inside-out) laufen, je nachdem in welcher Region die Instabilität zuerst auftritt.

In der heißen, ionisierten Materie herrscht eine große Viskosität, dies hat einen sehr effektiven Materietransport innerhalb der Akkretionsscheibe in Richtung des Weißen Zwerges zur Folge, die Scheibe entleert sich. In dieser Phase werden typischerweise etwa 10% des Materials der Akkretionsscheibe auf den Weißen Zwerg

<sup>15</sup>Diese Objekte werden als *Intermediate Polars* bezeichnet.

<sup>16</sup>Diese Objekte werden als *Polare* oder *AM Her Sterne* bezeichnet.

<sup>17</sup>Ist die Massentransferrate  $\dot{M}_2$  vom Sekundärstern kleiner als die Akkretionsrate  $\dot{M}$  innerhalb der Scheibe, hat die Materie Zeit zum Innenrand der Scheibe zu fließen und sich dort anzusammeln, im anderen Fall häuft sie sich im Außenbereich an.

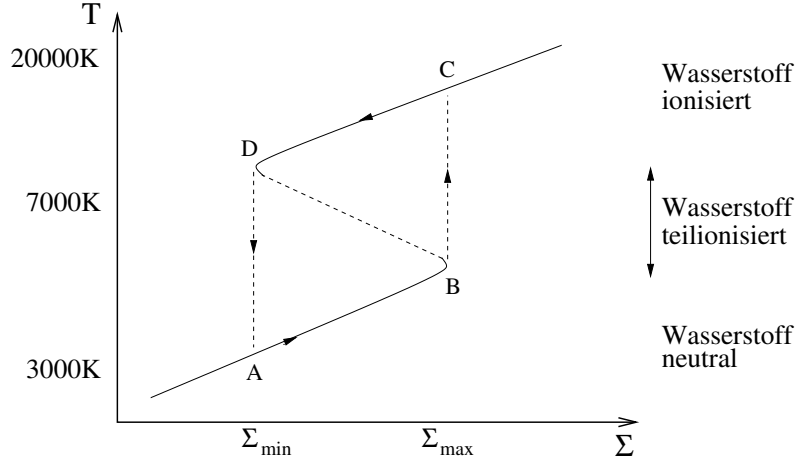


Abbildung 3.4: Darstellung des Verlaufs eines Zergnovaausbruchs (A-B-C-D-A) anhand der S-Kurve.

akkretiert. Mit dem Sinken der Oberflächenmassendichte unter den kritischen Wert  $\Sigma_{\min}$  fällt die Temperatur, eine Kühlwelle durchläuft die Scheibe von außen radial nach innen. Der Wasserstoff rekombiniert, der viskose Materietransport wird ineffektiv und die Akkretionscheibe befindet sich wieder in ihrer Ruhephase. Dieser zyklische Verlauf kann anhand der S-Kurve in Abb. 3.4 gut nachvollzogen werden.

In der auf Grund der wiederkehrenden Akkretionsphasen stetig anwachsenden Wasserstoffhülle des Weißen Zwergs kann nach einiger Zeit<sup>18</sup>, wenn Druck und Temperatur entsprechende Werte angenommen haben, Wasserstofffusion explosionsartig einsetzen. Dies führt zum Absprengen der akkretierten Schicht, die Helligkeit des Systems nimmt um bis zu 10 Magnituden zu, man spricht von einem Nova-Ausbruch<sup>19</sup>. Überschreitet der Weiße Zwerge aufgrund der fortdauernden Akkretion die Chandrasekhar-Grenzmasse, kommt es durch das explosive Zünden des Kohlenstoffkerns zu einer Supernova Typ Ia, die den Weißen Zwerge und damit den katakllysmischen Variablen zerstört (z.B. Langer et al. 2000). Dieses dramatische Ende stellt jedoch die Ausnahme dar.

Gegen Ende des Lebens der meisten katakllysmischen Variablen wird die Masse des Sekundärsterns so klein, dass er bei  $M_2 \approx 0.06 M_\odot$  entartet. Ein weiterer Massenverlust führt deshalb zu einer Zunahme seines Durchmessers. Die durch den Materietransfer eigentlich hervorgerufene Expansion des Systems muss nun nicht mehr durch Drehimpulsverlust des Binärsystems kompensiert werden, der Sekundärstern

<sup>18</sup> Abhängig von Primärsternmasse und Akkretionsrate wiederholen sich Novae im Abstand von einigen tausend bis Millionen Jahren.

<sup>19</sup> Die *rekurrierenden Novae* stellen hierbei eine Besonderheit dar. Sie besitzen Primärsterne nahe der Chandrasekhar-Grenzmasse von  $1,44 M_\odot$  und große Akkretionsraten von mehr als  $10^{-8} M_\odot/\text{a}$ . Novae treten in diesen Systemen in Abständen von weniger als 100 Jahren auf, ein bekannter Vertreter dieser Klasse ist T Pyxidis mit fünf Ausbrüchen seit 1890. Allerdings enthalten sie oft Sekundärsterne im Riesenstadium, sie sind also keine typischen Vertreter der katakllysmischen Variablen.

kann auf Grund seiner eigenen Expansion ständig Kontakt zu seinem Rochevolumen halten, der kataklysmische Variable entwickelt sich hin zu längeren Orbitalperioden bei gleichzeitig sinkenden Massentransferraten und stark abnehmender Helligkeit. Dieser Effekt tritt bei Orbitalperioden von  $\approx 78$  Minuten ein und erklärt das beobachtete Periodenminimum der kataklysmischen Variablen. Letztendlich verwandelt sich der kataklysmische Variable in einen Weißen Zwerg mit einem jupiterähnlichen Objekt im Orbit.

Am Beispiel von SS Cygni haben wir die zeitliche spektrale Entwicklung eines Zwergnovaausbruches untersucht (Kromer et al. 2007, Anhang A). Wir haben unter anderem gezeigt, dass sich ein Outside-In-Ausbruch anhand zeitaufgelöster Spektren von einem Inside-Out-Ausbruch unterscheiden lässt. Hierzu haben wir die einzelnen Ringe sowohl für die Ausbruchsphase als auch die Ruhephase berechnet und in unterschiedlichen Kombinationen, entsprechend verschiedenen Zeitschritten eines Zwergnovaausbruches, jeweils zu einem Gesamtspektrum der Akkretionsscheibe auf-integriert. Auf diese Weise kann der spektrale Verlauf beliebiger Ausbruchsszenarien (Outside-In, Inside-Out oder partiell) simuliert werden. Ein Vergleich unserer Modellspektren mit beobachteten Spektren, die einen Zwergnovaausbruch bzw. die Rückkehr in die Ruhephase teilweise abdecken (Hessman et al. 1984), favorisiert thermische Instabilitäten in der Akkretionsscheibe als Ursache eines Zwergnovaausbruches gegenüber dem alternativen Erklärungsmodell eines instabilen Massentransfers vom Sekundärstern<sup>20</sup>.

Ebenfalls am Beispiel der Zwergnova SS Cygni untersuchen wir zur Zeit, in wie weit die Berücksichtigung der Rotationsverbreiterung bereits während der Berechnung des Strahlungstransports das Linienprofil beeinflusst im Vergleich zur Anwendung der Rotationsverbreiterung auf das fertig berechnete Spektrum (Korčáková et al. 2009). Erste Ergebnisse zeigen, dass ein erkennbarer Unterschied in den Linienprofilen nur auftritt, wenn die gesamte Akkretionsscheibe optisch extrem dünn ist.

Verwandt mit den Kataklysmischen Variablen sind die Symbiotischen Sterne. Der Weiße Zwerg wird in diesen Systemen von einem Roten Riesen begleitet, die Orbitalperioden bewegen sich im Bereich von Tagen bis Jahren (z.B. Belczyński et al. 2000). Der Massentransfer auf den Weißen Zwerg geschieht im Gegensatz zu klassischen kataklysmischen Variablen nicht via RLO, vielmehr akkretiert der Weiße Zwerg Material aus dem starken Sternwind des Roten Riesen, die Akkretionsrate liegt bei  $10^{-7} - 10^{-8} M_{\odot}/a$ . Ob sich hierbei immer eine Akkretionsscheibe ausbildet ist unklar. Für Parameter, die typisch für einen Symbiotischen Stern sind, habe ich an einem exemplarischen Beispiel gezeigt, dass die Akkretionsscheibe den optischen Spektralbereich dominiert. Der beobachtete, hohe UV Fluss wird durch den inneren Bereich der Akkretionsscheibe verursacht, während der Fluss des Weißen Zwerges nur im EUV-Bereich den der Akkretionsscheibe übertrifft (Nagel et al. 2003).

---

<sup>20</sup>In diesem Szenario führt eine Instabilität im Sekundärstern zu einem erhöhtem Massentransfer. Das überströmende Material sammelt sich am Außenrand der Akkretionscheibe an, so dass die Helligkeitsausbrüche von Außen nach Innen verlaufen (Bath 1975).

## 3.2 AM CVn Sterne

AM CVn Sterne bilden eine Unterklasse der kataklysmischen Variablen mit zur Zeit 26 bekannten Mitgliedern (Nelemans et al. 2010). Ihre Orbitalperioden liegen zwischen 5 und 65 Minuten, sie sind damit allesamt kurzperiodischer als die klassischen kataklysmischen Variablen. Ihre Spektren sind dominiert von Linien des Heliums, Anzeichen für ein Vorhandensein von Wasserstoff gibt es dagegen keine. Der Primärstern in AM CVn Systemen ist wie bei einem klassischen CV ein Weißer Zwerg. Die kurze Orbitalperiode und damit die Kompaktheit des Gesamtsystems erfordert auch für die ihr Roche-Volumen ausfüllende Sekundärkomponente ein kompaktes Objekt. Die genaue Natur des Sekundärsterns und damit die Entstehung der AM CVn Sterne ist noch nicht endgültig geklärt, drei mögliche Szenarien werden derzeit diskutiert (z.B. Nelemans et al. 2010):

1. Es handelt sich um ein *Weisse Zwerge Binärsystem*, das einen massearmen und einen massereichen Weißen Zwerg beinhaltet. Die masserärmere Komponente füllt dabei ihr Rochevolumen aus und transferiert Materie auf den massereicheren.
2. Der Sekundärstern ist ein *Heliumstern*, der sein Rochevolumen ausfüllt.
3. Es war ursprünglich ein *klassischer CV*, bei dem ein Hauptreihenstern Masse auf einen Weißen Zwerg transferiert. Wenn der Massentransfer hierbei hinreichend spät auf der Hauptreihe einsetzt, kann der wasserstoffarme Kern des Sekundärsterns während des Massentransfers freigelegt werden.

Die Spektralanalyse der Akkretionsscheibe erlaubt die Bestimmung der chemischen Zusammensetzung der Hülle des Donorsterns und ist dadurch ein ideales Mittel, die Entstehungsgeschichte der AM CVn Sterne auffinden zu helfen.

AM CVn Sterne tragen unter Umständen erheblich zur Produktionsrate von Typ Ia Supernovae bei (Nelemans et al. 2001; Solheim & Yungelson 2005). Außerdem sind sie Quellen niederfrequenter Gravitationswellenstrahlung, wie sie von der geplanten Laser Interferometer Space Antenna LISA entdeckt werden kann (z.B. Hils & Bender 2000). Anhand ihrer photometrischen und spektralen Eigenschaften lassen sich AM CVn Sterne in mehrere Untergruppen einteilen:

- Systeme mit sehr kurzen Orbitalperioden zwischen 5 und 10 Minuten und Akkretionsraten in der Größenordnung von  $> 10^{-8} M_{\odot}/a$ . Ihre Zugehörigkeit zur Gruppe der AM CVn Sterne ist noch nicht geklärt (z.B. Nelemans 2005).
- Systeme mit kurzen Orbitalperioden zwischen 10 und 20 Minuten, sogenannte high-state-Systeme mit Akkretionsraten in der Größenordnung von  $10^{-8} M_{\odot}/a$ , zeigen Absorptionslinienspektren.
- Systeme mit mittleren Orbitalperioden zwischen 20 und 40 Minuten, sogenannte outbursting-Systeme mit Akkretionsraten in der Größenordnung von

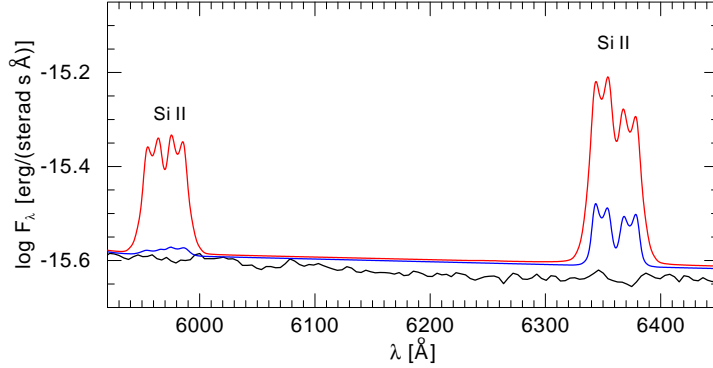


Abbildung 3.5: Vergleich eines beobachteten Spektrums von CE 315 (schwarz) und zweier Modellspektren mit solarer (rot) und 0,001 fach solarer (blau) Siliziumhäufigkeit.

$10^{-9} M_{\odot}/a - 10^{-10} M_{\odot}/a$ , zeigen einen Wechsel zwischen Absorptions- und Emissionslinienspektren. Die Ursache hierfür sind Zwergnovaausbrüche analog zu klassischen CV, hier jedoch durch einen Wechsel der Heliumionisation ausgelöst (z.B. Patterson et al. 2000).

- Systeme mit langen Orbitalperioden zwischen 40 und 70 Minuten, sogenannte low-state-Systeme mit Akkretionsraten in der Größenordnung von  $10^{-11} M_{\odot}/a$ , zeigen Emissionslinienspektren.

In meiner Forschungsarbeit habe ich u.a. das bisher umfangreichste Modellgitter für AM CVn Systeme erarbeitet. Durch die Variation von Primärsternmasse und Akkretionsrate erstrecken sich die Modelle über den gesamten Parameterbereich der bekannten AM CVn Systeme<sup>21</sup>. Die chemische Zusammensetzung besteht aus Wasserstoff, Helium, Kohlenstoff, Stickstoff, Sauerstoff und Silizium, wobei die Häufigkeiten variiert wurden. Ich konnte unter anderem belegen, dass eine große Akkretionsrate zu einem Absorptionslinienspektrum, eine kleine Akkretionsrate dagegen zu einem Emissionslinienspektrum führt. Des Weiteren habe ich obere Nachweisgrenzen für die Wasserstoffhäufigkeiten bei verschiedenen Akkretionsraten bestimmt. Im Falle von CE 315, dem AM CVn System mit der größten Orbitalperiode von 65,1 min, habe ich mittels Analyse eines beobachteten Spektrums (Ruiz et al. 2001) eine starke Silizium-Unterhäufigkeit<sup>22</sup> (siehe Abb. 3.5) und damit die Zugehörigkeit zur Sternpopulation II<sup>23</sup> bestätigt (Nagel et al. 2009, siehe Anhang B). Auch für SDSS J0926+3624

<sup>21</sup>Die Primärsternmasse wurde zwischen  $0,6 M_{\odot}$  und  $1,4 M_{\odot}$  variiert, die Akkretionsrate für jede Masse zwischen  $10^{-8} M_{\odot}/a$  und  $10^{-11} M_{\odot}/a$ .

<sup>22</sup>kleiner als  $10^{-3}$  in Massenbruchteilen im Vergleich zu solaren Werten

<sup>23</sup>Sterne der *Population II* sind ältere, metallarme Sterne, die man in unserer Galaxis vorwiegend im Halo und in Kugelsternhaufen findet. Sie sind metallärmer als die Sterne der *Population I*, der jungen Sterne in den Spiralarmen angehören. Die allerersten und damit ältesten Sterne werden der *Population III* zugerechnet.

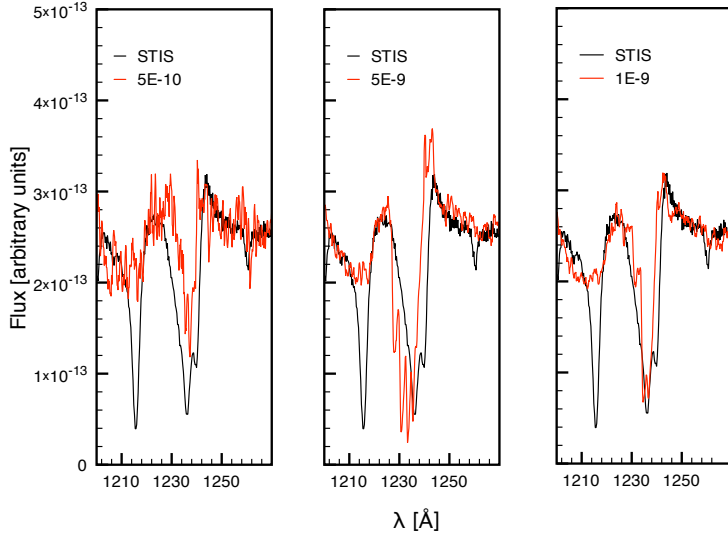


Abbildung 3.6: Vergleich eines mit STIS (HST) beobachteten Spektrums (schwarz) von AM CVn und eines Modellspektrums (rot) mit drei verschiedenen Massenverlustraten ( $5 \cdot 10^{-10}$ ,  $5 \cdot 10^{-9}$  und  $1 \cdot 10^{-9} M_{\odot}/a$ ) anhand der N V 1240 Å Resonanzlinie (Kusterer 2008). Die Inklination beträgt  $i=39^\circ$ ,  $M_1=0,6 M_{\odot}$ . Die Ly $\alpha$  Linie des Wasserstoffs bei 1216 Å ist interstellaren Ursprungs.

und SDSS J1411+4812 fanden wir Hinweise auf eine starke Siliziumunterhäufigkeit (Nagel et al. 2008).

Das Spektrum von AM CVn zeigt im ultravioletten Spektralbereich sog. P Cygni Linienprofile. Dies ist ein typisches Merkmal für einen starken Massenverlust in Form eines von der Akkretionsscheibe abströmenden Windes, wie man ihn auch in den Ausbruchphasen der klassischen, wasserstoffdominierten CV findet. Wir haben ein auf Monte-Carlo-Methoden basierendes Programm entwickelt, um die Windgeometrie und Beschleunigungsmechanismen zu untersuchen sowie die Massenverlustrate zu bestimmen, erste Ergebnisse sind bereits sehr vielversprechend (Kusterer 2008).

Die neuesten Modellrechnungen beinhalten neben weiteren leichten Metallen wie Neon und Magnesium auch Eisen. Ziel ist hierbei eine weitergehende Analyse von CE 315 und insbesondere V803 Cen, ein AM CVn Stern, der Zergnovaausbrüche und damit einen Wechsel von einem Emissionslinienspektrum in ein Absorptionslinienspektrum zeigt. Basierend auf Arbeiten von Nelemans et al. (2010), die die chemische Zusammensetzung der Sekundärsterne in AM CVn Systemen berechnet haben, erarbeitete ich Modellspektren von Akkretionsscheiben, wie sie sich in den einzelnen Entstehungsszenarien bilden können, um herauszufinden ob und anhand welcher spektralen Eigenschaften der Akkretionsscheibe sich die einzelnen Szenarien unterscheiden lassen und in welchen Wellenlängenbereichen die hierzu notwendigen Beobachtungen durchgeführt werden müssen.

### 3.3 Ultrakompakte Röntgendoppelsterne

Im Unterschied zu kataklysmischen Variablen besitzen Röntgendoppelsterne als Primärstern keinen Weißen Zwerg, sondern einen Neutronenstern oder ein schwarzes Loch. Diese deutlich kompakteren Objekte haben sich aus einem Vorläuferstern mit mehr als acht Sonnenmassen gebildet (z.B. Woosley et al. 2002). Bei einem derart massereichen Stern endet die Energiegewinnung im Kern nicht mit der Heliumfusion, vielmehr schließen sich weitere Fusionsprozesse an, bis sich ein Kern aus Eisen und Nickel gebildet hat<sup>24</sup>. Auf Grund der nun erreichten maximalen Bindungsenergie pro Nukleon sind keine weiteren Fusionsprozesse hin zu schwereren Elementen unter Energiegewinnung mehr möglich, der Kern beginnt unter seiner eigenen Schwerkraft zu kontrahieren, wobei die Dichte ein mehrfaches der Atomkerndichte erreicht. Die Eisenkerne werden durch Photodesintegration letztendlich in Protonen und Neutronen zerlegt. Bei einer Masse des ehemaligen Eisenkerns von nicht mehr als etwa  $2 M_{\odot}$  kommt die Kontraktion mit der Bildung eines sog. Neutronensterns zum Stillstand, Protonen und Elektronen haben sich im inversen  $\beta$ -Zerfall unter Aussendung von Neutrinos zu Neutronen vereinigt. Dem Gravitationsdruck wird nun durch den Fermidruck des Neutronengases die Waage gehalten. Übertrifft die Masse des Kerns, z.B. durch das Einfallen weiterer Materieschichten, jedoch die Oppenheimer-Volkoff-Grenzmasse von  $\approx 2 M_{\odot}$ , kollabiert er weiter bis zur Ausbildung einer Singularität, ein Schwarzes Loch ist entstanden.

Beide Endstadien gehen einher mit einer Supernova<sup>25</sup>, dem plötzlichen extrem hellen Aufleuchten des Sterns. Sobald der Kollaps des inneren Kerns ruckartig zum Stillstand kommt, läuft eine Stoßwelle dem weiterhin eingefallenen äußeren Kern und den darüber liegenden Schichten des Sterns entgegen, die äußeren Schichten werden auf bis zu 500 000 K aufgeheizt und auf Geschwindigkeiten  $\gg 10000 \text{ km/s}$  beschleunigt, der Stern sprengt somit seine gesamte Hülle in das ihn umgebende interstellare Medium ab.<sup>26</sup>

Die Masse der Sekundärkomponente ist ausschlaggebend für die Einteilung als massearmer ( $M_2 < 1 M_{\odot}$ ) oder massereicher ( $M_2 \gg 1 M_{\odot}$ ) Röntgendoppelstern. Bei

<sup>24</sup>Die einzelnen Fusionphasen laufen dabei immer schneller ab. Ein schwerer Stern kann einige Millionen Jahre aus Wasserstofffusion Energie gewinnen, während die Fusion von Silizium als letzte Fusionsstufe nur noch Stunden bis Tage anhält.

<sup>25</sup>Hierbei handelt es sich um die *Kernkollaps-Supernovae* vom Typ Ib, Ic und Typ II, im Gegensatz zu den in Binärsystemen auftretenden *thermonuklearen Supernova* Typ Ia. Typ Ib Supernovae zeigen keine Spektrallinien des Wasserstoffs jedoch des Siliziums, Typ Ic kaum Heliumlinien, kein Wasserstoff und kein Silizium in ihren Spektren. Ihre Vorläufersterne sind vermutlich Wolf-Rayet Sterne, extrem massereiche, entwickelte Sterne, die auf Grund ihres starken Sternwindes eine hohe Massenverlustrate von bis zu  $10^{-4} M_{\odot}/\text{a}$  besitzen und dadurch ihre wasserstoff- und heliumreichen äußeren Schichten abstoßen. Supernovae vom Typ II zeigen dagegen Wasserstofflinien in ihren Spektren.

<sup>26</sup>Viele Details dieser Prozesse sind noch nicht endgültig geklärt, die Grenzmasse zur Ausbildung eines Schwarzen Loches hängt auch von der noch unbekannten Zustandsgleichung der Neutronensterne ab. Der größte Teil der bei einer Supernova freiwerdenden Energie wird in Form von Neutrinos abgegeben.

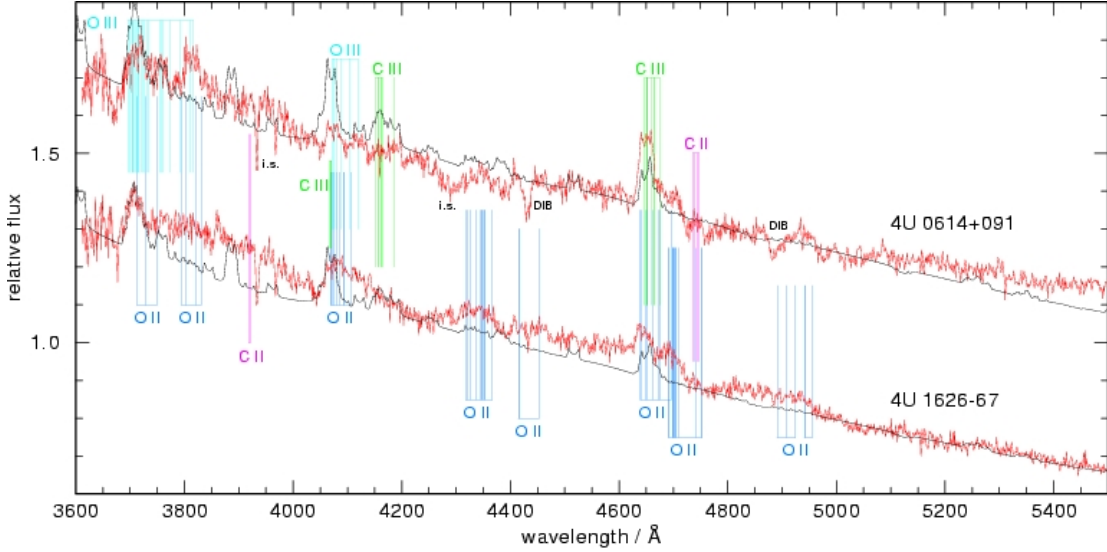


Abbildung 3.7: Beobachtete Spektren (rot) der beiden UCXB 4U 0614+091 und 4U 1626-67. Eingezeichnet sind Emissionslinienpositionen von Sauerstoff und Kohlenstoff sowie jeweils ein Modellspektrum (schwarz) (Werner et al. 2006).

ersteren erfolgt die Akkretion auf den Primärstern via Roche Lobe Overflow analog zu kataklysmischen Variablen, während in den massereichen Systemen der Primärstern Materie aus dem starken Sternwind des Sekundärsterns akkretiert.

Die ultrakompakten, massearmen Röntgendifoppelsterne (UCXB) nehmen mit Orbitalperioden  $< 80$  min eine Sonderrolle ein, ähnlich den AM CVn Sternen bei den kataklysmischen Variablen. In den UCXB<sup>27</sup> muss auf Grund der Kompaktheit der Systeme<sup>28</sup> der Sekundärstern ein nicht-entarteter wasserstoffreicher Stern oder Weißer Zwerg sein (Verbunt & van den Heuvel 1995). Es deutet sich hierbei an, dass es sowohl UCXB gibt mit einem Helium-Weißen-Zwerg als Sekundärstern<sup>29</sup> als auch solche mit einem Kohlenstoff-Sauerstoff-Weißen-Zwerg, wie im Falle der von mir untersuchten UCXB 4U 0614+091 und 4U 1626-67. Die Spektren dieser beiden Objekte werden im optischen und ultravioletten Spektralbereich dominiert von Emissionslinien des Kohlenstoffs und Sauerstoffs, die auf Grund ihres Linienprofils einer Akkretionsscheibe zugeordnet werden können (Siehe Abb. 3.7). Wie im Falle der AM CVn Sterne ist auch die Entstehung der UCXB nicht geklärt, es werden aber dieselben Szenarien diskutiert, eine ausführliche Betrachtung findet sich in Nelemans et al. (2010).

Der Sekundärstern in den von mir analysierten Objekten ist der seiner äußeren Hälften beraubte, massearme Kohlenstoff-Sauerstoff-Kern eines Weißen Zwerges

<sup>27</sup>Zur Zeit sind 27 derartige Objekte bekannt, einschließlich einiger Kandidaten, deren Zugehörigkeit zu den UCXB noch nicht gesichert ist (Nelemans et al. 2010).

<sup>28</sup>Die Separation beider Komponenten entspricht etwa der Distanz Erde-Mond.

<sup>29</sup>Ein Helium-Weißen-Zwerg würde im Falle von 4U 1820-30 erklären, wieso er neben normalen Röntgenbursts auch Superbursts zeigt (Brown & Bildsten 1998; Strohmayer & Brown 2002).

( $M_2 \ll 0.1 M_\odot$ ). Dies bietet die einzigartige Möglichkeit, das Innere eines Weißen Zwerges spektroskopisch zu untersuchen, da sich dieses Material via Roche Lobe Overflow in einer Akkretionsscheibe um das kompakte Objekt sammelt. Ich konnte das Fehlen von Wasserstoff und Helium in der Akkretionsscheibe bestätigen und obere Grenzen für die entsprechenden Häufigkeiten bestimmen (Werner et al. 2006, siehe Anhang C). Es deutet sich außerdem an, dass das O/C-Verhältnis in 4U 0614+091 größer ist als in 4U 1626-67. Dies kann dahingehend interpretiert werden, dass der Massentransfer in 4U 0614+091 schon weiter fortgeschritten ist und tieferliegende Schichten des Weißen Zwerges transferiert werden.

Meine Modelle zeigen keine Anzeichen für eine deutliche Überhäufigkeit von Neon (Werner et al. 2006), wie von Juett & Chakrabarty (2003) aus Röntgenbeobachtungen abgeleitet wurde, und bestätigen damit die Schlussfolgerungen von Juett & Chakrabarty (2005), dass die vormals abgeleiteten ISM Häufigkeiten von Neon durch Ionisationseffekte beeinflusst werden und nicht den in den Sekundärsternen vorliegenden Häufigkeiten entsprechen. Die aus meinen Modellen abgeleitete Obergrenze der Neonhäufigkeit von etwa 10% führt zu zwei möglichen Schlussfolgerungen: Ist der Kern des Weißen Zwerges auskristallisiert und fraktioniert, resultiert der Kristallisationsprozess offenbar nur in einer geringen Neon-Anreicherung. Sollte Kristallisation jedoch zu einer großen Neonhäufigkeit führen (Yungelson et al. 2002), dann hatte der Weiße Zwerg noch keine Zeit zu kristallisieren.



# Kapitel 4

## Akkretionsscheiben um Einzelsterne

### 4.1 Supernova-Fallback-Scheiben

Die Existenz von Akkretionsscheiben um die stellaren Überreste von Supernovae wird seit vielen Jahren kontrovers diskutiert. Es wird allgemein angenommen, dass es sich bei den anomalen Röntgenpulsaren (AXPs), jungen, langsam rotierenden<sup>1</sup> isolierten Neutronensternen, um sogenannte Magnetare handelt und sie die Energie für ihre Röntgenleuchtkraft aus ihrem extrem starken Magnetfeld von bis zu  $10^{14}$  G und mehr schöpfen (Woods & Thompson 2006). Es ist jedoch auch vorstellbar, dass die Röntgenemission aus einer Akkretionsscheibe stammt, die aus dem bei der Supernovaexplosion ausgeworfenen Material hervorgegangen ist (van Paradijs et al. 1995; Chatterjee et al. 2000; Alpar 2001). Der geringe im optischen und infraroten Spektralbereich beobachtete Fluss legt jedoch nahe, dass derartige Fallbackscheiben sehr kompakt sein müssen (Perna et al. 2000; Israel et al. 2004). Kürzlich entdeckte Infrarotemission des AXP 4U 0142+61 wird einer Staub- (Wang et al. 2006) oder Gasscheibe (Ertan et al. 2007) zugeschrieben. Die Modellierung und Analyse derartiger Akkretionsscheiben erlaubt unter anderem die Ableitung der Magnetfeldstärke des Neutronensterns durch die Bestimmung des Innenradius der Scheibe, da der Innenrand der Scheibe dem Magnetosphärenradius des Magnetars entspricht.

Ein weiterer Hinweis auf die Existenz von Fallback-Scheiben sind Jets von Pulsaren wie dem Crab- oder Vela-Pulsar. Diese Jets könnten durch einen von der Akkretionsscheibe abströmenden Wind entstehen, der mit dem Pulsarwind interagiert und ihn bündelt (Blackman & Perna 2004). Auch die erhöhte Röntgenleuchtkraft, die nach einem gewaltigen Flareausbruch der Quelle SGR 1900+14 beobachtet wurde, könnte mit einer Fallback-Scheibe erklärt werden (Ertan & Alpar 2003).

Im Falle des stellaren Überrestes der Supernova SN 1987A<sup>2</sup> wird eine Fallback-

<sup>1</sup>Sie besitzen ein Alter von weniger als 100 000 Jahren, ihre Rotationsperioden liegen im Bereich von etwa 5-12 s.

<sup>2</sup>Die Kernkollaps-Supernova SN 1987A war seit Keplers Supernova 1604 die erste in unserer unmittelbaren Umgebung. Sie wurde am 24. Februar 1987 im etwa 170 000 Lichtjahre entfernten

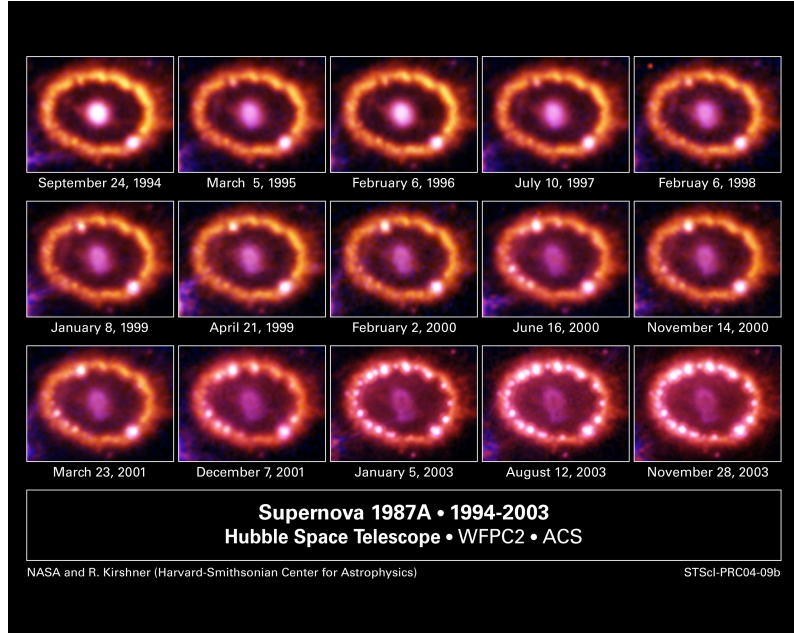


Abbildung 4.1: Zeitliche Entwicklung des zentralen Gebiets in der Supernova SN 1987A.

Scheibe diskutiert, die den von aus theoretischen Modellen für radioaktiven Zerfall von  $^{56}\text{Co}$ ,  $^{57}\text{Co}$  und  $^{44}\text{Ti}$  erwarteten abweichenden Verlauf der beobachteten Lichtkurve erklären könnte (Meyer-Hofmeister 1992). Die Tatsache, dass bisher weder im optischen noch im UV eine Punktquelle gefunden wurde, die dem stellaren Supernovaüberrest zugeordnet werden kann, setzt der radialen Ausdehnung einer möglicherweise vorhandenen Scheibe enge Grenzen (Graves et al. 2005). In meiner Forschungsarbeit zur Supernova SN 1987A habe ich gezeigt, dass die Annahme eines simplen Schwarzkörperspektrums den Fluss, abhängig vom Inklinationswinkel, im Vergleich zu den von mir berechneten realistischeren NLTE Modellen<sup>3</sup> um bis zu einem Faktor zwei unter- bzw. überschätzt (Abb. 4.2). Dies hat zur Folge, dass die Ausdehnung einer hypothetischen Scheibe um SN 1987A, die aus dem Vergleich von Schwarzkörperspektren mit Beobachtungen des Hubble Weltraumteleskops HST im blauen Spektralbereich (Filter F330W) gewonnen wurde, um etwa 30 % auf etwa 70 000 km reduziert werden muss<sup>4</sup> (Werner et al. 2007, siehe Anhang D). Die genaue chemische Zusammensetzung einer Supernova-Fallback-Scheibe ist nicht bekannt,

Tarantelnebel in der Großen Magellanschen Wolke, einer kleinen Begleitgalaxie unserer Milchstrasse, entdeckt. Ihr Vorläuferstern war ein blauer Überriese namens Sanduleak -69° 202 (Gilmozzi et al. 1987).

<sup>3</sup>Hierbei wurden für die Akkretionsrate  $3 \cdot 10^{-9} M_{\odot}/\text{a}$ , entsprechend 30 % der Eddingtonleuchtkraft, und für die Masse des Neutronensterns  $1,4 M_{\odot}$  angenommen. Innerer und äußerer Rand der Akkretionsscheibe betrugen 2 000 km bzw. 200 000 km.

<sup>4</sup>Hierbei wird angenommen, dass die Inklination der Scheibe  $43^{\circ}$  beträgt, abgeleitet aus dem beobachteten inneren äquatorialen Ring.

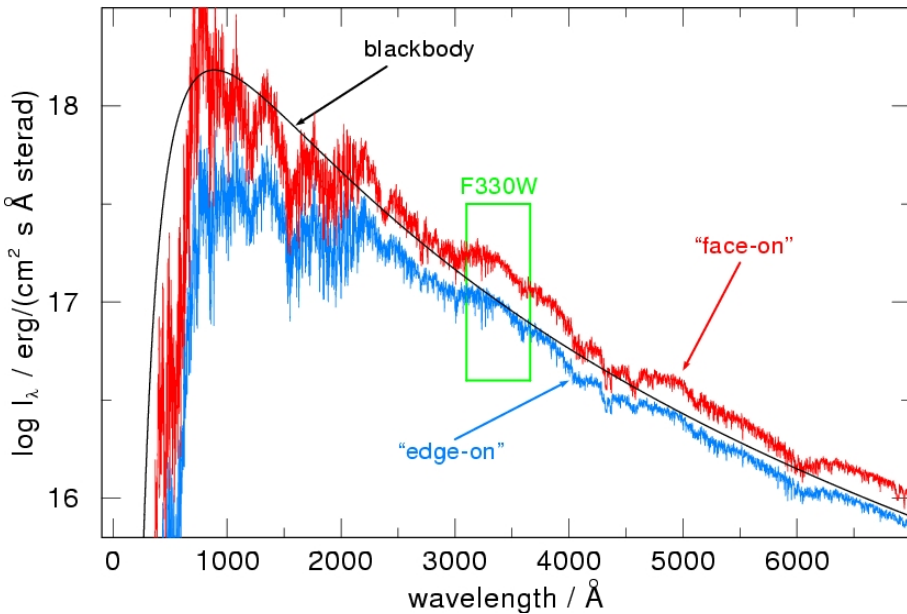


Abbildung 4.2: Vergleich zweier Modellspektren eines Scheibenringes für  $18^\circ$  (rot) und  $87^\circ$  (blau) Inklination mit einem Schwarzkörperspektrum (schwarz) mit  $T_{\text{eff}}=33\,000\,\text{K}$ . In grün eingezeichnet der Bereich des HST/ACS Filters F330W. Das Schwarzkörperspektrum unterschätzt den Fluss für nahezu alle Inklinationswinkel der Akkretionsscheibe (Werner et al. 2007, siehe Anhang D).

ich habe deshalb sowohl Modelle für eine nur aus Eisen bestehende Scheibe als auch mit einer chemischen Zusammensetzung, die der Siliziumbrennasche<sup>5</sup> entspricht, berechnet. Das Eisenmodellatom umfasst hierbei die ersten 11 Ionisationsstufen und mehr als 3 Millionen Spektrallinien<sup>6</sup>. Ich habe gezeigt, dass die chemische Zusammensetzung der Akkretionsscheibe spektroskopisch im Detail nicht bestimmbar ist, solange Eisen der dominierende Bestandteil ist (Werner et al. 2007, siehe Anhang D).

## 4.2 Debris-Scheiben um Weiße Zwerge

Ende der 1980er wurde um den DAZ<sup>7</sup> Weißen Zwerg G29-38 ein Infrarotexzess entdeckt (Zuckerman & Becklin 1987), der in der Folgezeit als äquatorialer Staubgürtel (Graham et al. 1990) interpretiert und vor kurzem vom Spitzer-Weltraumteleskop bestätigt wurde (Reach et al. 2005). Spektralanalysen des Weißen Zwerges zeigen

<sup>5</sup> Siliziumbrennasche bezeichnet eine chemische Zusammensetzung aus 80% Eisen und je 10% Silizium und Schwefel, wie sie typischerweise nach der Siliziumfusion im Kern vorliegt.

<sup>6</sup> Die Atomdaten stammen aus Kurucz (1991), Opacity Project und Iron Project (TIPTOPbase, <http://cdsweb.u-strasbg.fr/topbase/home.html>).

<sup>7</sup> Weiße Zwerge, deren Spektren Linien von Wasserstoff und Metallen, jedoch nicht von Helium enthalten, werden als *DAZ Weiße Zwerge* bezeichnet.

eine Anreicherung mit Metallen. Da die Zeitskalen für gravitatives Absinken der Metalle in der Photosphäre kurz sind, muss eine fortwährende Akkretion von Materie auf den Weißen Zwerge stattfinden (Koester et al. 1997). Das Fehlen eines Begleitsternes um G29-38 unterstützt den Schluss eines zirkumstellaren Materieringes bzw. einer Materiewolke. Im Rahmen einer Beobachtungskampagne des WET, an der ich teilgenommen habe, wurde die Verteilung von Kalzium auf der Oberfläche von G29-38 untersucht und gezeigt, dass die Akkretion des Kalziums über die Pole erfolgt (Thompson et al. 2010). Inzwischen wurden weitere von einer Staubscheibe umgebene Weiße Zwerge entdeckt (Becklin et al. 2005; Kilic et al. 2005, 2006; Farihi et al. 2007, 2009).

Vor kurzem wurden auch Gasscheiben um DAZ und DBZ<sup>8</sup> Weiße Zwerge nachgewiesen (Gänsicke et al. 2006, 2008), deren Spektren meist ausgeprägte Emissionslinien von Kalzium ( $\lambda\lambda$  8498, 8542, 8662 Å), jedoch keinerlei Anzeichen von Wasserstoff und Helium zeigen. Im Falle von SDSS J1228+1040 wurden sogar sowohl eine Staub- als auch eine Gaskomponente nachgewiesen (Brinkworth et al. 2009).

Die Ausdehnung der Gas- und Staubscheiben beträgt etwa  $1,5 R_{\odot}$ , damit liegen sie innerhalb des Gezeitenradius eines typischen Weißen Zwerges (Jura 2003). Als Entstehungsszenario ist die Zerstörung von Kometen (Debes & Sigurdsson 2002) oder Asteroiden (Jura 2003) durch Gezeitenkräfte des Weißen Zwerges denkbar, insbesondere letzteres wird durch das Nichtvorhandensein von Wasserstoff und Helium gestützt. Allerdings müssen sich diese Objekte auf Grund der Roten-Riesen-Phase des Vorläufersterns ursprünglich in einigen  $100 R_{\odot}$  Entfernung befunden haben (Gänsicke et al. 2006). Planeten, die die Rote-Riesen-Phase des Vorläufersterns überlebt haben, stören die Bahn eines solchen Asteroiden und er gelangt so an den Gezeitenradius des Weißen Zwergs. Dort wird er zerissen und endet als zirkumstellare Gas- und Staubscheibe. Die in SDSS J0845+2257 beobachtete Variabilität der Linienprofile innerhalb von nur vier Jahren legt den Schluss nahe, dass sich die Struktur der Debrischeiben in ständigem Wandel befindet. Ursache hierfür könnte sein, dass immer wieder neue Asteroiden durch Gezeitenkräfte zerissen und akkretiert werden (Gänsicke et al. 2008). Diese Debris-Scheiben bieten somit die einmalige Gelegenheit, die Überreste extrasolarer Planetensysteme spektroskopisch zu untersuchen und die gefundenen chemischen Häufigkeiten mit denen in unserem Sonnensystem zu vergleichen.

Ich habe mich auf die Analyse der Gasscheibe um SDSS J1228+1040 konzentriert<sup>9</sup>. Das beobachtete Spektrum zeigt stark ausgeprägte Emissionslinien des Kalziums, deren Doppelhöckerprofil typisch für eine Akkretionsscheibe ist (siehe Abb. 4.3). In einem ersten Schritt konnte das beobachtete Linienprofil mit einem Akkretions-

---

<sup>8</sup>Weiße Zwerge, deren Spektren Linien von neutralem Helium und Metallen, jedoch nicht von Wasserstoff enthalten, werden als *DBZ Weiße Zwerge* bezeichnet.

<sup>9</sup>Die Masse des Weißen Zwerges beträgt etwa  $0,77 M_{\odot}$ , dies entspricht einem Vorläuferstern von etwa  $4-5 M_{\odot}$  (Blöcker 1995). Das Vorhandensein einer Debrischeibe in SDSS J1228+1040 ist ein guter Beleg dafür, dass auch um relativ kurzlebige, massereichere Sterne Planetensysteme entstehen können.

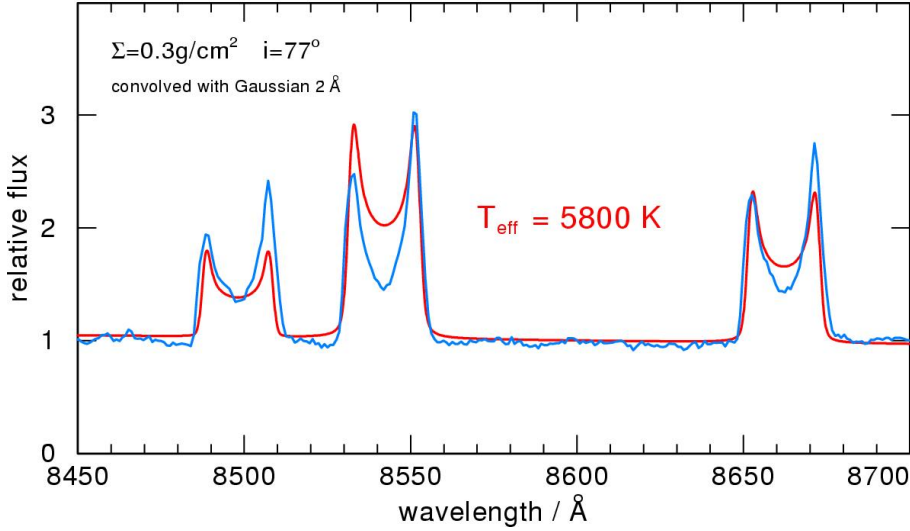


Abbildung 4.3: Vergleich eines Modellspektrums (rot) mit einem beobachteten Spektrum (blau) von SDSS J1228+1040 (Werner et al. 2009, siehe Anhang E). Der Ausschnitt zeigt das Ca II Triplet bei  $\lambda\lambda 8498, 8542, 8662 \text{ \AA}$ .

scheibenring, bestehend aus Kalzium, bei einer Entfernung von  $1.2 R_\odot$  mit einer Effektivtemperatur von  $T_{\text{eff}} \approx 6000 \text{ K}$  und einer Oberflächendichte von  $\Sigma = 3 \text{ kg/m}^2$  gut wiedergegeben werden. Ich konnte zeigen, dass die Wasserstoffhäufigkeit in der Gasscheibe kleiner als 1% sein muss. Nimmt man an, dass diese Akkretionsscheibe bis an die Oberfläche des Weißen Zwerges reicht, ergibt dies eine Masse von etwa  $10^{18} \text{ kg}$ , ein Asteroid dieser Masse hätte einen Durchmesser von etwa 160 km (Werner et al. 2009, siehe Anhang E).

Die aktuellsten Modelle enthalten neben Kalzium auch die leichten Metalle Kohlenstoff, Sauerstoff, Silizium und Magnesium, die chemischen Häufigkeiten entsprechen denen von Asteroiden unseres Sonnensystems. Da die beobachteten Linienprofile eine Asymmetrie zeigen, die möglicherweise analog zu SDSS J0845+2257 einer elliptischen bzw. asymmetrischen Akkretionsscheibe zugeschrieben werden kann (Gänsicke et al. 2008), wird die in bisherigen Modellen verwendete Axialsymmetrie aufgegeben. Erste Vergleiche von Modellrechnungen, bei denen statt einer kompletten Akkretionsscheibe ein sich nach Innen verjüngender Spiralarm simuliert wird, mit beobachteten Spektren sind bereits sehr vielversprechend (Nagel et al. in Vorb.).



# Kapitel 5

## Zusammenfassung und Ausblick

Die Erforschung von Akkretionsscheiben um kompakte, stellare Objekte hat in den vergangenen zwei Dekaden stetig an Bedeutung gewonnen. Mit der Einführung moderner Methoden zur Lösung des Strahlungstransportproblems im nicht-thermodynamischen Gleichgewicht sowie der enorm gestiegenen Rechenleistung heutiger Computer, die es erlaubt Elemente einschließlich der Eisengruppe zu berücksichtigen, ist es möglich geworden realitätsnahe synthetische Spektren für eine Vielzahl verschiedener Objektklassen zu berechnen. Dies erlaubt nun die detaillierte Untersuchung verschiedener, mit Akkretionsscheiben verbundener Phänomene, die Enträtselung der Entstehungsgeschichte ganzer Objektklassen und sogar die spektroskopische Analyse der Überreste extrasolarer Planetensysteme.

Meine Forschung der letzten Jahre umfasst sowohl die Analyse kataklymatischer Variabler und Röntgendifoppelsterne als auch die Untersuchung von Akkretionsscheiben um isolierte Objekte wie z.B. im Falle der metallreichen Debrissscheiben um Weiße Zwerge. Für einzelne AM CVn Sterne habe ich eine starke Silizium-Unterhäufigkeit und damit eine potentielle Zugehörigkeit zur Sternpopulation II gezeigt, die beobachteten Absorptions- bzw. Emissionslinienspektren lassen sich durch unterschiedliche Akkretionsraten erklären. Am Beispiel von Supernova-Fallbackscheiben habe ich unter anderem gezeigt, dass die Annahme von Schwarzkörperspektren für eine Akkretionsscheibe zu deutlich falschen Ergebnissen bzgl. der radialen Ausdehnung der Akkretionsscheibe führt.

Akkretionsscheibenmodelle werden in naher Zukunft weiter verfeinert werden müssen, um mit den qualitativ immer hochwertigeren Beobachtungsdaten Schritt halten zu können. Ein Schwerpunkt wird hierbei sein, Ergebnisse aus hydrodynamischen Rechnungen mit Strahlungstransportmodellen zu vereinigen. Erste Schritte in diese Richtung habe ich bereits unternommen. Auch die Berücksichtigung eines in einigen Systemen beobachteten strahlungsdruckgetriebenen Akkretionsscheibenwindes wurde bereits von uns in Angriff genommen. Die Spektralanalyse von Akkretionsscheiben wird auch in Zukunft eine wichtige Rolle in der Astrophysik spielen und zum Verständnis mannigfaltiger Phänomene im Universum beitragen.



# Literaturverzeichnis

- Alpar, M. A. 2001, *The Astrophysical Journal*, 554, 1245
- Bath, G. T. 1975, *Monthly Notices of the Royal Astronomical Society*, 171, 311
- Becklin, E. E., Farihi, J., Jura, M., et al. 2005, *The Astrophysical Journal*, 632, L119
- Belczyński, K., Mikolajewska, J., Munari, U., Ivison, R. J., & Friedjung, M. 2000, *Astronomy and Astrophysics Supplement*, 146, 407
- Blackman, E. G. & Perna, R. 2004, *The Astrophysical Journal*, 601, L71
- Blöcker, T. 1995, *Astronomy and Astrophysics*, 299, 755
- Brinkworth, C. S., Gänsicke, B. T., Marsh, T. R., Hoard, D. W., & Tappert, C. 2009, *The Astrophysical Journal*, 696, 1402
- Brown, E. F. & Bildsten, L. 1998, *The Astrophysical Journal*, 496, 915
- Cannizzo, J. K. & Cameron, A. G. W. 1988, *The Astrophysical Journal*, 330, 327
- Cannizzo, J. K. & Wheeler, J. C. 1984, *The Astrophysical Journal Supplement Series*, 55, 367
- Chatterjee, P., Hernquist, L., & Narayan, R. 2000, *The Astrophysical Journal*, 534, 373
- Debes, J. H. & Sigurdsson, S. 2002, *The Astrophysical Journal*, 572, 556
- Diaz, M. P., Wade, R. A., & Hubeny, I. 1996, *The Astrophysical Journal*, 459, 236
- Dörrer, T., Riffert, H., Staubert, R., & Ruder, H. 1996, *Astronomy and Astrophysics*, 311, 69
- Ertan, Ü. & Alpar, M. A. 2003, *The Astrophysical Journal*, 593, L93
- Ertan, Ü., Erkut, M. H., Eksi, K. Y., & Alpar, M. A. 2007, *The Astrophysical Journal*, 657, 441
- Farihi, J., Jura, M., & Zuckerman, B. 2009, *The Astrophysical Journal*, 694, 805

- Farihi, J., Jura, M., Zuckerman, B., & Melis, C. 2007, Bulletin of the American Astronomical Society, 211, 814
- Gänsicke, B. T., Koester, D., Marsh, T. R., Rebassa-Mansergas, A., & Southworth, J. 2008, Monthly Notices of the Royal Astronomical Society, 391, L103
- Gänsicke, B. T., Marsh, T. R., Southworth, J., & Rebassa-Mansergas, A. 2006, Science, 314, 1908
- Gilmozzi, R., Cassatella, A., Clavel, J., et al. 1987, Nature, 328, 318
- Graham, J. R., Matthews, K., Neugebauer, G., & Soifer, B. T. 1990, The Astrophysical Journal, 357, 216
- Graves, G. J. M., Challis, P. M., Chevalier, R. A., et al. 2005, The Astrophysical Journal, 629, 944
- Hawley, J. F. & Balbus, S. A. 1998, Wild Stars In The Old West: Proceedings of the 13th North American Workshop on Cataclysmic Variables and Related Objects, eds. S. Howell, E. Kuulkers, & C. Woodward, ASP Conference Series, 137, 273
- Hellier, C. 2001, Cataclysmic Variable Stars, Springer Praxis Books
- Hessman, F. V., Robinson, E. L., Nather, R. E., & Zhang, E.-H. 1984, The Astrophysical Journal, 286, 747
- Hils, D. & Bender, P. L. 2000, The Astrophysical Journal, 537, 334
- Hubeny, I. & Hubeny, V. 1997, The Astrophysical Journal, 484, L37
- Israel, G. L., Rea, N., Mangano, V., et al. 2004, The Astrophysical Journal, 603, L97
- Juett, A. M. & Chakrabarty, D. 2003, The Astrophysical Journal, 599, 498
- Juett, A. M. & Chakrabarty, D. 2005, The Astrophysical Journal, 627, 926
- Jura, M. 2003, The Astrophysical Journal, 584, L91
- Kilic, M., von Hippel, T., Leggett, S. K., & Winget, D. E. 2005, The Astrophysical Journal, 632, L115
- Kilic, M., von Hippel, T., Leggett, S. K., & Winget, D. E. 2006, The Astrophysical Journal, 646, 474
- Kiplinger, A. L. 1979, The Astrophysical Journal, 234, 997
- Kippenhahn, R. & Weigert, A. 1994, Stellar Structure and Evolution, Springer Verlag
- Koester, D., Provencal, J., & Shipman, H. L. 1997, Astronomy and Astrophysics, 320, L57
- Korčáková, D., Votruba, V., Kubát, J., et al. 2009, eds. I. Hubeny, J.M. Stone, K. MacGregor, & K. Werner, AIP Conference Proceedings, 1171, 359

- Kriz, S. & Hubeny, I. 1986, Bulletin of the Astronomical Institutes of Czechoslovakia, 37, 129
- Kromer, M., Nagel, T., & Werner, K. 2007, Astronomy and Astrophysics, 475, 301
- Kurucz, R. L. 1979, The Astrophysical Journal Supplement Series, 40, 1
- Kurucz, R. L. 1991, NATO ASIC Proc. 341: Stellar Atmospheres: Beyond Classical Models, 441
- Kusterer, D.-J. 2008, Dissertation, Eberhard Karls Universität Tübingen
- Langer, N., Deutschmann, A., Wellstein, S., & Höflich, P. 2000, Astronomy and Astrophysics, 362, 1046
- Mayo, S. K., Wickramasinghe, D. T., & Whelan, J. A. J. 1980, Monthly Notices of the Royal Astronomical Society, 193, 793
- Meyer, F. & Meyer-Hofmeister, E. 1982, Astronomy and Astrophysics, 106, 34
- Meyer-Hofmeister, E. 1992, Astronomy and Astrophysics, 253, 459
- Misner, C. W., Thorne, K. S., & Wheeler, J. A. 1973, Gravitation, W. H. Freeman & Co.
- Nagel, T. 2003, Dissertation, Eberhard Karls Universität Tübingen
- Nagel, T., Dreizler, S., Rauch, T., & Werner, K. 2004, Astronomy and Astrophysics, 428, 109
- Nagel, T., Dreizler, S., & Werner, K. 2003, Symbiotic Stars Probing Stellar Evolution, eds. R. L. M. Corradi, J. Mikolajewska, & T. J. Mahoney, ASP Conference Series, 303, 482
- Nagel, T., Kusterer, D.-J., Rauch, T., & Werner, K. 2008, Hydrogen-Deficient Stars, eds. K. Werner & T. Rauch, ASP Conference Series, 391, 281
- Nagel, T., Rauch, T., & Werner, K. 2009, Astronomy and Astrophysics, 499, 773
- Nagel, T., Schuh, S., Kusterer, D.-J., et al. 2006, Astronomy and Astrophysics, 448, L25
- Nagel, T. & Werner, K. 2004, Astronomy and Astrophysics, 426, L45
- Nasser, M. R., Solheim, J.-E., & Semionoff, D. A. 2001, Astronomy and Astrophysics, 373, 222
- Nelemans, G. 2005, The Astrophysics of Cataclysmic Variables and Related Objects, eds. J.-M. Hameury & J.-P. Lasota, ASP Conference Series, 330, 27
- Nelemans, G., Steeghs, D., & Groot, P. J. 2001, Monthly Notices of the Royal Astronomical Society, 326, 621
- Nelemans, G., Yungelson, L. R., van der Sluys, M. V., & Tout, C. A. 2010, Monthly Notices of the Royal Astronomical Society, 401, 1347

- Osaki, Y. 1974, Astronomical Society of Japan, 26, 429
- Patterson, J., Walker, S., Kemp, J., et al. 2000, The Publications of the Astronomical Society of the Pacific, 112, 625
- Perna, R., Hernquist, L., & Narayan, R. 2000, The Astrophysical Journal, 541, 344
- Peterson, B. M. 1997, An Introduction to Active Galactic Nuclei, Cambridge University Press
- Provencal, J. L., Montgomery, M. H., Kanaan, A., et al. 2009a, The Astrophysical Journal, 693, 564
- Provencal, J. L., Thompson, S., Montgomery, M., et al. 2009b, 16th European Workshop on White Dwarfs, eds. E. Garcia-Berro, M. Hernanz, J. Isern, S. Torres, Journal of Physics: Conference Series, 172, 012061
- Reach, W. T., Kuchner, M. J., von Hippel, T., et al. 2005, The Astrophysical Journal, 635, L161
- Ruiz, M. T., Rojo, P. M., Garay, G., & Maza, J. 2001, The Astrophysical Journal, 552, 679
- Schuh, S., Silvotti, R., Lutz, R., et al. 2010, Astrophysics and Space Science, in press
- Shakura, N. I. & Sunyaev, R. A. 1973, Astronomy and Astrophysics, 24, 337
- Shaviv, G. & Wehrse, R. 1986, Astronomy and Astrophysics, 159, L5
- Shaviv, G. & Wehrse, R. 1989, Theory of Accretion Disks, eds. F. Meyer, NATO Advanced Science Institutes (ASI) Series C, 290, 419
- Solheim, J.-E. & Yungelson, L. R. 2005, 14th European Workshop on White Dwarfs, eds. D. Koester and S. Moehler, ASP Conference Series, 334, 387
- Störzer, H., Hauschildt, P. H., & Allard, F. 1994, The Astrophysical Journal, 437, L91
- Strohmayer, T. E. & Brown, E. F. 2002, The Astrophysical Journal, 566, 1045
- Thompson, S. E., Montgomery, M. H., von Hippel, T., et al. 2010, The Astrophysical Journal, 714, 296
- van Paradijs, J., Taam, R. E., & van den Heuvel, E. P. J. 1995, Astronomy and Astrophysics, 299, L41
- Verbunt, F. & van den Heuvel, E. P. J. 1995, X-ray binaries, Cambridge University Press
- Wade, R. A. 1988, The Astrophysical Journal, 335, 394
- Wang, Z., Chakrabarty, D., & Kaplan, D. L. 2006, Nature, 440, 772
- Warner, B. 1995, Cataclysmic Variables, Cambridge University Press

- Weisberg, J. M. & Taylor, J. H. 2005, Binary Radio Pulsars, eds. F. A. Rasio & I. H. Stairs, ASP Conference Series, 328, 25
- Werner, K., Deetjen, J. L., Dreizler, S., et al. 2003, Stellar Atmosphere Modeling, eds. I. Hubeny, D. Mihalas, & K. Werner, ASP Conference Series, 288, 31
- Werner, K., Nagel, T., & Rauch, T. 2007, *Astrophysics and Space Science*, 308, 141
- Werner, K., Nagel, T., & Rauch, T. 2009, 16th European Workshop on White Dwarfs, eds. E. Garcia-Berro, M. Hernanz, J. Isern, S. Torres, *Journal of Physics: Conference Series*, 172, 012054
- Werner, K., Nagel, T., Rauch, T., Hammer, N. J., & Dreizler, S. 2006, *Astronomy and Astrophysics*, 450, 725
- Woods, P. M. & Thompson, C. 2006, Compact stellar X-ray sources, eds. W. Lewin & M. van der Klis, Cambridge Astrophysics Series, 547
- Woosley, S. E., Heger, A., & Weaver, T. A. 2002, *Reviews of Modern Physics*, 74, 1015
- Yungelson, L. R., Nelemans, G., & van den Heuvel, E. P. J. 2002, *Astronomy and Astrophysics*, 388, 546
- Zuckerman, B. & Becklin, E. E. 1987, *Nature*, 330, 138



# Publikationsliste

## referierte Publikationen

1. Schuh, S., Silvotti, R., Lutz, R., Loeptien, B. et al. 2010, *EXOTIME: searching for planets around pulsating subdwarf B stars*, The Fourth Meeting On Hot Subdwarf Stars And Related Objects, eds. C.S. Jeffery & Jinhua He, Ap&SS, in press
2. Thompson, S. E., Montgomery, M. H.; von Hippel, T., Nitta, A. et al. 2010, *Pulsational Mapping of Calcium Across the Surface of a White Dwarf*, ApJ, 714, 296
3. Beeck, B., Schuh, S., Nagel, T., & Traulsen, I. 2009, *Towards a dynamical mass of a PG 1159 star: radial velocities and spectral analysis of SDSS J212531-010745*, CoAst., 159, 111B
4. Nagel, T., Rauch, T., & Werner, K. 2009, *A new grid of NLTE accretion-disc models for AM CVn systems: application to CE 315*, A&A, 49, 773
5. Provencal, J. L., Montgomery, M. H., Kanaan, A., Shipman, H. L., et al. 2009, *2006 Whole Earth Telescope Observations of GD358: A New Look at the Prototype DBV*, ApJ, 693, 564
6. Schuh, S., Traulsen, I., Nagel, T., Reiff, E., Homeier, D., Schwager, H., Kusterer, D.-J., Lutz, R., & Schreiber, M. R. 2008, *A new period determination for the close PG1159 binary SDSSJ212531.92-010745.9*, Astronomische Nachrichten, 329, 376
7. Costa, J. E. S., Kepler, S. O., Winget, D. E., et al. 2008, *The pulsation modes of the pre-white dwarf PG 1159-035*, A&A, 477, 627
8. Kromer, M., Nagel, T., & Werner, K. 2007, *Synthetic NLTE accretion disc spectra for the dwarf nova SS Cygni during an outburst cycle*, A&A, 475, 301
9. Werner, K., Nagel, T., Rauch, T., & Suleimanov, V. 2007, *Non-LTE models for neutron star atmospheres and SN fallback disks*, Adv. Space Res., 40, 1512
10. Werner, K., Nagel, T., & Rauch, T. 2007, *Non-LTE modeling of supernova-fallback disks*, Ap&SS, 308, 141

11. Werner, K., Nagel, T., Rauch, T., Hammer, N. J., & Dreizler, S. 2006, *VLT spectroscopy and non-LTE modeling of the C/O-dominated accretion disks in two ultracompact X-ray binaries*, A&A, 450, 725
12. Nagel, T., Schuh, S., Kusterer, D.J., Stahn, T., Hügelmeyer, S.D., Dreizler, S., Gännsicke, B.T., & Schreiber M.R. 2006, *SDSS J212531.92-010745.9 - the first definite PG1159 close binary system*, A&A, 448, L25
13. Nagel, T., Dreizler, S., Rauch, T., & Werner, K. 2004, *AcDc - A new code for the NLTE spectral analysis of accretion discs: application to the helium CV AM CVn*, A&A, 428, 109
14. Nagel, T. & Werner, K. 2004, *Detection of non-radial g-mode pulsations in the newly discovered PG 1159 star HE1429-1209*, A&A, 426, L45
15. Nagel, T. 2003, *Synthetische Spektren und Vertikalschichtungen von Akkretionsscheiben*, Dissertation, Eberhard Karls Universität Tübingen
16. Schuh, S. L., Handler, G., Drechsel, H. et al. 2003, *2MASS J0516288+260738: Discovery of the first eclipsing late K + Brown dwarf binary system?*, A&A, 410, 649
17. Kepler, S. O., Nather, R. E., Winget, D. E. et al. 2003, *The everchanging pulsating white dwarf GD358*, A&A, 401, 639
18. Schuh, S. L., Heber, U., Dreizler, S., O'Toole, S., Jeffery, C. S. et al. 2003, *PG 1605+072 in WET XCov22: Support for the Multi Site Spectroscopic Telescope*, Baltic Astronomy, 12, 55
19. Kepler, S. O., Nather, E. R., Winget, D. E. et al. 2003, *WET Observations of GD 358 in 2000*, Baltic Astronomy, 12, 45

## nicht referierte Publikationen

20. Korčáková, D., Votruba, V., Kubát, J., Werner, K., Škoda, P., & Nagel, T. 2009, *Radiative Transfer in Axial Symmetry*, Recent Directions in Astrophysical Quantitative Spectroscopy and Radiation Hydrodynamics, eds. I. Hubeny, J.M. Stone, K. MacGregor, & K. Werner, AIP Conference Proceedings, 1171, 359
21. Nagel, T., Hartmann, S., Rauch, T., & Werner, K. 2009, *Spectral Modeling of Accretion Disks around Compact Stars*, Recent Directions in Astrophysical Quantitative Spectroscopy and Radiation Hydrodynamics, eds. I. Hubeny, J.M. Stone, K. MacGregor, & K. Werner, AIP Conference Proceedings, 1171, 341
22. Provencal, J. L., Thompson, S., Montgomery, M., et al. 2009, *Preliminary XCOV26 results for EC14012-1446*, 16th European Workshop on White Dwarfs, eds. E. Garcia-Berro, M. Hernanz, J. Isern, S. Torres, Journal of Physics: Conference Series, 172, 012061

23. Schuh, S., Beeck, B., & Nagel, T. 2009, *Dynamic masses for the close PG1159 binary SDSSJ212531.92-010745.9*, 16th European Workshop on White Dwarfs, eds. E. Garcia-Berro, M. Hernanz, J. Isern, S. Torres, Journal of Physics: Conference Series, 172, 012065
24. Werner, K., Nagel, T., & Rauch, T. 2009, *Spectral modeling of gaseous metal disks around DAZ white dwarfs*, 16th European Workshop on White Dwarfs, eds. E. Garcia-Berro, M. Hernanz, J. Isern, S. Torres, Journal of Physics: Conference Series, 172, 012054
25. Kusterer, D.-J., Nagel, T., & Werner, K. 2008, *Accretion Disk Wind in AM CVn Binaries - a Monte Carlo Approach*, Hydrogen-Deficient Stars, eds. K. Werner & T. Rauch, ASP Conference Series, 391, 285
26. Nagel, T., Kusterer, D.-J., Rauch, T., & Werner, K. 2008, *Metal abundances in accretion discs of AM CVn binaries*, Hydrogen-Deficient Stars, eds. K. Werner & T. Rauch, ASP Conference Series, 391, 281
27. Schuh, S., Nagel, T., Traulsen, I., & Beeck, B. 2008, *New Light Curves and Spectra of the close PG1159 Binary System SDSSJ212531.92-010745.9*, Hydrogen-Deficient Stars, eds. K. Werner & T. Rauch, ASP Conference Series, 391, 133
28. Kusterer, D.-J., Nagel, T., Werner, K., & Feldmeier, A. 2008, *Radiative transfer in CV disk winds*, in Clumping in Hot Star Winds, eds. W.-R. Hamann, A. Feldmeier, & L. Oschinova, Potsdam: Universitätsverlag
29. Schuh, S. & Nagel, T. 2007, *The First PG 1159 Close Binary System*, in 15th European Workshop on White Dwarfs, eds. R. Napiwotzki & M. R. Burleigh, ASP Conference Series, 372, 491
30. Werner, K., Nagel, T., & Rauch, T. 2007, *Limits on iron-dominated fallback disk in SN 1987A*, in Supernova 1987A: 20 years after, eds. S. Immler, K. Weiler, & R. McCray, American Institute of Physics Conference Proceedings, 937, 81
31. Lahulla, F., Allen, R. L., Garcia, J., Schuh, S., Nagel, T., & Göhler, E. 2006, Minor Planet Observations [493 Calar Alto], Minor Planet Circular 56155, 5
32. Werner, K., Rauch, T., Suleimanov, V., & Nagel, T. 2006, *Non-LTE models for neutron star atmospheres and SN fallback disks*, 36th COSPAR Scientific Assembly, COSPAR, Plenary Meeting, 36, 2213
33. Werner, K., Hammer, N.J., Nagel, T., Rauch, T., & Dreizler, S. 2005, *On Possible Oxygen/Neon White Dwarfs: H1504+65 and the White Dwarf Donors in Ultracompact X-ray Binaries*, 14th European Workshop on White Dwarfs, eds. D. Koester, S. Moehler, ASP Conference Series, 334, 165
34. Nagel, T., & Werner, K. 2005, *Detection of non-radial g-mode pulsations in the newly discovered PG1159 star HE 1429-1209*, 14th European Workshop on White Dwarfs, eds. D. Koester, S. Moehler, ASP Conference Series, 334, 647

35. Nagel, T., Hammer, N. J., Rauch, T., Werner, K., & Dreizler, S. 2005, *NLTE Spectral Analysis of Accretion Discs in Ultracompact X-ray Binaries*, The Astrophysics of Cataclysmic Variables and Related Objects, eds. J.-M. Hameury & J.-P. Lasota, ASP Conference Series, 330, 73
36. Hammer, N. J., Kusterer, D.-J., Nagel, T., Rauch, T., Werner, K., & Dreizler, S. 2005, *Modelling C/O/Ne dominated accretion discs in ultra-compact X-ray binaries*, The Astrophysics of Cataclysmic Variables and Related Objects, eds. J.-M. Hameury & J.-P. Lasota, ASP Conference Series, 330, 333
37. Kellermann, T., Nagel, T., Hammer, N. J., & Werner, K. 2005, *Accretion Disc Models in Quiescence and Outburst*, The Astrophysics of Cataclysmic Variables and Related Objects, eds. J.-M. Hameury & J.-P. Lasota, ASP Conference Series, 330, 391
38. Werner, K., Nagel, T., Dreizler, S., & Rauch, T. 2004, *Modeling of Oxygen-Neon Dominated Accretion Disks in Ultracompact X-ray Binaries: 4U 1626-67*, IAU Colloquium 194, eds. G. Tovmassian & E. Sion, RevMexAA Conference Series, 20, 146
39. Nagel, T., Rauch, T., Dreizler, S., & Werner, K. 2004, Modeling He-rich Disks in AM CVn Binaries, IAU Colloquium 194, eds. G. Tovmassian & E. Sion, RevMexAA Conference Series, 20, 228
40. Hammer, N., Nagel, T., & Werner, K. 2003, *A New Class of Ultracompact Binary Systems*, Astronomische Nachrichten Supplement, 324, 142
41. Nagel, T., Dreizler, S., & Werner, K. 2003, *Synthetic Spectra of Accretion Disks*, Astronomische Nachrichten Supplement, 324, 64
42. Nagel, T., Dreizler, S., & Werner, K. 2003, *Vertical Structures and Spectra of Accretion Disks in Symbiotic Stars*, Symbiotic Stars probing Stellar Evolution, eds. R. L. M. Corradi, J. Mikolajewska, & T. J. Mahoney, ASP Conference Series, 303, 482
43. Nagel, T., Dreizler, S., & Werner, K. 2003, *Calculating spectra of accretion disks in AM CVn systems*, White Dwarfs, eds. D. de Martino, R. Silvotti, J.-E. Solheim, & R. Kalytis, NATO Science Series II – Mathematics, Physics and Chemistry, 105 , 357
44. Nagel, T., Dreizler, S., Rauch, T., & Werner, K. 2003, *Modeling He-rich Disks in Am CVn Binaries*, KITP Conference: Globular Clusters: Formation, Evolution and the Role of Compact Objects
45. Nagel, T., Dreizler, S., & Werner, K. 2003, *Calculating Vertical Structures and Spectra of Accretion Disks with the New Code AcDc*, Stellar Atmosphere Modeling, eds. I. Hubeny, D. Mihalas, & K. Werner, ASP Conference Series, 288, 641
46. Schuh, S. L., Nagel, T., Deetjen, J. L., Dreizler, S., Handler, G. et al. 2003, *Preliminary results of the WET Xcov22 campaign at Calar Alto Observatory*, White Dwarfs, eds. D. de Martino, R. Silvotti, J.-E. Solheim, & R. Kalytis, NATO Science Series II – Mathematics, Physics and Chemistry, 105, 263

47. Werner, K., Deetjen, J.L., Dreizler, S., Nagel, T., & Rauch, T. 2003, *Stellar Atmosphere and Accretion Disk Models for the Hot Component in Symbiotic Stars*, Symbiotic Stars probing Stellar Evolution, eds. R. L. M. Corradi, J. Mikolajewska, & T. J. Mahoney, ASP Conference Series, 303, 303
48. Werner, K., Dreizler, S., Deetjen, J. L., Nagel, T., Rauch, T., & Schuh, S. L. 2003, *Model Photospheres with Accelerated Lambda Iteration*, Stellar Atmosphere Modeling, eds. I. Hubeny, D. Mihalas, & K. Werner, ASP Conference Series, 288, 31
49. Werner, K., Nagel, T., Dreizler, S., & Rauch, T. 2003, *Modeling C/O/Ne Dominated Accretion in Ultracompact X-ray Binaries*, KITP Conference: Globular Clusters: Formation, Evolution and the Role of Compact Objects, electronic proceedings, [http://online.kitp.ucsb.edu/online/ultra\\_c03/](http://online.kitp.ucsb.edu/online/ultra_c03/)
50. Nagel, T., Dreizler, S., & Werner, K. 2002, *AcDc – A new code to calculate vertical structures and spectra of accretion disks*, The Physics of Cataclysmic Variables and Related Objects, eds. B. T. Gänsicke, K. Beuermann, & K. Reinsch, ASP Conference Series, 261, 509
51. Nagel, T., Dreizler, S., & Werner, K. 2001, *Sphericity Effects in Metal-Line Blanketed NLTE Model Atmospheres*, 12th European Workshop on White Dwarfs, eds. J. L. Provencal, H. L. Shipman, J. MacDonald, & S. Goodchild, ASP Conference Series, 226, 86



# Anhang A

## Synthetic NLTE accretion disc spectra for the dwarf nova SS Cygni during an outburst cycle

M. Kromer, T. Nagel , and K. Werner

### **Abstract**

*Context.* Dwarf nova outbursts result from enhanced mass transport through the accretion disc of a cataclysmic variable system.

*Aims.* We assess the question of whether these outbursts are caused by an enhanced mass transfer from the late-type main sequence star onto the white dwarf (so-called mass transfer instability model, MTI) or by a thermal instability in the accretion disc (disc instability model, DIM).

*Methods.* We compute non-LTE models and spectra of accretion discs in quiescence and outburst and construct spectral time sequences for discs over a complete outburst cycle. We then compare our spectra to published optical spectroscopy of the dwarf nova SS Cygni. In particular, we investigate the hydrogen and helium line profiles that are turning from emission into absorption during the rise to outburst.

*Results.* The evolution of the hydrogen and helium line profiles during the rise to outburst and decline clearly favour the disc instability model. Our spectral model sequences allow us to distinguish inside-out and outside-in moving heating waves in the disc of SS Cygni, which can be related to symmetric and asymmetric outburst light curves, respectively.

## Synthetic NLTE accretion disc spectra for the dwarf nova SS Cygni during an outburst cycle

M. Kromer<sup>1,2</sup>, T. Nagel<sup>1</sup>, and K. Werner<sup>1</sup>

<sup>1</sup> Institut für Astronomie und Astrophysik, Universität Tübingen, Sand 1, 72076 Tübingen, Germany  
 e-mail: nage1@astro.uni-tuebingen.de

<sup>2</sup> Max-Planck-Institut für Astrophysik, Karl-Schwarzschild-Straße 1, 85741 Garching, Germany

Received 16 May 2007 / Accepted 14 August 2007

### ABSTRACT

**Context.** Dwarf nova outbursts result from enhanced mass transport through the accretion disc of a cataclysmic variable system.

**Aims.** We assess the question of whether these outbursts are caused by an enhanced mass transfer from the late-type main sequence star onto the white dwarf (so-called mass transfer instability model, MTI) or by a thermal instability in the accretion disc (disc instability model, DIM).

**Methods.** We compute non-LTE models and spectra of accretion discs in quiescence and outburst and construct spectral time sequences for discs over a complete outburst cycle. We then compare our spectra to published optical spectroscopy of the dwarf nova SS Cygni. In particular, we investigate the hydrogen and helium line profiles that are turning from emission into absorption during the rise to outburst.

**Results.** The evolution of the hydrogen and helium line profiles during the rise to outburst and decline clearly favour the disc instability model. Our spectral model sequences allow us to distinguish inside-out and outside-in moving heating waves in the disc of SS Cygni, which can be related to symmetric and asymmetric outburst light curves, respectively.

**Key words.** accretion, accretion disks – stars: dwarf novae – stars: binaries: close

### 1. Introduction

Dwarf novae (DN) belong to the non-magnetic cataclysmic variables which are binary systems consisting of a white dwarf as primary component and an orbiting late-type main sequence star. Due to their close orbit, mass transfer from the secondary onto the primary via Roche lobe overflow occurs. Because of conservation of angular momentum an accretion disc forms around the white dwarf (Warner 1995).

Dwarf novae are characterised by more or less regular outbursts during which the system undergoes a rise in optical brightness of 2–6 mag. The observed outbursts can be divided into two categories, depending whether the lightcurves are symmetric or not. For asymmetric outbursts they are characterised by a fast rise and slower decline and show a delay of the rise in the UV against the optical. For symmetric outbursts UV and optical fluxes rise simultaneously on a longer timescale than the asymmetric outbursts. Sometimes for both types plateaus are observed during maximum. It is commonly accepted that the outbursts are caused by a luminosity increase in the disc that arises from a temporarily increased mass transport through the disc. The origin of this increased mass transport, however, has been discussed controversially.

According to the mass transfer instability model (MTI, Bath 1975) an instability in the secondary star leads to a temporarily increased mass transfer rate  $\dot{M}_2$  from the secondary onto the disc, so that also the mass transport through the disc increases. Because the instability originates in the secondary, the outbursts must start at the outer edge of the disc and proceed inwards in the framework of this model.

In the disc instability model (DIM, Osaki 1974) the mass transfer from the secondary is constant and the outbursts are attributed to thermal viscous instabilities in the disc that lead to a temporarily increased mass transport through the disc. Meyer & Meyer-Hofmeister (1981) and Faulkner et al. (1983) have shown that this instability is due to the local ionisation of hydrogen. Radial temperature and viscosity gradients lead to the propagation of heating or cooling waves throughout the disc, which carry the whole disc over to outburst or quiescence, respectively. In particular this allows the outbursts to start any place in the disc so that outbursts can proceed inwards or outwards.

Today the DIM is generally favoured over the MTI. This is due to the existence of a detailed theoretical framework for the DIM that can explain the outburst behaviour and the different outburst types in a natural manner. According to Smak (1984a) the different rise times for asymmetric and symmetric outbursts are caused by different propagation directions of the outbursts: for the asymmetric outbursts (type-A after Smak 1984a) the heating wave originates in the outer part of the disc and proceeds inside moving with the mass stream, so that the heating wave can move relatively fast. Finally the hot inner part of the disc switches to outburst, so that the rise in the UV is delayed against the optical. In contrast to the symmetric type-B outbursts, the heating wave proceeds inside-out and therefore has to move against the mass stream, resulting in a relatively slow rise. In this case the hot inner parts of the disc are the first to switch to outburst so that optical and UV fluxes increase simultaneously.

Furthermore, that no luminosity increase in the hotspot – the region of the disc, where the mass stream from the secondary impinges – is observed during an outburst contradicts the MTI

model, because such a luminosity increase would be expected if the mass transfer from the secondary increases.

A possibility of distinguishing between both models by observational data arises if one is able to decide whether the outbursts proceed outside-in or inside-out. This can be achieved by comparing time-resolved spectra for an entire outburst cycle with the appropriate model spectra because quiescence and outburst spectra differ significantly. In quiescence the optical spectrum shows the strong hydrogen Balmer emission lines characteristic of an optically thin disc. In contrast, during outburst, broad absorption features in the Balmer series indicate an optically thick disc. At the same time, the intensity in the blue wavelength range increases particularly strongly indicating a rise in the disc temperature.

To this end we calculated time-resolved model spectra (Sect. 3) tailored to the dwarf nova SS Cyg. This is the brightest known DN, showing an outburst brightness of  $V = 8.2$  mag (Ritter & Kolb 2003), making it one of the best-studied DN. Before presenting these models in Sect. 3, we give a short overview of our approach in Sect. 2. The results are discussed in Sect. 4.

## 2. Model assumptions

To calculate the accretion disc spectra we use our accretion disc code AcDc (Nagel 2003; Nagel et al. 2004), which is based on the assumption of a geometrically thin disc (total disc thickness  $H$  is much smaller than the disc diameter). This allows us to decouple vertical and radial structures and, together with the assumption of axial symmetry, to separate the disc into concentric annuli of plane-parallel geometry. Then radiative transfer becomes a one-dimensional problem.

Each of these disc rings, which are located at a given radial distance  $r$  from the white dwarf, is assumed to be stationary. Thus it can be characterised by a constant mass transport rate  $\dot{M}$ . The rate of energy generation from viscous shear then becomes independent of the kinematic viscosity  $\nu_k$  and can be parameterised by the effective temperature

$$T_{\text{eff}}(r) = \left[ \frac{3GM_1\dot{M}}{8\pi\sigma r^3} \left( 1 - \sqrt{\frac{r_1}{r}} \right) \right]^{1/4} \quad (1)$$

(for example Warner 1995). Thereby  $M_1$  denotes the mass,  $r_1$  the radius of the primary white dwarf,  $G$  the gravitational constant, and  $\sigma$  the Stefan-Boltzmann constant.

To get a self-consistent solution, the radiative transfer equation, the hydrostatic and energy equilibrium equations, as well as the NLTE rate equations, that determine the occupation numbers of the atomic levels, are solved simultaneously by an iterative scheme. Therefore detailed information about the involved atomic levels is needed, which is provided in the form of a model atom (cf. Rauch & Deetjen 2003). The kinematic viscosity, which is needed for the vertical structure calculation, can be parameterised by the  $\alpha$ -approach of Shakura & Sunyaev (1973)

$$\nu_k = \alpha c_s H \quad (2)$$

(where  $c_s$  is the speed of sound and  $\alpha \leq 1$  a dimensionless parameter) or after Lynden-Bell & Pringle (1974) by the Reynolds number  $Re$

$$\nu_k = \frac{rv_\phi}{Re} = \frac{\sqrt{GM_1r}}{Re}, \quad (3)$$

where  $v_\phi$  is the Kepler velocity. We choose the latter approach that is numerically easier to implement because we save a further iteration to solve consistently for  $c_s$  and  $H$ .

Irradiation of the disc by the primary is considered via the upper boundary condition for the radiative transfer equation. For that purpose the irradiation angle  $\beta$  for each disc ring and the spectrum of the primary must be specified. The spectrum of the primary is parameterised by a blackbody temperature  $T_{\text{bb}}$ , or detailed white dwarf model atmosphere spectra are calculated.

The complete set of input parameters, which we must provide for each disc ring, thus consists of  $M_1, r_1, \dot{M}, r, Re, \beta, T_{\text{bb}}$ . The spectrum of the complete disc is then obtained by integrating the spectra of these disc rings for different inclination angles, the spectral lines are Doppler shifted according to the radial component of the Keplerian rotation velocity in the disc.

As the accretion discs of dwarf novae are fed by a late-type main sequence star, we assume a disc composition of hydrogen and helium with relative solar abundances. The model atoms used for the disc model calculations presented here contain the ionisation stages H I, H II, and He I–He III. The number of NLTE levels and lines considered is 15 and 105 for H I, 29 and 61 for He I, and 14 and 78 for He II. We consider the H<sup>-</sup> opacity and Rayleigh scattering for H and He, which is important for the coolest regions of the disc model. In addition, the Ly <sub>$\alpha$</sub>  line in the cool models for the quiescent disk is so broad that it contributes considerably to the source function in the optical band. The reason is that most of the hydrogen (about 90–99%) is neutral throughout most of the line-forming region (Fig. 1, second panel from top).

## 3. Models

In the following we present detailed models for the accretion disc of SS Cyg in outburst and quiescence. SS Cyg is the brightest known DN and belongs to the U Gem type of DN. For our models we have chosen the orbital parameters according to Ritter & Kolb (2003), who give  $M_1 = (1.19 \pm 0.02) M_\odot$  for the mass of the white dwarf. According to the mass-radius relation, this corresponds to a white dwarf radius of  $3.9 \times 10^8$  cm. Together with the mass of the companion  $M_2 = (0.704 \pm 0.002) M_\odot$  and the orbital period  $P = 6.6031$  h, the tidal radius – the radius where the disc is disrupted by tidal interactions with the secondary – follows from

$$r_{\text{tidal}} = 0.60 \cdot \frac{a}{1+q} \quad (4)$$

(Hellier 2001) and amounts to  $r_{\text{tidal}} = 5.78 \times 10^{10}$  cm. Here  $a$  denotes the distance between primary and secondary, and it can be calculated from the third Kepler law.  $q$  is the mass ratio  $\frac{M_2}{M_1}$ . The minimal extension of the disc is given by the so-called circularisation radius

$$r_{\text{circ}} = r_{L_1}^4 \cdot \frac{1+q}{a^3} \quad (5)$$

at which the angular momentum is equal to the angular momentum at the Lagrange point L<sub>1</sub>. The Roche lobe and therefore the distance  $r_{L_1}$  of the Lagrange point L<sub>1</sub> must be calculated numerically. After Plavec & Kratochvil (1964), however, for  $0.1 < q < 10$  the approximation

$$r_{L_1} = a \cdot (0.500 - 0.227 \log q) \quad (6)$$

is possible. This finally leads to  $r_{\text{circ}} = 1.65 \times 10^{10}$  cm. In this radial range we have increased the disc's outer edge  $r_o$  until the double-peaked line profiles matched the observation, so we chose  $r_o = 4 \times 10^{10}$  cm. A lower value would give line profiles

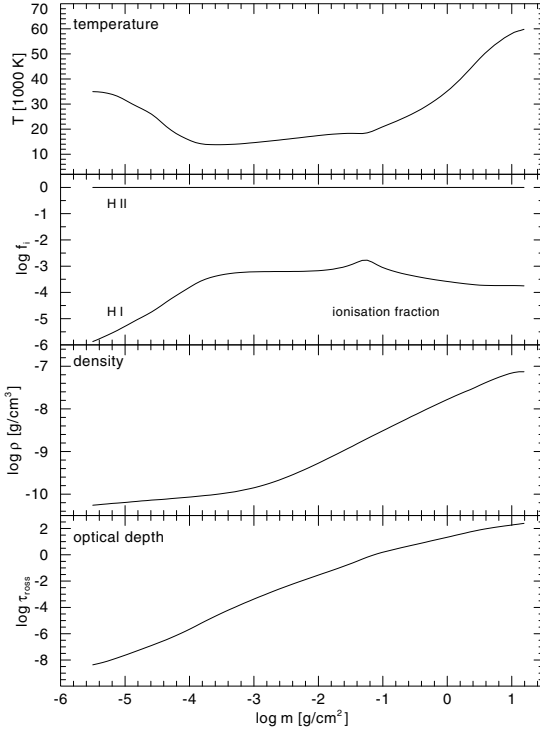


**Fig. 1.** Vertical structure of the hot disc at a distance of  $7.35 \times 10^9$  cm from the white dwarf. The physical variables are plotted against the column mass measured from the surface towards the midplane.

that are too broad due to the higher Kepler rotation velocity for smaller radii.

The inner edge of the disc model was fixed from the following arguments. Our model cannot be applied to the boundary layer expected at the transition from the disc to the primary, so we must truncate the disc well before the white dwarf. Despite the higher temperatures in the inner disc, this has little influence on the optical spectrum because the surface area of the inner parts of the disc is much smaller than that of the outer parts. Thus the inner parts can be neglected for modelling optical spectra. In contrast, in the UV range there will be strong imprints from the inner disc portions (cf. Fig. 2).

For the inclination angle  $i$  we have chosen  $40^\circ$ , which is consistent with the value of  $i = (37 \pm 5)^\circ$  given by Ritter & Kolb (2003). All disc rings have been irradiated with a 50 000 K blackbody spectrum. This temperature is compatible with the observational results for the WD in SS Cyg (Long et al. 2005; Smak 1984b). Tests with a 50 000 K white dwarf model atmosphere have shown that the blackbody approximation has little influence on the emerging disc spectra. The irradiation angle was set to  $1^\circ$ . According to the system geometry, this is possible but probably marks an upper limit. For such small angles, the irradiation increases the effective temperature of the disc ring compared to the value expected according to Eq. (2) only marginally. The relative differences are below  $10^{-3}$  and decrease with increasing  $r$ .

### 3.1. Outburst

For the hot disc during outburst, we assume a constant mass transport rate through the disc of  $\dot{M} = 4 \times 10^{-9} M_\odot/\text{yr}$  and a constant viscosity of  $\alpha \approx 0.30$  according to the DIM. With those parameters, we calculated a disc model from

**Table 1.** Parameters of the rings for the hot disc in SS Cyg.

#	$r [10^9 \text{ cm}]$	$Re$	$T_{\text{eff}} [\text{K}]$	$\tau_{\text{tot}}$	$h [10^8 \text{ cm}]$
1	1.00	3200	74 912	104	0.21
2	1.10	3200	71 056	110	0.23
3	1.22	3000	66 935	114	0.26
4	1.35	2900	63 013	119	0.30
5	1.50	2800	59 074	124	0.34
6	1.66	2600	56 742	125	0.39
7	1.84	2500	51 916	127	0.44
8	2.05	2400	48 403	128	0.50
9	2.30	2350	44 873	130	0.58
10	2.60	2300	41 350	131	0.67
11	2.97	2300	37 798	134	0.79
12	3.43	2300	34 259	139	0.93
13	4.02	2200	30 705	145	1.13
14	4.80	2100	27 135	155	1.40
15	5.85	1700	23 610	163	1.81
16	7.35	1620	20 080	192	2.38
17	9.65	1550	16 525	221	3.29
18	13.50	1450	12 969	258	4.93
19	21.00	1200	9 404	169	8.14
20	40.00	500	5 862	1.61	16.18

$\tau_{\text{tot}}$  is the total Rosseland optical depth from top to disc midplane and  $h = H/2$  the vertical extension of the disc from the midplane. The other symbols are defined in the text.

$1 \times 10^9 \text{ cm} \leq r \leq 4 \times 10^{10} \text{ cm}$  by dividing the disc into 20 rings to obtain a smooth distribution of  $T_{\text{eff}}(r)$  with a maximal difference of  $\sim 3500 \text{ K}$  between neighbouring rings (see Table 1). The resulting disc is optically thick except for the outermost ring. This ring's effective temperature of 5862 K is more typical for a cold disc.

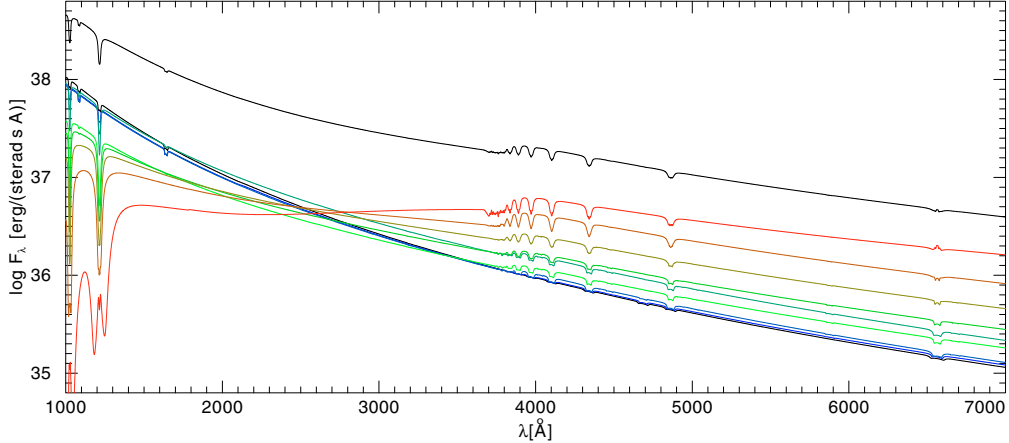
As an example of the vertical structure of the disc model, the temperature, hydrogen ionisation fraction, density, and optical depth are plotted against the height above the disc midplane in Fig. 1 at a distance of  $7.35 \times 10^9$  cm from the white dwarf. The temperature shows an inversion at the disc surface due to the heating by irradiation of the WD before a strong drop down at  $\log m \approx -4$  occurs and then the temperature rises slowly towards the disc's midplane. At  $\log m \approx -1$  the disc becomes optically thick.

Figure 2 shows the integrated spectrum of the hot disc and the contribution of selected disc rings. Doppler broadening due to the Keplerian velocity is taken into account. In the optical it is characterised by hydrogen Balmer absorption lines. In the UV, strong absorption lines of the hydrogen Lyman series and He II appear. The latter lines originate in the inner disc rings, where  $T_{\text{eff}}$  becomes high enough to populate He II levels. This high  $T_{\text{eff}}$  is also the reason the inner disc rings dominate the spectrum in the UV range despite their small surface area compared to the outer rings. The situation is completely different in the optical. There the disc spectrum is dominated by the outermost ring due to its large surface area, so the weak absorption line of He II at 4686 Å, which is visible in the inner ring spectra, is outshone by the much larger continuum flux of the outer rings.

For a comparison to observational results, Fig. 3 shows our synthetic spectrum of the hot accretion disc with the spectra of Clarke et al. (1984), who observed SS Cyg during a rise to outburst.

### 3.2. Quiescence

Wood et al. (1986) studied the radial temperature distribution in the accretion disc of the DN Z Cha by eclipse mapping. In



**Fig. 2.** Model spectra for the accretion disc of SS Cyg in outburst (uppermost curve). The other curves show the contribution of selected individual disc rings starting with the outermost ring (*top*) and then continuing towards the inner disc edge. The inclination angle is  $40^\circ$ .

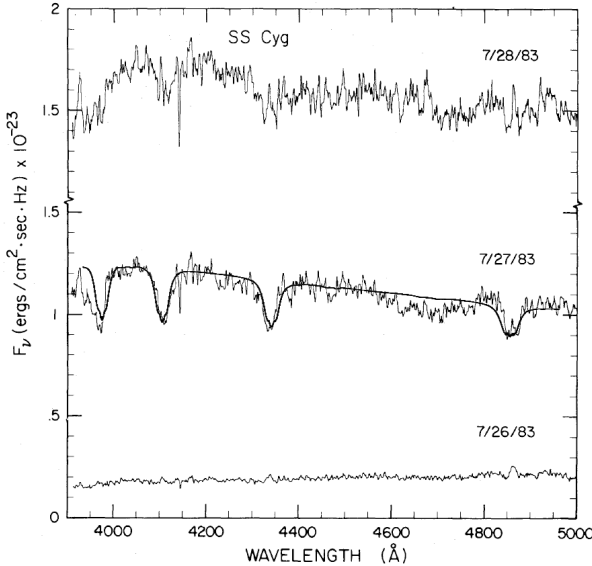


**Fig. 3.** Observed spectra of SS Cyg (from Clarke et al. 1984) during rise to outburst (outburst maximum corresponds to 7/28/83). Overplotted is our synthetic spectrum for the accretion disc in outburst. The model flux was multiplied by a constant factor to match the observed continuum flux.

contrast to the  $T_{\text{eff}} \propto r^{-3/4}$  power law expected for stationary accretion discs, they found a more or less constant value of the effective temperature at a level of several thousand Kelvin. This has been interpreted as a hint that the accretion discs of DN in quiescence are not stationary. Therefore we assumed a constant effective temperature of  $\sim 4200$  K throughout the disc, which is in the typical range for cold discs. To achieve this temperature for all rings, we adjusted the mass transport rates through the rings (see Table 2). We also adjusted the Reynolds number to get typical values for  $\alpha$  in a disc in quiescence according to the DIM. The resulting kinematic viscosity is smaller than in the hot disc by a factor of 10, except for the outermost ring, where the viscosity is as high as for disc rings in outburst. For this disc ring, it was not possible to construct a low-viscosity model with strong emission lines.

**Table 2.** Parameters for the ring models of the cold disc in SS Cyg.

#	$r [10^9 \text{ cm}]$	$\dot{M} [M_\odot/\text{yr}]$	$Re$	$\tau_{\text{tot}}$	$h [10^8 \text{ cm}]$
1	4.00	$1.4 \times 10^{-12}$	19 000	0.27	0.71
2	6.00	$4.0 \times 10^{-12}$	16 000	0.24	1.13
3	8.00	$1.0 \times 10^{-11}$	13 000	0.28	1.59
4	9.00	$1.4 \times 10^{-11}$	13 000	0.30	2.00
5	10.00	$1.9 \times 10^{-11}$	10 000	0.29	2.34
6	20.00	$1.4 \times 10^{-10}$	3000	0.28	6.00
7	40.00	$1.0 \times 10^{-9}$	500	0.22	14.56

The number of disc rings required is much smaller than for the hot disc, as the change in spectral properties across the radius is marginal due to the constant temperature. Furthermore we did not extend the cold disc as far in as the hot disc, but truncated the model at  $r = 4 \times 10^9$  cm. This is again justified by the constant effective temperature, which prevents a strong contribution of the inner rings to the UV-flux in contrast to the case of the hot disc (see Fig. 4).

The resulting disc spectrum (Fig. 4) is compared to an observed spectrum taken from Martinez-Pais et al. (1994) in Fig. 5. For that purpose the model spectrum has been normalised to the local continuum flux. In principle, the model reproduces the hydrogen Balmer emission lines, but they are not as strong as in the observation. The He I emission lines are not seen in our model spectrum, and the reason may be that they form in the hot spot, which we have not included in our models.

As an example, the vertical structure of the cold disc is shown in Fig. 6 at a radial distance of  $4.0 \times 10^{10}$  cm. In contrast to the hot disc, the temperature does not increase towards the disc midplane but declines monotonically. Towards the disc surface, the irradiation of the WD again causes a temperature inversion. The entire cold disc is optically thin.

### 3.3. Rise to outburst

To examine the spectral evolution from quiescence to outburst, we combined rings of the cold and hot discs to a sequence of disc models such that this sequence simulates the propagation of the heating wave throughout the disc. In this way we studied the two different cases of outside-in and inside-out moving heating waves to achieve further insight into the processes taking place

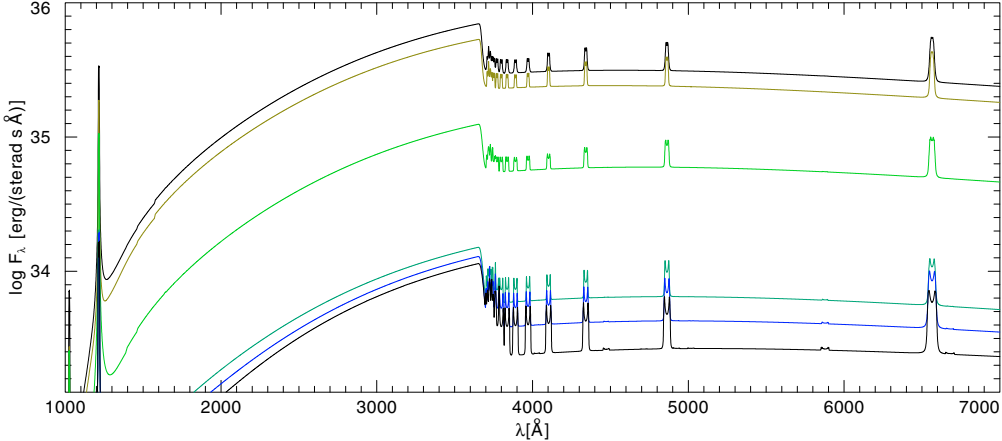


**Fig. 4.** Model spectra for the accretion disc of SS Cyg in quiescence (uppermost curve). The other curves show the contribution of selected individual disc rings starting with the outermost ring (*top*) and then continuing towards the inner disc edge. The inclination is  $40^\circ$ . The spectral lines are getting broader due to the higher Kepler velocities of the inner disc rings.

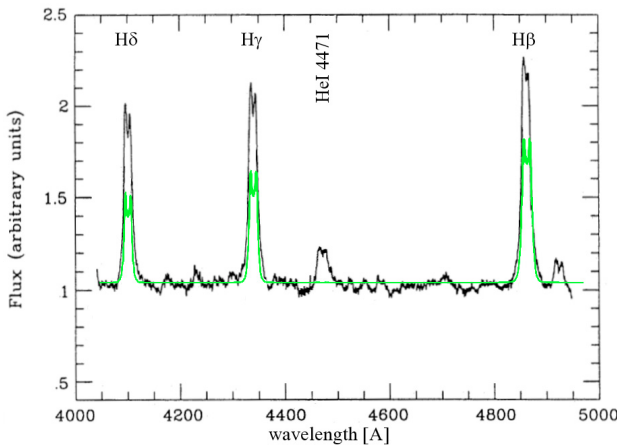


**Fig. 5.** Observed spectra of the accretion disc of SS Cyg during quiescence (Martinez-Pais et al. 1994). Overplotted is our synthetic spectrum for the accretion disc of SS Cyg in quiescence (grey). The flux was normalised to the local continuum flux.

in the disc during rise to outburst. For the outside-in outburst this sequence consists of five disc models in which the cold rings have been replaced by the next-neighbouring hot rings from the outside. The assembly of these models is shown in Table 3.

The left panel of Fig. 7 shows the spectral evolution for this sequence from a pure cold disc to full outburst, as well as the left panel of Fig. 8 where the spectra are normalised to the local continuum. The Balmer series turns from emission to absorption immediately after the outermost disk ring flipped into the hot state, because the overall disc flux in the optical is dominated by the flux of the outer rings and these are dominated by absorption in the hot state.

Similarly we modelled the inside-out outburst by a sequence of five disc models. In the first step the cold disc's innermost ring is replaced by the hot rings that lie inside of its radial position. At the same time the disc is extended inwards to the inner boundary of the hot disc at  $1 \times 10^9$  cm. For optical spectra, to which we will restrict our discussion in the following, this simplification can be justified because the inner disc rings will only contribute to the UV due to their high effective temperature and

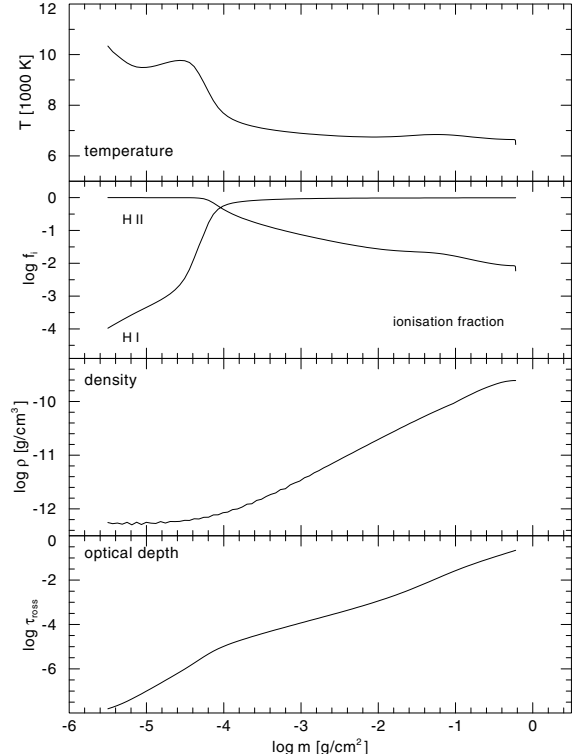


**Fig. 6.** Vertical structure of the cold disc at a distance of  $4.0 \times 10^{10}$  cm from the white dwarf. The physical variables are plotted against the column mass measured from the surface towards the midplane.

because they only cover a small surface area. In the subsequent steps, the next-neighbouring rings from the inside are replaced by hot ones. The complete assembly of the discs for the inside-out model sequence is shown in Table 4.

The right panels of Figs. 7 and 8 show the spectral evolution for this sequence from a pure cold disc to full outburst. In contrast to the outside-in scenario the hydrogen Balmer emission only diminishes slowly during rise to outburst, while increasing absorption wings appear.

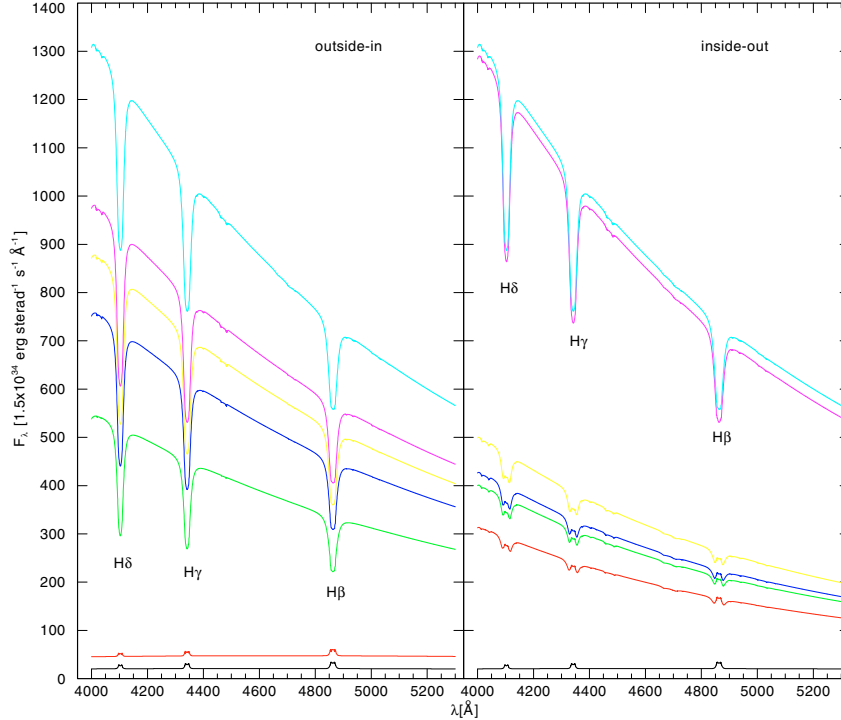


**Fig. 7.** Spectral evolution between 4000 and 5300 Å for an outside-in outburst (left panel) and an inside-out outburst (right panel). The lowermost graphs show a pure cold disc that evolves to full outburst (uppermost graph) over steps 1 to 5 of Tables 3 and 4, respectively.

**Table 3.** Assembly of disc models for the simulated outside-in outburst.

#	Step 1	Step 2	Step 3	Step 4	Step 5
1	4.00cold	4.00cold	4.00cold	4.00cold	4.00cold
2	6.00cold	6.00cold	6.00cold	6.00cold	6.00cold
3	8.00cold	8.00cold	8.00cold	8.00cold	7.35hot
4	9.00cold	9.00cold	9.00cold	9.65hot	9.65hot
5	10.0cold	10.0cold	13.5hot	13.5hot	13.5hot
6	20.0cold	21.0hot	21.0hot	21.0hot	21.0hot
7	40.0hot	40.0hot	40.0hot	40.0hot	40.0hot

Numbers in “step” columns denote the radial position of the model in  $10^9$  cm, the following “cold” or “hot” label whether a cold or hot ring was used.

One has to keep in mind that the steps of our sequences are not equidistant in time. For an outside-in outburst, for example, the heating wave moves inwards quickly; and according to our models, the spectral lines change from emission to absorption as soon as a part of the outer region is in outburst, so one will observe an absorption-line spectrum during most of the rise of an outside-in outburst. In the case of an inside-out outburst, the heating wave moves rather slowly outwards. As our models show, the line spectrum of the disk does not change to pure absorption until the outermost regions are in outburst. Hence one would observe an emission-line spectrum most of the time of an inside-out outburst.

### 3.4. Decline

Decline from outburst to quiescence is mediated by a cooling wave. This wave always propagates outside-in as argued by e.g. Warner (1995), so that the cooling can be studied by examining the inside-out moving heating wave of Table 4 in reverse order. According to the right panel of Fig. 7, the hydrogen Balmer lines evolve smoothly from absorption to pure emission.

## 4. Results and discussion

We used the models presented above to determine the nature of the outbursts in SS Cyg by comparing them to spectra available in the literature. This turned out to be rather difficult, because adequate time-resolved spectra during rise to outburst are very rare even for the well-studied case of SS Cyg.

Martinez-Pais et al. (1996) presented time-resolved spectra for different outbursts of SS Cyg. Among them are two spectra taken during a rise to an outburst of the symmetric type. According to their Fig. 2 the hydrogen Balmer emission lines decrease slowly between these two spectra, while the absorption wings increase like in the right panel of our Fig. 7 for the inside-out outburst. This leads to an identification of symmetric outbursts in SS Cyg with inside-out outbursts, which is in good agreement to Smak’s (1984a) description of type-B outbursts, but contrasts to the original conclusion of Martinez-Pais et al. (1996). They interpret the late appearance of the He II 4686 Å line as a consequence of an outside-in propagating heating wave, because they assumed that the He II 4686 Å line originates in the hot inner part of the disc. This is questionable in light of our models. The line should be significantly broader due to the higher Kepler velocity if this assumption is true.

“Some indication of an increase in the hot spot’s vertical size and, perhaps, brightness” leads them to conclude further that symmetric outbursts are connected with an instability of the secondary star, so they favoured the MTI for this outburst. This is put into question by our models, which indicate an inside-out outburst in favour of the DIM.

The observations of Clarke et al. (1984) cover a complete outburst cycle of SS Cyg. The outburst shows an asymmetric light curve. Three of its spectra before and during rise, as well as during maximum, are shown in Fig. 3. The spectral evolution of this outburst differs significantly from what was observed by Martinez-Pais et al. (1996): quiescent Balmer line emission abruptly disappears at the onset of rise to maximum, before full

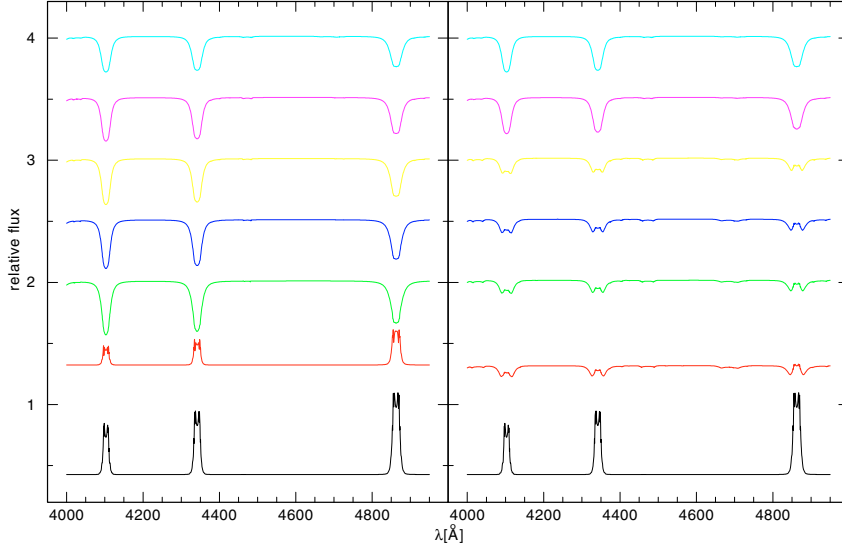


**Fig. 8.** Spectral evolution between 4000 and 5300 Å for an outside-in outburst (left panel) and an inside-out outburst (right panel). The spectra are normalised to the local continuum. The lowermost graphs show a pure cold disc that evolves to full outburst (uppermost graph) over steps 1 to 5 of Tables 3 and 4, respectively.

**Table 4.** Assembly of disc models for the simulated inside-out outburst.

#	Step 1	Step 2	Step 3	Step 4	Step 5
1	1.00hot	1.00hot	1.00hot	1.00hot	1.00hot
2	1.10hot	1.10hot	1.10hot	1.10hot	1.10hot
3	1.22hot	1.22hot	1.22hot	1.22hot	1.22hot
4	1.35hot	1.35hot	1.35hot	1.35hot	1.35hot
5	1.50hot	1.50hot	1.50hot	1.50hot	1.50hot
6	1.66hot	1.66hot	1.66hot	1.66hot	1.66hot
7	1.84hot	1.84hot	1.84hot	1.84hot	1.84hot
8	2.05hot	2.05hot	2.05hot	2.05hot	2.05hot
9	2.30hot	2.30hot	2.30hot	2.30hot	2.30hot
10	2.60hot	2.60hot	2.60hot	2.60hot	2.60hot
11	2.97hot	2.97hot	2.97hot	2.97hot	2.97hot
12	3.43hot	3.43hot	3.43hot	3.43hot	3.43hot
13	4.02hot	4.02hot	4.02hot	4.02hot	4.02hot
14	4.80hot	4.80hot	4.80hot	4.80hot	4.80hot
15	5.85hot	5.85hot	5.85hot	5.85hot	5.85hot
16	6.00cold	7.35hot	7.35hot	7.35hot	7.35hot
17	8.00cold	8.00cold	9.00cold	9.65hot	9.65hot
18	9.00cold	9.00cold	10.00cold	10.00cold	13.5hot
19	10.00cold	10.00cold	20.00cold	20.00cold	21.0hot
20	20.00cold	20.00cold	40.00cold	40.00cold	40.0cold
21	40.00cold	40.00cold	—	—	—

absorption sets in during the rise. This fits our outside-in model sequence, indicating that the asymmetric outbursts are indeed connected to outside-in, i.e. type-A outbursts following Smak (1984a).

The fact that the observed spectra of Clarke et al. (1984) during full maximum do not show pure absorption lines like our model might be a consequence of the radial extension of the disc during outburst. This is not considered in our model, although it is expected in the DIM due to the higher transport of angular momentum during outburst. It might be possible that this portion of the disc outshines the basic inner part of the disc due to its large surface area. If this portion of the disc then has comparable properties to the current outermost grid point, which is relatively cool and emission-dominated, or at least continuum-dominated, the resulting model spectrum of the extended disc might show no absorption lines anymore.

For decline from outburst to quiescence, another study by Hessman et al. (1984) exists. Their Fig. 5 is in good agreement with the right panel of our Fig. 7 if read from top to bottom, which means that they witnessed an outside-in propagating cooling wave. This again agrees with the DIM.

During decline the 4686 Å line of He II often shows a prominent emission feature like in the study of Hessman et al. (1984). This does not appear in our model. If it originates in the disc, it must arise from the inner parts, because only there does  $T_{\text{eff}}$  become high enough to populate He II levels. Accordingly, the inner rings of our hot disc model show He II 4686 Å, however, not in emission but in absorption. This supports the results of Unda-Sanzana et al. (2006), which identified the gas stream/disc impact region as the origin of the He II 4686 Å emission by means of Doppler tomography.

That Hessman et al. (1984) observed central emission peaks in the Balmer lines right from the beginning of the decline might be indicating that not the complete disc but only the inner parts participated in the outburst. If for example the disc stays cold for  $r > 10 \times 10^{10}$  cm, we only have to compare the lower five curves of the right panel in Fig. 7 to the observation. As Hessman et al. (1984) observed a short outburst without plateau, this would be again in good agreement with the DIM. There the short outbursts are attributed to discs that are not completely in outburst, while plateaus are supposed to appear if matter is accreted with a constant rate through a disc that is completely in outburst.

It will be interesting to extend our study to the UV range where especially the C IV 1550 Å line shows a similar behaviour to the Balmer lines. For that purpose, heavier elements must be included in the model calculations, and the influence of the disc wind, which becomes obvious in the P Cyg shaped profile of the C IV 1550 Å line in outburst, will be considered.

Another question is the influence of metal opacities, which we have neglected here, on the hydrogen and helium lines. From our experience in working on stellar atmospheres (O and sdO stars), we would predict that metal line blanketing and surface cooling will produce slightly deeper H and He absorption lines in the hot disk; however, we expect no qualitative change in the optical spectrum. The situation is different in the cool ring models, which are optically thin. Work is in progress to investigate the metal line blanketing problem.

## 5. Summary

In this paper, we have presented NLTE model calculations for the accretion disc of SS Cyg in outburst and quiescence. The resulting synthetic spectra describe the observed optical spectra and their transition well from absorption during outburst to emission during quiescence.

Simulations of the spectral evolution for outside-in and inside-out propagating heating waves were carried out. We compared them to published observations and conclude that symmetric outbursts belong to the inside-out type. This confirms DIM expectations (e.g. Smak 1984a), which are based on rise-time arguments and explicitly excludes the MTI model. In contrast, asymmetric outbursts seem to be outside-in outbursts.

## References

- Bath, G. T. 1975, MNRAS, 171, 311  
 Clarke, J. T., Bowyer, S., & Capel, D. 1984, ApJ, 287, 845  
 Faulkner, J., Lin, D. N. C., & Papaloizou, J. 1983, MNRAS, 205, 359  
 Hellier, C. 2001, Cataclysmic Variable Stars (Springer Praxis)
- Hessman, F. V., Robinson, E. L., Nather, R. E., & Zhang, E.-H. 1984, ApJ, 286, 747  
 Long, K. S., Froning, C. S., Knigge, C., et al. 2005, ApJ, 630, 511  
 Lynden-Bell, D., & Pringle, J. E. 1974, MNRAS, 168, 603  
 Martinez-Pais, I. G., Giovannelli, F., Rossi, C., & Gaudenzi, S. 1994, A&A, 291, 455  
 Martinez-Pais, I. G., Giovannelli, F., Rossi, C., & Gaudenzi, S. 1996, A&A, 308, 833  
 Meyer, F., & Meyer-Hofmeister, E. 1981, A&A, 104, L10  
 Nagel, T. 2003, Ph.D. Thesis, Eberhard-Karls-Universität Tübingen  
 Nagel, T., Dreizler, S., Rauch, T., & Werner, K. 2004, A&A, 428, 109  
 Osaki, Y. 1974, PASJ, 26, 429  
 Plavec, M., & Kratochvil, P. 1964, Bull. Astr. Inst. Czechosl., 15, 165  
 Rauch, T., & Deetjen, J. L. 2003, in Stellar Atmosphere Modelling, ed. I. Hubeny, D. Mihalas, & K. Werner, ASP Conf. Ser., 288, 103  
 Ritter, H., & Kolb, U. 2003, A&A, 404, 301  
 Shakura, N. I., & Sunyaev, R. A. 1973, A&A, 24, 337  
 Smak, J. 1984a, PASP, 96, 5  
 Smak, J. 1984b, Acta Astron., 34, 317  
 Unda-Sanzana, E., Marsh, T. R., & Morales-Rueda, L. 2006, MNRAS, 369, 805  
 Warner, B. 1995, Cataclysmic Variable Stars (Cambridge University Press), Cambridge Astrophys. Ser., Cambridge, New York  
 Wood, J., Horne, K., Berriman, G., et al. 1986, MNRAS, 219, 629



# Anhang B

## A new grid of NLTE accretion-disc models for AM CVn systems: application to CE 315

T. Nagel, T. Rauch, and K. Werner

### Abstract

*Context.* AM CVn stars are very compact interacting binary systems with helium-dominated spectra. The nature of the donor star remains unclear, but the accretion disc represents the chemical composition of the donor's atmosphere. Analysing the disc will therefore help us to understand the donor star and the formation of these systems.

*Aims.* We investigate the influence of primary mass, mass-accretion rate, chemical abundances, irradiation by the primary, and inclination on the spectrum of the accretion disc to determine the extent to which it is possible to deduce these system properties by comparison with observed spectra.

*Methods.* We compute a grid of metal-line blanketed NLTE accretion-disc spectra for an extensive parameter space by solving self-consistently the radiative-transfer equations and the equations describing the vertical structure using our accretion disc code AcDc.

*Results.* We detect emission-line spectra for low and absorption-line spectra for high mass-accretion rates. Irradiation of the accretion disc by the primary has almost no influence on the spectrum. The spectroscopic detection of the primary is achievable most easily in the UV. Comparing an observed spectrum of CE 315 with our accretion-disc models, we find the qualitatively closest match for a  $0.8 M_{\odot}$  primary and a mass-accretion rate of  $10^{-11} M_{\odot}/\text{yr}$ . Furthermore, the disc of CE 315 exhibits a strong silicon underabundance confirming the hypothesis that it is a Pop. II object.

## A new grid of NLTE accretion-disc models for AM CVn systems: application to CE 315

T. Nagel, T. Rauch, and K. Werner

Institut für Astronomie und Astrophysik, Kepler Center for Astro and Particle Physics, Eberhard-Karls-Universität, Sand 1,  
 72076 Tübingen, Germany  
 e-mail: nagel@astro.uni-tuebingen.de

Received 21 December 2008 / Accepted 12 March 2009

### ABSTRACT

**Context.** AM CVn stars are very compact interacting binary systems with helium-dominated spectra. The nature of the donor star remains unclear, but the accretion disc represents the chemical composition of the donor's atmosphere. Analysing the disc will therefore help us to understand the donor star and the formation of these systems.

**Aims.** We investigate the influence of primary mass, mass-accretion rate, chemical abundances, irradiation by the primary, and inclination on the spectrum of the accretion disc to determine the extent to which it is possible to deduce these system properties by comparison with observed spectra.

**Methods.** We compute a grid of metal-line blanketed NLTE accretion-disc spectra for an extensive parameter space by solving self-consistently the radiative-transfer equations and the equations describing the vertical structure using our accretion disc code *AcDc*.

**Results.** We detect emission-line spectra for low and absorption-line spectra for high mass-accretion rates. Irradiation of the accretion disc by the primary has almost no influence on the spectrum. The spectroscopic detection of the primary is achievable most easily in the UV. Comparing an observed spectrum of CE 315 with our accretion-disc models, we find the qualitatively closest match for a  $0.8 M_{\odot}$  primary and a mass-accretion rate of  $10^{-11} M_{\odot}/\text{yr}$ . Furthermore, the disc of CE 315 exhibits a strong silicon underabundance confirming the hypothesis that it is a Pop. II object.

**Key words.** accretion, accretion disks – navae, cataclysmic variables – stars: individual: CE 315

### 1. Introduction

AM CVn stars are close, interacting binary systems with very short orbital periods below the 78 min period minimum of classical, hydrogen cataclysmic variables (CVs). Their spectra are dominated by helium lines. They are named after the prototype AM CVn (also known as HZ 29), whose binarity was proposed for the first time by Smak (1975). Presently, 21 of these systems are known (Table 1), seven of them having been discovered by the Sloan Digital Sky Survey (Anderson et al. 2005; Roelofs et al. 2005). The accretor is a white dwarf (WD), whereas the nature of the Roche-lobe-filling low-mass ( $M_2 < 0.1 M_{\odot}$ ) donor remains unclear. It might be a helium white dwarf, a helium star, or the helium-rich core of an evolved CV secondary (for more details see, e.g., Nelemans 2005). Since the matter in the accretion disc originates in the outer layers of the donor star, the analysis of the disc and the determination of its chemical composition will help us to understand the nature of the donor and the formation channel of AM CVn systems.

AM CVn systems are discussed to contribute significantly to the Type Ia supernova production rate (Nelemans et al. 2001; Solheim & Yungelson 2005). Furthermore, they are sources of low-frequency gravitational wave radiation, which will be detectable with the future Laser Interferometer Space Antenna LISA (e.g., Hils & Bender 2000).

The AM CVn stars can be divided into subgroups according to their orbital periods. The first group includes systems with ultra-short periods below 10 min. They are probably

direct-impact accretors without an accretion disc. The short-period group ( $P_{\text{orb}} < 20 \text{ min}$ ) with high mass-accretion rates of about  $10^{-8} M_{\odot}/\text{yr}$  exhibits mostly absorption-line spectra, whereas the long-period group ( $P_{\text{orb}} > 35 \text{ min}$ ) with low mass-accretion rates of about  $10^{-11} M_{\odot}/\text{yr}$  exhibits emission-line spectra. In-between are the outbursting systems, which undergo dwarf-nova cycles like hydrogen CVs but on shorter timescales because of their much smaller accretion discs. Depending on their state in the dwarf-nova cycle, they show emission- or absorption-line spectra.

There have been various attempts to model the accretion disc in AM CVn systems. Tsugawa & Osaki (1997) calculated the thermal-tidal instability cycle for helium discs. Kunze et al. (2001) studied the interaction between the infalling gas stream and the disc. Semionovas & Solheim (1999) calculated a model grid of hydrogen-helium NLTE discs and applied it to four of the AM CVn systems, El-Khoury & Wickramasinghe (2000) calculated a LTE model grid of hydrogen-helium discs in the optical range, and applied it to AM CVn and CR Boo. Nasser et al. (2001) calculated NLTE H/He-disc spectra for some AM CVn systems in the optical wavelength range, varying the mass-accretion rate only slightly ( $2-9 \times 10^{-9} M_{\odot}/\text{yr}$ ). Nagel et al. (2004) analysed the optical spectrum of AM CVn itself, using their own NLTE disc models containing H, He, C, N, O, and Si.

In this work, we calculated an extended grid of NLTE accretion-disc models, containing H, He, C, N, O, and Si, to study the influence of parameters such as primary mass, mass-accretion rate, or chemical abundances on the disc spectrum. The

**Table 1.** The known AM CVn systems.

System	$P_{\text{orb}}$ (s)	Type
RX J0806.3+1527	321.52911(2)	ultra-short, pulsed X-ray
V407 Vul	569.4	ultra-short, pulsed X-ray
ES Cet	621	high-state
AM CVn	1028.73	high-state
HP Lib	1103	high-state
CR Boo	1471	outbursting
KL Dra	1500	outbursting
V803 Cen	1596	outbursting
SDSS J0926+3642	1699	outbursting
CP Eri	1701	outbursting
2003aw (V406 Hya)	2028	outbursting
2QZ J1427-01	2194 (?)	outbursting
SDSS J1240-0159	2242	low-state
GP Com	2794	low-state
CE 315 (V396 Hya)	3906	low-state
SDSS J1411+4812	2760	emission lines
SDSS J1552+3201	3376.3(3)	emission lines
SDSS J0129+3842	—	emission lines
SDSS J1208+3550	—	emission lines
SDSS J2047+0008	—	absorption lines
SNF 20060524-042	—	—

Data taken from Bildsten et al. (2006) and references therein, Roelofs et al. (2007a,b), Anderson et al. (2005, 2008), and the website of G. Nelemans (<http://www.astro.ru.nl/~nelemans/>).

values of primary mass and mass-accretion rate were selected to include the variety of AM CVn systems. It is the first time that a such an extensive helium-dominated model grid, including the effects fo metals, has been calculated for wavelengths between the EUV and IR.

In the next section, we briefly introduce our modelling of accretion discs and their spectra. In Sect. 3, we present vertical structures and spectra of the accretion discs, varying the primary mass, mass-accretion rate, chemical abundances, and inclination angle. We also consider the effect of irradiation of the disc by the primary for different cases and the possibility of a spectroscopic detection of the primary. Finally, we compare our model spectra with an observed spectrum of CE 315 (Sect. 4). We close with a brief summary in Sect. 5.

## 2. Accretion-disc modelling

For the calculation of the metal-line blanketed NLTE accretion-disc models, we use our accretion-disc code *AcDc* (Nagel et al. 2004). It is based on the radial structure of an  $\alpha$ -disc (Shakura & Sunyaev 1973), assuming a stationary, geometrically thin disc (total disc thickness  $H$  is much smaller than the disc diameter). This allows the decoupling of the vertical and radial structures and, together with the assumption of axial symmetry, we can separate the disc into concentric annuli of plane-parallel geometry. In that way, the radiative transfer becomes a one-dimensional problem. The mass of the disc is far smaller than the mass of the central object, so we can neglect self-gravitation. The radial distribution of the effective temperature  $T_{\text{eff}}$  can be described by

$$T_{\text{eff}}(R) = \left[ \frac{3GM_1\dot{M}}{8\pi\sigma R^3} \left( 1 - \sqrt{\frac{R_1}{R}} \right) \right]^{1/4}, \quad (1)$$

where  $M_1$  and  $R_1$  denote the mass and the radius of the central object,  $\dot{M}$  is the mass-accretion rate,  $G$  the gravitational constant,

and  $\sigma$  the Stefan-Boltzmann constant. The radial profile of surface mass density  $\Sigma$  can be described by

$$w\Sigma(R) = \frac{\dot{M}}{3\pi} \left( 1 - \left( \frac{R_1}{R} \right)^{1/2} \right) \quad (2)$$

for the kinematic viscosity  $w$ .

For each disc ring, the following set of coupled equations were solved simultaneously under the constraints of particle number and charge conservation:

- radiation transfer for the specific intensity  $I$

$$\mu \frac{\partial I(\nu, \mu, z)}{\partial z} = -\chi(\nu, z) I(\nu, \mu, z) + \eta(\nu, z) \quad (3)$$

with the absorption coefficient  $\chi$ , the emission coefficient  $\eta$ , the geometrical disc height  $z$  above the midplane, and  $\mu = \cos\theta$  with  $\theta$  being the angle between the ray and  $z$ . To consider irradiation of the accretion disc by the primary, the irradiation angle and the spectrum of the primary (blackbody or detailed model-atmosphere spectrum) must be specified. Since we employ a five-point Gaussian quadrature for angle integration, the stellar disc is usually unresolved (except for annuli very close to the star) and the irradiated flux is assigned to a single quadrature point. Stellar limb darkening is neglected;

- hydrostatic equilibrium between gravitation, gas pressure  $P_{\text{gas}}$ , and radiation pressure

$$\frac{dP_{\text{gas}}}{dm} = \frac{GM_1}{R^3} z - \frac{4\pi}{c} \int_0^\infty \frac{\chi(\nu)}{\rho} H(\nu, z) d\nu, \quad (4)$$

with  $\rho$  denoting the mass density, and  $H$  the Eddington flux. Here we also introduced the column mass depth  $m$  as

$$m(z) = \int_z^\infty \rho(z') dz'; \quad (5)$$

- energy balance between the viscously generated energy  $E_{\text{mech}}$  and the radiative energy loss  $E_{\text{rad}}$

$$E_{\text{mech}} = E_{\text{rad}} (+ E_{\text{conv}}) \quad (6)$$

with

$$E_{\text{mech}} = w\Sigma \left( R \frac{d\omega}{dR} \right)^2 = \frac{9}{4} w\Sigma \frac{GM_1}{R^3} \quad (7)$$

and

$$E_{\text{rad}} = 4\pi \int_0^\infty (\eta(\nu, z) - \chi(\nu, z) J(\nu, z)) d\nu \quad (8)$$

with the angular velocity  $\omega$ , and the mean intensity  $J$ . Convection ( $E_{\text{conv}}$ ) is neglected in our models;

- NLTE rate equations for the population numbers  $n_i$  of the atomic levels  $i$

$$\frac{\partial n_i}{\partial t} = n_i \sum_{i \neq j} P_{ij} - \sum_{j \neq i} n_j P_{ji}. \quad (9)$$

$P_{ij}$  denotes the rate coefficients, consisting of radiative and collisional components. For the static case, it follows that

$$\frac{\partial n_i}{\partial t} = 0. \quad (10)$$

**Table 2.** Statistics of the model atoms used in our disc models.

Ion	LTE levels	NLTE levels	Lines
H I	6	10	45
H II	—	1	—
He I	15	29	61
He II	24	8	28
He III	—	1	—
C I	14	7	4
C II	4	38	160
C III	9	58	329
C IV	49	9	17
C V	0	1	0
N I	15	12	15
N II	4	17	21
N III	38	7	5
N IV	78	16	30
N V	8	54	297
N VI	0	1	0
O I	12	1	0
O II	14	29	82
O III	8	36	42
O IV	58	11	5
O V	15	6	4
O VI	0	1	0
Si II	5	25	28
Si III	17	17	27
Si IV	11	28	49
Si V	44	15	20
Si VI	0	1	0

By integrating the spectra of the individual annuli, one obtains a complete disc spectrum for different inclination angles, where the spectral lines are Doppler shifted according to the radial component of the Kepler rotational velocity. For a more detailed description of the accretion-disc modelling with *AcDc*, we refer the reader to Nagel et al. (2004).

The input parameters we have to provide for the calculation of disc rings are the mass  $M_1$  and radius  $R_1$  of the primary, the mass-accretion rate  $\dot{M}$ , the Reynolds number  $Re$ , the radius of the annulus  $R$ , the chemical abundances, the irradiation angle  $\beta$ , and the spectrum or the black-body temperature  $T_{\text{irr}}$  of the primary. Detailed information about the involved atomic data is provided in the form of a model atom (cf. Rauch & Deetjen 2003).

Since the accretion discs of AM CVn stars are fed by a helium-rich secondary, we assume a disc composition dominated by helium. Hydrogen, carbon, nitrogen, oxygen, and silicon are considered with varying abundances (Table 4). Iron-group elements and molecule formation are not considered. Details about our model atoms are shown in Table 2, the silicon lines in the optical and UV are split into multiplets (assuming relative LTE populations for the sublevels).

The model grid presented here comprises more than 70 accretion discs with about 10 single disc-ring models each. For each disc, the spectrum for five inclination angles is calculated.

### 3. The model grid

We calculated a grid of accretion-disc models to cover the entire parameter range of AM CVn systems. We assumed five different primaries from  $0.6$  to  $1.4 M_\odot$ , for each four different mass-accretion rates from  $10^{-8}$  to  $10^{-11} M_\odot/\text{yr}$  (see Table 3). Every disc spectrum is calculated for at least three different chemical

**Table 3.** Parameters of the model grid.  $M_1$ ,  $R_1$  and  $g$  are the mass, the radius and the surface gravity of the white dwarf primary, respectively,  $\dot{M}$  the mass-accretion rate,  $\log g$  is calculated from  $M_1$  and  $R_1$ .

#	$M_1 [M_\odot]$	$R_1 [\text{km}]$	$\log g$	$\log \dot{M} [M_\odot/\text{yr}]$
1	0.6	9550	7.9	-8, -9, -10, -11
2	0.8	7380	8.3	-8, -9, -10, -11
3	1.0	5830	8.6	-8, -9, -10, -11
4	1.2	4100	9.0	-8, -9, -10, -11
5	1.4	3160	9.3	-8, -9, -10, -11

**Table 4.** Variation in the abundances for the included elements with  $[x] = \log(\text{mass fraction}/\text{solar mass fraction})$  of species  $x$ , following Grevesse & Sauval (2000) for the solar abundances.

#	[C]	[N]	[O]	[Si]	[H]
1	0	0	0	0	-10
2	-3	1	-3	0	-10
3	-3	1	-3	-3	-10
4	0	0	0	0	-6, -5, -3, -2

compositions. Unless otherwise noted, all plots shown are of composition #2 (Table 4).

The maximum outer radius of the discs is defined by the tidal radius, where the disc is truncated by the tidal forces of the secondary. It can approximately be written (Warner 1995) as

$$r_{\text{tidal}} = 0.60 \cdot \frac{a}{1+q} \quad \text{with} \quad 0.03 < q < 1 \quad (11)$$

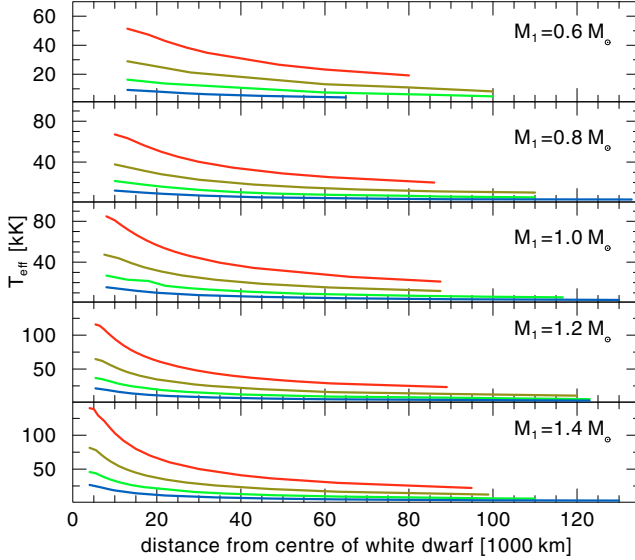
with the binary's separation  $a$  and the mass ratio  $q = M_2/M_1$ . The separation can be derived from Kepler's law. For the highest mass-accretion rate systems, we assumed an orbital period of 1000 s, for the lowest mass-accretion rate systems 3000 s and for the systems in between 1500 s. For the companion, we assumed a mass of  $0.05 M_\odot$  for all systems. In the case of the lowest mass-accretion rate, we encountered numerical problems for the outermost disc rings. As a result, the respective disc models were not extended to the tidal radius. Depending on the primary mass and mass-accretion rate, this produced outer disc radii between 8 and  $20 R_1$ .

Figure 1 shows the radial variation in the effective temperature as well as the radial extension for the five primary masses and all mass-accretion rates. Here and in the following, the effective temperatures of the disc are always intrinsic, regardless of whether irradiation is considered or not. Our hottest model has effective temperatures of between 120 000 K and 22 000 K, whereas the coolest disc only varies between 9000 K and 4000 K. As an example, Fig. 2 shows the vertical ionisation structure of an inner disc ring for low and high mass-accretion rates.

#### 3.1. Variation of the primary mass

With increasing primary mass and constant mass-accretion rate, the accretion disc becomes hotter, due to the stronger gravitational field of the more compact primary (Fig. 1). In Fig. 3, the vertical structures of a ring in the inner part ( $1.9 R_1$ ) of the disc are shown for all five primary masses at low mass-accretion rate. In the case of low-mass primaries, the temperature structure becomes nearly isothermal and the disc is optically thin.

Figure 4 shows the optical and UV spectra of the accretion discs for the five primary masses and mass-accretion rates of



**Fig. 1.** Radial run of disc effective temperature for five primary masses and four mass-accretion rates (in each panel  $\dot{M} = 10^{-8}$ – $10^{-11} M_{\odot}/\text{yr}$  from top).

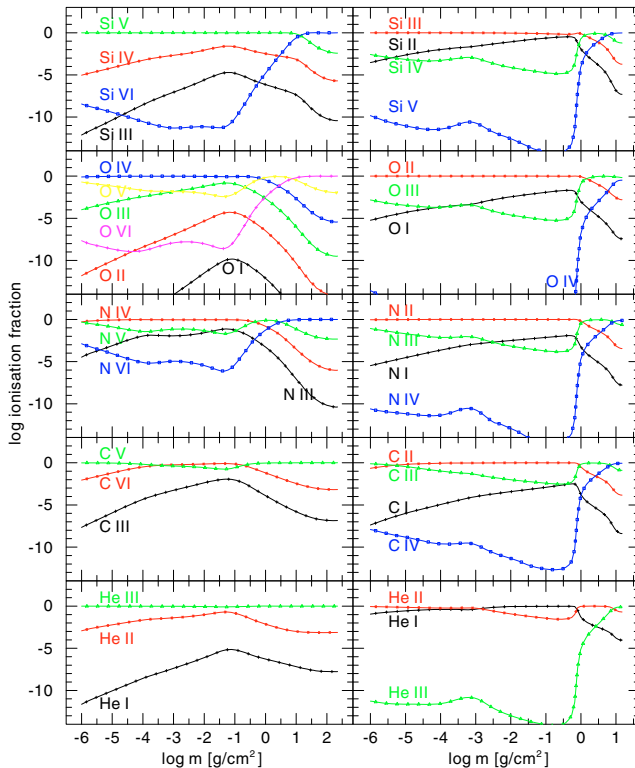


**Fig. 2.** Vertical run of ionisation fractions for a primary with  $0.6 M_{\odot}$  and mass-accretion rates of  $10^{-8} M_{\odot}/\text{yr}$  (left panels) and  $10^{-10} M_{\odot}/\text{yr}$  (right) versus the column mass density (increasing from outer to inner layers) for an inner disc ring ( $1.4 R_1$ ).

$10^{-8} M_{\odot}/\text{yr}$  and  $10^{-11} M_{\odot}/\text{yr}$ , all shown for the same inclination angle ( $18^{\circ}$ ). As expected from observations, the low mass-accretion rate models show strong emission-line spectra and the high mass-accretion rate models absorption-line spectra. In the case of low mass-accretion rates, the total flux in the optical and

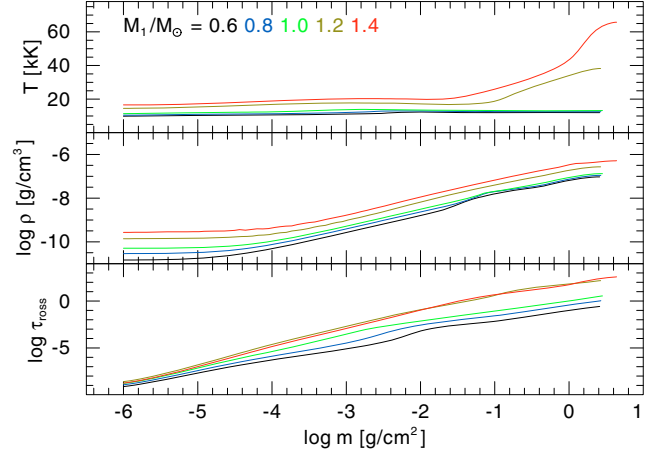


**Fig. 3.** Vertical structure of an inner disc ring at a radius of  $1.9 R_1$  for different primary masses at a mass-accretion rate of  $10^{-11} M_{\odot}/\text{yr}$ . Shown are the temperature  $T$  (top panel), the density  $\rho$  (middle) and the Rosseland optical depth  $\tau_{\text{ross}}$  (bottom).

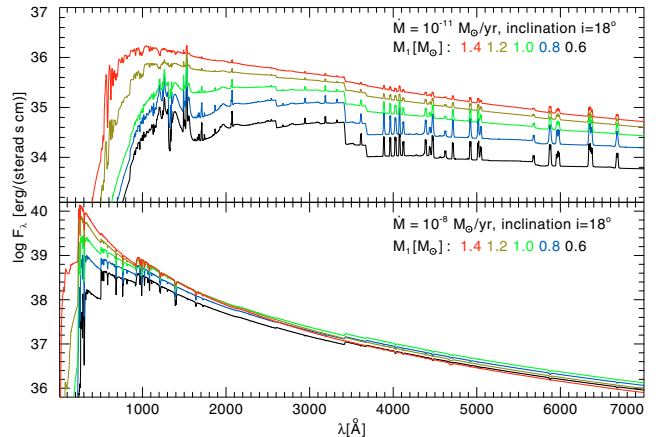


**Fig. 4.** Accretion-disc spectra for a mass-accretion rate of  $10^{-8}$  (bottom panel) and  $10^{-11} M_{\odot}/\text{yr}$  (top panel) and different primary masses.

UV increases with increasing primary mass due to the higher disc temperature. In the case of high mass-accretion, the disc model with the most massive primary dominates the UV, but in the optical spectral range the disc fluxes with the lower-mass primaries are higher.

In Fig. 5, the spectra of single rings of a disc with a  $0.6 M_{\odot}$  primary and a mass-accretion rate of  $10^{-10} M_{\odot}/\text{yr}$  are shown. Due to the different effective temperatures in the inner and outer parts of the disc, the spectra differ significantly and show absorption lines in the inner and emission lines in the outer disc region.

### 3.2. Variation of the mass-accretion rate

An increase in the mass-accretion rate at the same primary mass leads to a higher disc temperature, which can be seen in Fig. 6, where the vertical structures of an inner disc ring ( $1.9 R_1$ ) are shown for a low-mass primary at four different mass-accretion rates. The surface density increases with increasing accretion rate, as can be seen from the  $\log m$  value at the inner depth point.

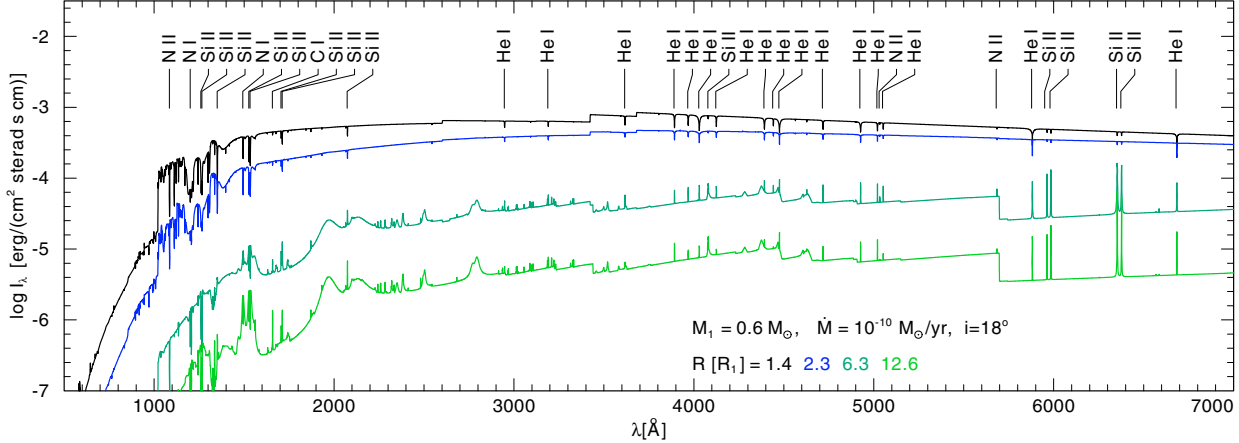


**Fig. 5.** Disc ring spectra from the inner (top graph,  $1.4 R_1$ ) to the outer (bottom graph,  $12.6 R_1$ ) part of the accretion disc for an  $0.6 M_\odot$  primary and a mass-accretion rate of  $10^{-10} M_\odot/\text{yr}$  without rotational broadening.

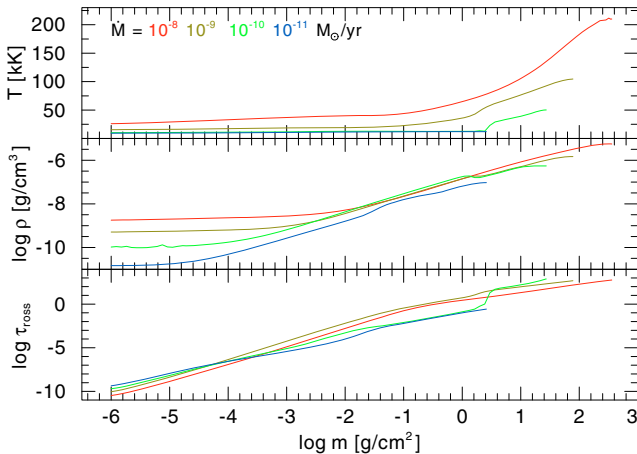


**Fig. 6.** Vertical structure of an inner disc ring ( $1.9 R_1$ ) for different mass-accretion rates with a WD primary of  $0.6 M_\odot$ .

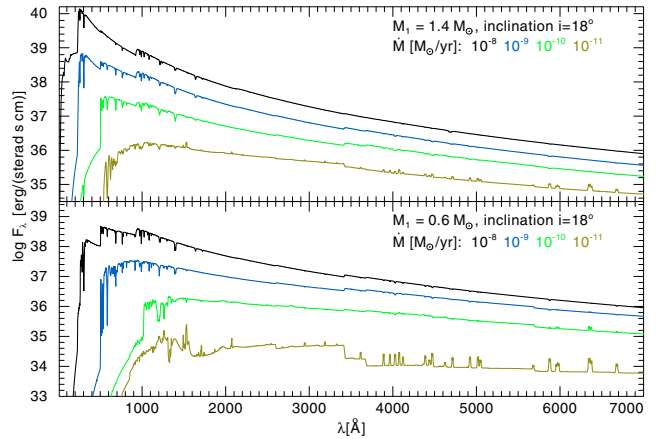


**Fig. 7.** Accretion-disc spectra for a primary with  $0.6$  (bottom panel) and  $1.4 M_\odot$  (top) and different mass-accretion rates.

Figure 7 (lower panel) shows the change from an absorption-line spectrum to an emission-line spectrum with decreasing mass-accretion rate for a low-mass primary of  $0.6 M_\odot$ . Furthermore, the continuum flux level is reduced by almost a factor of 1000 due to the decrease in temperature. In the case of the most massive primary with  $1.4 M_\odot$ , we found a weak emission-line spectrum only for our lowest mass-accretion rate (Fig. 7, upper panel).

### 3.3. Variation in chemical abundances

The variation in the chemical abundances for a low-mass and a high-mass primary is shown in Figs. 8 and 9. We compare models with chemical compositions as listed in Table 4.

In the case of the low-mass primary, there are strong Si lines in the optical, which disappear only for strong Si underabundance. In the case of the high-mass primary, it is difficult to see any differences in the optical disc spectra, but in the UV the disappearance of carbon and silicon lines with corresponding underabundance can be clearly seen. By comparing our model spectra with observations, it should be possible to reveal a metal

underabundance in the accretion discs of AM CVn systems, as already proposed for GP Com (Marsh et al. 1991; Morales-Rueda et al. 2003). The determination of hydrogen in the accretion disc is especially interesting in the case of the white-dwarf formation channel of AM CVn stars, where it is possible that a small amount of hydrogen remains (Podsiadlowski et al. 2003). We increased the abundance of hydrogen in a high and low mass-accretion rate disc for two primaries ( $0.6$  and  $1.2 M_\odot$ ) to deduce the upper limits at which hydrogen becomes visible in the spectrum. We found that in low-state systems a H abundance of  $10^{-6}$  already leads to strong Balmer emission lines (Fig. 9, right panel), whereas in the UV no hydrogen lines are detectable. In high-state systems, only an abundance of  $10^{-3}$  produces significant Balmer lines (Fig. 9, left panel). In the UV, even an abundance of  $10^{-2}$  is needed to see significant hydrogen lines.

### 3.4. Variation of inclination

All models so far have been shown for an inclination angle of  $18^\circ$ . The variation in the inclination also leads to strong

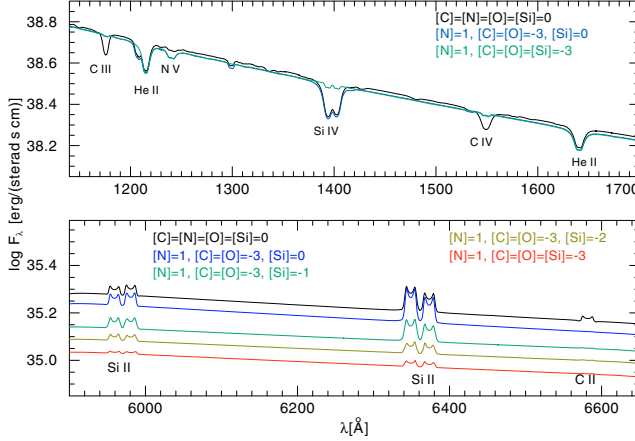


**Fig. 8.** Accretion-disc spectra for a primary with  $1.2 M_\odot$  and a mass-accretion rate of  $10^{-8} M_\odot/\text{yr}$  (upper panel) and a primary with  $0.6 M_\odot$  and a mass-accretion rate of  $10^{-10} M_\odot/\text{yr}$  (lower) for different chemical abundances.

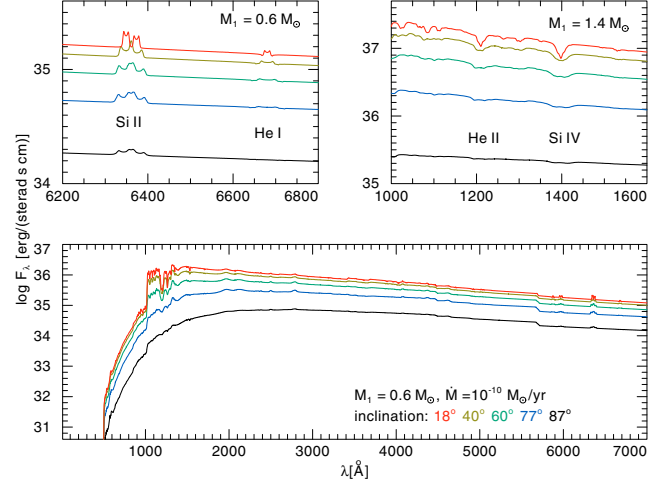


**Fig. 10.** Accretion-disc spectra for a primary with  $0.6 M_\odot$  (bottom panel) and  $1.4 M_\odot$  (top right panel) and a mass-accretion rate of  $10^{-10} M_\odot/\text{yr}$  for different inclination angles.

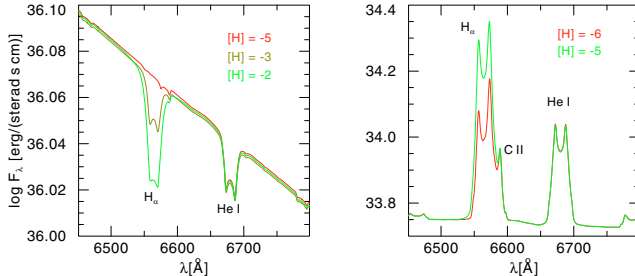


**Fig. 9.** Accretion-disc spectra for different hydrogen abundances. Left panel:  $M_1 = 0.6 M_\odot$ ,  $\dot{M} = 10^{-8} M_\odot/\text{yr}$ , right:  $M_1 = 0.6 M_\odot$ ,  $\dot{M} = 10^{-11} M_\odot/\text{yr}$ .

differences in the spectra, which is shown in Fig. 10 for two primary masses. The spectral lines become broader with increasing inclination due to the increasing radial component of the Kepler rotation velocity. At the same time, the total flux decreases because of the smaller visible projected surface area of the disc and limb-darkening effects.

### 3.5. Irradiation by the primary

The geometry of AM CVn systems is quite extreme, as can be seen from Fig. 11, where a sketch of a primary with  $0.6 M_\odot$  and the accretion disc is shown. This leads to rather large irradiation angles of more than  $20^\circ$  for the inner part and about  $5^\circ$  for the outer part of the accretion disc. We accounted for irradiation of the disc by the primary for two primary masses at high and low mass-accretion rate to investigate the influence on the vertical structure and disc spectrum. The irradiation was performed with a 20 000 K black-body spectrum for the low and 50 000 K, 80 000 K, and 100 000 K for the high mass-accretion rate system. These effective temperatures for the primary are reasonable, following Bildsten et al. (2006), who calculated the heating and cooling of the accreting white dwarf in AM CVn systems. Using white-dwarf model spectra instead of black-body spectra

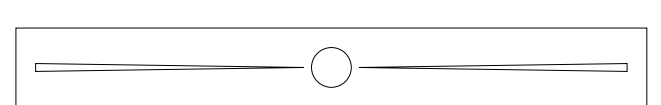


**Fig. 11.** Sketch of a cut through an AM CVn system (primary with  $0.6 M_\odot$ ,  $\dot{M} = 10^{-11} M_\odot/\text{yr}$ , adequate proportions).

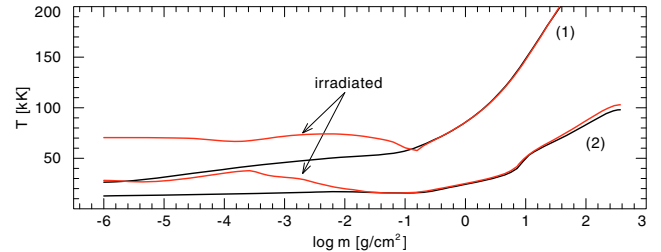


**Fig. 12.** Temperature structure in the inner (1,  $1.3 R_1$ ) and outer part (2,  $12 R_1$ ) of the disc, irradiated by a white dwarf with  $T_{\text{eff}} = 80 000 \text{ K}$  and non-irradiated, primary with  $0.8 M_\odot$  and mass-accretion rate of  $10^{-8} M_\odot/\text{yr}$ .

for the irradiation does not show any difference in the resulting accretion-disc spectrum.

Figure 12 compares, as an example, the vertical temperature structures of irradiated and non-irradiated disc rings for high mass-accretion rate ( $10^{-8} M_\odot/\text{yr}$ ) in the case of a  $0.8 M_\odot$  primary. The upper layers of the disc rings are heated up by the irradiation, but the spectra do not significantly differ (not shown). At low mass-accretion rate and with irradiation from a 20 000 K primary, the UV spectrum changes slightly, while the optical spectrum is unaffected (see Fig. 13).

### 3.6. Disc and primary

Since AM CVn systems are very compact binaries, it is impossible to resolve their components. The spectra we obtain

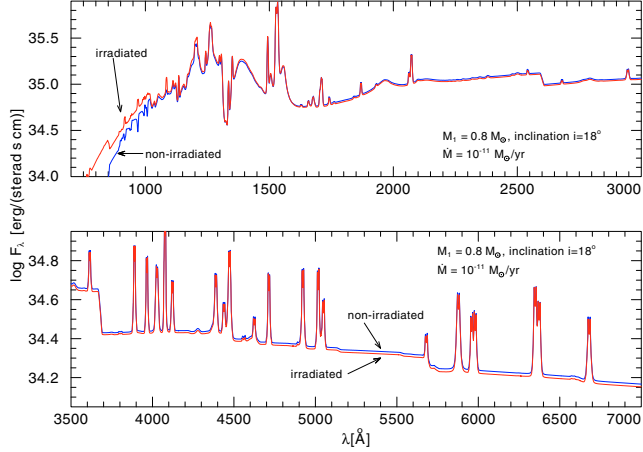


**Fig. 13.** Comparison of an irradiated ( $T_{\text{eff,WD}} = 20\,000$  K) and a non-irradiated accretion-disc spectrum for low mass-accretion rate ( $10^{-11} M_\odot/\text{yr}$ ), primary with  $0.8 M_\odot$ .

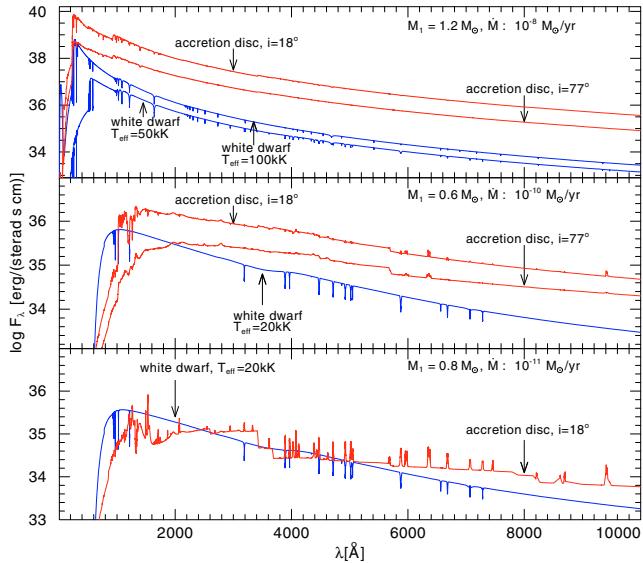


**Fig. 14.** Comparison of spectra of accretion disc and white dwarf. Top panel:  $1.2 M_\odot$  primary with  $T_{\text{eff}} = 50\,000$  K and  $T_{\text{eff}} = 100\,000$  K and  $\dot{M} = 10^{-8} M_\odot/\text{yr}$ , accretion disc extended between  $1.3$  and  $20 R_1$ . Middle panel:  $0.6 M_\odot$  primary with  $T_{\text{eff}} = 20\,000$  K and  $\dot{M} = 10^{-10} M_\odot/\text{yr}$ , accretion disc extended between  $1.3$  and  $12.5 R_1$ . Bottom panel:  $0.8 M_\odot$  primary with  $T_{\text{eff}} = 20\,000$  K and  $\dot{M} = 10^{-11} M_\odot/\text{yr}$ , accretion disc extended between  $1.3$  and  $18 R_1$ .

correspond to the light of the white dwarf, the accretion disc, and the donor star. Only for one of the AM CVn systems the primary seems to have been spectroscopically detected (Sion et al. 2006). To investigate the amount to which the white dwarf contributes to the total spectrum, we calculated synthetic helium-dominated ( $H/He = 10^{-5}$ ) spectra using our stellar atmosphere code TMAP. We then weighted the spectra with the WD surface area, ignoring partial occlusion by the accretion disc, and compared them with the accretion-disc spectra (Fig. 14). For high mass-accretion rates ( $\dot{M} = 10^{-8} M_\odot/\text{yr}$ ), we assumed a hot WD of 50 000 K and 100 000 K. We found that the flux

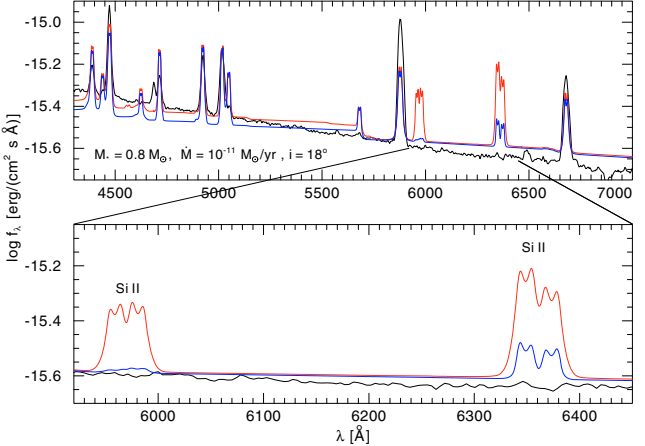


**Fig. 15.** Comparison of the spectrum of CE 315 (Ruiz et al. 2001, thick line) with a model spectrum with solar and 0.001 times solar silicon abundance (lower panel, zoom). The mass of the primary is  $0.8 M_\odot$ , the mass-accretion rate is  $10^{-11} M_\odot/\text{yr}$ , the inclination is  $18^\circ$ . The He I lines in the observed spectrum are dominated by a component probably not created in the disc itself but at the hotspot or the inner boundary layer (as discussed by Ruiz et al. 2001).

of even the coolest disc is higher than the flux of the related white dwarf ( $T_{\text{eff}} = 50\,000$  K). At low mass-accretion rate ( $\dot{M} = 10^{-10} M_\odot/\text{yr}$ ), assuming a WD of 20 000 K, there is a chance of detecting the primary in the UV, especially if the disc is at high inclination. In the optical and infrared range, the disc flux is much higher than that of the white dwarf, even if we reduce the disc size drastically ( $3-7 R_1$  instead of  $1.3-12.5 R_1$ ). The optimal opportunity of detecting the WD spectroscopically is in systems with the lowest mass-accretion rate ( $\dot{M} = 10^{-11} M_\odot/\text{yr}$ , again assuming  $T_{\text{eff}} = 20\,000$  K).

#### 4. Model versus observation in the case of CE 315

CE 315 is the AM CVn system with the longest known orbital period (65.1 min). The optical spectrum shows emission lines of He I and He II, and a few weak N I and N II lines. The accretor mass is about  $0.77 M_\odot$  (Ruiz et al. 2001). The profile of the spectral lines is variable on a timescale of a few minutes, probably due to the rotating hotspot, the collisional region between accretion stream and accretion disc. The helium lines often show three peaks. Ruiz et al. (2001) suggested that the outer components originate in the accretion disc, whereas the central peak is produced by the boundary layer. In the case of He II  $\lambda 4686 \text{ Å}$  the central component dominates the line completely. This central peak feature is also seen in GP Com (Smak 1975; Morales-Rueda et al. 2003) and is much weaker in SDSS J124058.03-015919.2 (Roelofs et al. 2005). Because of the absence of silicon lines in the UV (Gänsicke et al. 2003) and optical spectra, CE 315 is thought to be a Population II object (Roelofs et al. 2005; Ramsay et al. 2006). A strong silicon underabundance ( $10^{-3}$  times solar) has also been found for GP Com (Marsh et al. 1991). From the analysis of the X-ray spectrum of CE 315, Ramsay et al. (2006) found a significant enhancement of nitrogen (68–92% more than the solar value).

In Fig. 15, we compare an observed spectrum of CE 315 (Ruiz et al. 2001) with two model spectra with solar and

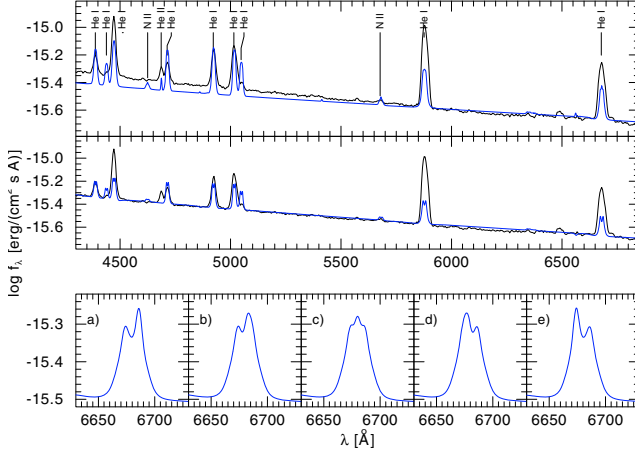


**Fig. 16.** Top panel: comparison of the spectrum of CE 315 (Ruiz et al. 2001, thick line) with a model with 0.0001 times solar silicon abundance, a boundary layer and a hotspot region. Middle: accretion disc without boundary layer and hotspot, combined with the model spectrum of a white dwarf ( $T_{\text{eff}} = 20\,000\,\text{K}$ ,  $\log g = 8.3$ ), compared with the observed spectrum. Lower panel: modulation of the He I  $\lambda 6678\,\text{\AA}$  spectral line caused by the orbiting hotspot. The position of the hotspot varies from a) moving away from observer to e) moving towards observer. Inclination of all models is  $18^\circ$ .

0.001 times solar silicon abundance. We assumed  $M_1 = 0.8\,M_\odot$  and  $\dot{M} = 10^{-11}\,M_\odot/\text{yr}$ . It is clearly indicative of a strong silicon underabundance (<0.001 times solar) in the accretion disc of CE 315.

Since the model spectra are too flat, we added a hotter disc ring to the innermost part ( $1.1\text{--}1.4R_1$ ) of the disc to approximate a type of a boundary layer. Using a ring of  $\dot{M} = 10^{-9}\,M_\odot/\text{yr}$ , the flux in the UV becomes too high, in contrast to the observation showing almost no continuum in UV (Gänsicke et al. 2003). With a mass-accretion rate of  $10^{-10}\,M_\odot/\text{yr}$ , the flux in the UV is comparable to that of observations but in the optical still remains too flat. In addition to this boundary layer, we added to the outermost part of the disc a hot area approximating a hot-spot region in the following way. We took the structure of the outermost disc ring and heated the upper layers artificially from about 10 000 K to 35 000 K. The result was an almost identical emission-line spectrum in the optical but of a higher flux level. In the final integration of all disc rings, this region was extended 20 degrees in azimuth and between 12 and  $13.5R_1$  in radial direction, representing the hot-spot region. Finally, we reduced the silicon abundance to 0.0001 times solar and set the nitrogen abundance to 2 times solar. The resulting model spectrum is shown in the upper panel of Fig. 16. In general, the observed spectrum is reproduced well, but some of the helium lines are too weak, and others are too strong.

We also determined the possible contribution of the white dwarf to the observed spectrum. In the middle panel of Fig. 16, the combined model spectrum of the pure disc (no boundary region or hotspot) and a white dwarf ( $T_{\text{eff}} = 20\,000\,\text{K}$ ,  $\log g = 8.3$ ) is compared with observations. The observed spectrum is reproduced qualitatively well indicating that the WD's contribution should not be neglected. Because of the missing hotspot, the spectral lines are double peaked.

The lower panel of Fig. 16 shows in detail He I  $\lambda 6678\,\text{\AA}$ . The influence of the orbiting hotspot on the line profile is obvious.

## 5. Summary

We have presented our grid of NLTE accretion-disc models for AM CVn systems. In the framework of the Virtual Observatory<sup>1</sup> (VO), all spectral energy distributions (SEDs,  $\lambda - F_\lambda$ ) described here will be available in VO compliant form from the VO service *TheoSSA*<sup>2</sup> provided by the German Astrophysical Virtual Observatory (GAVO)<sup>3</sup>. We used primary masses between  $0.6\,M_\odot$  and  $1.4\,M_\odot$  and mass-accretion rates between  $10^{-11}$  and  $10^{-8}\,M_\odot/\text{yr}$  and varied the chemical composition. Our main results are as follows:

1. Discs with high mass-accretion rate ( $10^{-8}\,M_\odot/\text{yr}$ ) show absorption-line spectra, and discs with low mass-accretion rate ( $10^{-10}\text{--}10^{-11}\,M_\odot/\text{yr}$ ) emission-line spectra, as expected from observations.
2. Underabundances of C, O, and Si should be detectable by comparisons with observed spectra. A hydrogen abundance of  $10^{-5}$  (mass fraction) leads to strong Balmer emission lines in low-state systems. In high-state systems, an abundance of  $10^{-3}$  is necessary to obtain detectable Balmer lines. In both cases, it is nearly impossible to detect hydrogen lines in the UV.
3. Irradiation of the accretion disc by the primary ( $T_{\text{eff}} = 20\,000\,\text{K}$  for low-state and outbursting systems,  $T_{\text{eff}} = 50\,000\,\text{K}$  up to  $T_{\text{eff}} = 100\,000\,\text{K}$  for high-state systems) heats up the upper layers of the disc but has almost no effect on the spectrum.
4. Comparing the spectra of the primary white dwarf and the accretion disc shows that the primary, if at all, can be seen only in UV. The optical spectral range is dominated by the disc for  $\dot{M}$  between  $10^{-8}$  and  $10^{-10}\,M_\odot/\text{yr}$ . Only for the lowest rate of  $10^{-11}\,M_\odot/\text{yr}$  is the continuum flux of the white dwarf in the optical higher than the disc flux.
5. The accretion-disc spectrum of CE 315 is reproduced well by assuming a  $0.8\,M_\odot$  primary, a mass-accretion rate of  $10^{-11}\,M_\odot/\text{yr}$ , and a white dwarf with  $T_{\text{eff}} = 20\,000\,\text{K}$ , and  $\log g = 8.3$ .
6. An orbiting hotspot in the outer part of the disc produces a modulation in the helium-line profiles.
7. We have confirmed a strong silicon underabundance in the accretion disc of CE 315 and, hence, that this system might be a Population II object.

**Acknowledgements.** We thank M. T. Ruiz for providing us with the observed spectrum of CE 315. T.R. is supported by the German Astrophysical Virtual Observatory (GAVO) project of the German Federal Ministry of Education and Research (BMBF) under grant 05 AC6VTB.

## References

- Anderson, S. F., Haggard, D., Homer, L., et al. 2005, AJ, 130, 2230  
 Anderson, S. F., Becker, A. C., Haggard, D., et al. 2008, AJ, 135, 2108  
 Bildsten, L., Townsley, D. M., Deloye, C. J., & Nelemans, G. 2006, ApJ, 640, 466  
 El-Khoury, W., & Wickramasinghe, D. 2000, A&A, 358, 154  
 Gänsicke, B. T., Szkody, P., de Martino, D., et al. 2003, ApJ, 594, 443  
 Grevesse, N., & Sauval, A. 2000, Solar Abundances, ed. P. Murdin, Encyclopedia of Astronomy and Astrophysics  
 Hils, D., & Bender, P. L. 2000, ApJ, 537, 334  
 Kunze, S., Speith, R., & Hessman, F. V. 2001, MNRAS, 322, 499  
 Marsh, T. R., Horne, K., & Rosen, S. 1991, ApJ, 366, 535

<sup>1</sup> <http://www.ivoa.net>

<sup>2</sup> <http://vo.ari.uni-heidelberg.de/ssatr-0.01/TrSpectra.jsp>

<sup>3</sup> <http://www.g-vo.org>

- Morales-Rueda, L., Marsh, T. R., Steeghs, D., et al. 2003, *A&A*, 405, 249  
 Nagel, T., Dreizler, S., Rauch, T., & Werner, K. 2004, *A&A*, 428, 109  
 Nasser, M. R., Solheim, J.-E., & Semionoff, D. A. 2001, *A&A*, 373, 222  
 Nelemans, G. 2005, in *The Astrophysics of Cataclysmic Variables and Related Objects*, ed. J.-M. Hameury, & J.-P. Lasota, ASP Conf. Ser., 330, 27  
 Nelemans, G., Portegies Zwart, S. F., Verbunt, F., & Yungelson, L. R. 2001, *A&A*, 368, 939  
 Podsiadlowski, P., Han, Z., & Rappaport, S. 2003, *MNRAS*, 340, 1214  
 Ramsay, G., Groot, P. J., Marsh, T., et al. 2006, *A&A*, 457, 623  
 Rauch, T., & Deetjen, J. L. 2003, in *Stellar Atmosphere Modeling*, ed. I. Hubeny, D. Mihalas, & K. Werner, ASP Conf. Ser., 288, 103  
 Roelofs, G. H. A., Groot, P. J., Marsh, T. R., et al. 2005, *MNRAS*, 361, 487  
 Roelofs, G. H. A., Groot, P. J., Nelemans, G., Marsh, T. R., & Steeghs, D. 2007a, *MNRAS*, 379, 176  
 Roelofs, G. H. A., Groot, P. J., Steeghs, D., Marsh, T. R., & Nelemans, G. 2007b, *MNRAS*, 382, 1643  
 Ruiz, M. T., Rojo, P. M., Garay, G., & Maza, J. 2001, *ApJ*, 552, 679  
 Semionovas, D., & Solheim, J.-E. 1999, in *11th European Workshop on White Dwarfs*, ed. J.-E. Solheim, & E. G. Meistas, ASP Conf. Ser., 169, 356  
 Shakura, N. I., & Sunyaev, R. A. 1973, *A&A*, 24, 337  
 Sion, E. M., Solheim, J.-E., Szkody, P., Gaensicke, B. T., & Howell, S. B. 2006, *ApJ*, 636, L125  
 Smak, J. 1975, *Acta Astron.*, 25, 371  
 Solheim, J.-E., & Yungelson, L. R. 2005, in *14th European Workshop on White Dwarfs*, ed. D. Koester, & S. Moehler, ASP Conf. Ser., 334, 387  
 Tsugawa, M., & Osaki, Y. 1997, *PASJ*, 49, 75  
 Warner, B. 1995, *Cataclysmic variable stars*, Cambridge Astrophysics Series (Cambridge, New York: Cambridge University Press)

Anhang C

VLT spectroscopy and non-LTE modeling of the  
C/O-dominated accretion disks in two ultracompact X-ray  
binaries

K. Werner, T. Nagel, T. Rauch, N. J. Hammer, and S. Dreizler

**Abstract**

*Aims.* We present new medium-resolution high-S/N optical spectra of the ultracompact low-mass X-ray binaries 4U 0614+091 and 4U 1626-67, taken with the ESO Very Large Telescope. They are pure emission line spectra and the lines are identified as due to C II-IV and O II-III.

*Methods.* Line identification is corroborated by first results from modeling the disk spectra with detailed non-LTE radiation transfer calculations. Hydrogen and helium lines are lacking in the observed spectra.

*Results.* Our models confirm the deficiency of H and He in the disks. The lack of neon lines suggests an Ne abundance of less than about 10 percent (by mass), however, this result is uncertain due to possible shortcomings in the model atom. These findings suggest that the donor stars are eroded cores of C/O white dwarfs with no excessive neon overabundance. This would contradict earlier claims of Ne enrichment concluded from X-ray observations of circumbinary material, which was explained by crystallization and fractionation of the white dwarf core.

## VLT spectroscopy and non-LTE modeling of the C/O-dominated accretion disks in two ultracompact X-ray binaries\*

K. Werner<sup>1</sup>, T. Nagel<sup>1</sup>, T. Rauch<sup>1</sup>, N. J. Hammer<sup>2,1</sup>, and S. Dreizler<sup>3</sup>

<sup>1</sup> Institut für Astronomie und Astrophysik, Universität Tübingen, Sand 1, 72076 Tübingen, Germany  
 e-mail: werner@astro.uni-tuebingen.de

<sup>2</sup> Max-Planck-Institut für Astrophysik, Karl-Schwarzschild-Straße 1, 85741 Garching, Germany

<sup>3</sup> Institut für Astrophysik, Universität Göttingen, Friedrich-Hund-Platz 1, 37077 Göttingen, Germany

Received 5 July 2005 / Accepted 2 January 2006

### ABSTRACT

**Aims.** We present new medium-resolution high-S/N optical spectra of the ultracompact low-mass X-ray binaries 4U 0614+091 and 4U 1626-67, taken with the ESO Very Large Telescope. They are pure emission line spectra and the lines are identified as due to C II-IV and O II-III.

**Methods.** Line identification is corroborated by first results from modeling the disk spectra with detailed non-LTE radiation transfer calculations. Hydrogen and helium lines are lacking in the observed spectra.

**Results.** Our models confirm the deficiency of H and He in the disks. The lack of neon lines suggests an Ne abundance of less than about 10 percent (by mass), however, this result is uncertain due to possible shortcomings in the model atom. These findings suggest that the donor stars are eroded cores of C/O white dwarfs with no excessive neon overabundance. This would contradict earlier claims of Ne enrichment concluded from X-ray observations of circumbinary material, which was explained by crystallization and fractionation of the white dwarf core.

**Key words.** accretion, accretion disks – binaries: close – X-rays: binaries – stars: individual: 4U 0614+091 – stars: individual: 4U 1626-67

### 1. Introduction

Low-mass X-ray binaries (LMXBs) consist of a neutron star or black-hole accretor and a low-mass donor star ( $M \lesssim 1 M_{\odot}$ ). Of particular interest are those systems with orbital periods  $P_{\text{orb}} \lesssim 80$  min, which is the minimum period for LMXBs with hydrogen-rich main sequence donors. In these ultracompact binaries (UCBs) the mass donor must be a non-degenerate hydrogen-deficient star or a white dwarf (e.g. Verbunt & van den Heuvel 1995). Currently eight such systems with measured orbital periods ( $P_{\text{orb}} = 11$ –50 min) are known (Ritter & Kolb 2003).

In the recent past, the existence of a group of five ultracompact systems with neon-rich white dwarf donors has been claimed based on X-ray spectral properties (Schulz et al. 2001; Juett et al. 2001; Juett & Chakrabarty 2003). The donors are then C/O or even O/Ne/Mg white dwarfs that have transferred a significant fraction of their mass to the neutron star, in contrast to the usual wisdom that the donors are the remains of He white dwarfs. This has caused new explorations of the formation of these systems (e.g. Yungelson et al. 2002). Our motivation for studying these systems is that the stripped donor

stars offer the possibility to probe the interior composition of white dwarfs, which depends on the interplay of gravitational settling and crystallization of chemical elements.

Three of these five Ne-rich systems belong to the above-mentioned eight UCBs with measured orbital periods, while two of them are believed to be UCBs because of their similar optical and X-ray properties. The class of Ne-rich UCBs consists of:

- (1) 4U 1626-67 ( $P_{\text{orb}} = 41$  min)
- (2) 4U 0614+091
- (3) 2S 0918-549
- (4) 4U 1543-624 ( $P_{\text{orb}} = 18$  min, Wang & Chakrabarty 2004)
- (5) 4U 1850-087 ( $P_{\text{orb}} = 20$  min).

4U 1626-67 may be regarded as the prototype of this class. The donor's Ne-rich C/O-WD nature is derived from X-ray and ultraviolet spectra that exhibit double-peaked emission lines that obviously stem from the accretion disk (Schulz et al. 2001; Homer et al. 2002).

The close relation of the other four objects (2)–(5) to 4U 1626-67 was based on extraordinary high Ne/O abundance ratios (when compared to the ISM value) measured from ASCA spectra of (3)–(5) and a Chandra spectrum of (2). The spectra exhibit photoelectric absorption edges of neutral O and Ne in the interstellar medium (ISM) along the

\* Based on observations made with ESO Telescopes at the Paranal Observatory under programme ID 72.D-0013(A).

line-of-sight, which is suspected to originate from expelled material close to the binary systems. New X-ray spectroscopic observations of (3) and (4) obtained with Chandra and XMM-Newton confirmed the ASCA results, although different values for the Ne/O enrichment have been obtained from a Chandra and a XMM-Newton spectrum of (4) (Juett & Chakrabarty 2003). In contrast to the ASCA measurement of (5), recent XMM-Newton and Chandra observations found no evidence of an unusual Ne/O ratio (Sidoli et al. 2005; Juett & Chakrabarty 2005). These apparently contradictory results can be attributed to a variable Ne I/O I ratio due to changes in the ionisation structure in the measured absorption columns that, however, are not understood (Juett & Chakrabarty 2005). Hence, this means that the measured Ne/O ratio does not reflect the donor composition. Although the orbital periods of these systems are below 80 min (or at least believed to be so small), this does not necessarily mean that they contain C/O donors. For example, the X-ray burst properties of the 4U 1820-30 ( $P_{\text{orb}} = 11$  min) suggest an He-WD donor in that ultracompact system (e.g. Strohmayer & Brown 2002). Another example are the relatively short X-ray bursts observed from (3) that even suggest H-burning of material accreted onto the neutron star (NS) (Jonker et al. 2001), while optical spectra suggest a C/O WD donor (Nelemans et al. 2004 and this work). A possible explanation is that the heavy elements (C, O, Ne) undergo spallation during accretion leaving H and He nuclei for thermonuclear burning on the NS (Bildsten et al. 1992). In a recent paper In't Zand et al. (2005) conclude that the Ne/O ratio and the X-ray burst properties are all best explained with an He-rich donor.

In conclusion, the only way to confirm that the four systems (2)–(5) – besides the prototype (1) – indeed contain C/O-rich donors, perhaps enriched with Ne, is by UV and/or optical spectroscopy. Nelemans et al. (2004) show that the optical spectra of (2)–(4) are devoid of hydrogen and helium emission lines, which are usually seen in H- or He-rich accreting systems. Their spectra exhibit low-ionisation C and O emission lines, most prominent in the brightest of these objects, 4U 0614+091. In this paper we present new optical spectra of this system that cover a larger wavelength interval. They confirm the earlier conclusion by Nelemans et al. (2004) that the emission lines arise from the C/O-dominated material that is probably located in the accretion disk and not in the X-ray heated face of the white-dwarf donor. We also present a first detailed optical spectrum of the prototype 4U 1626-67, which mainly shows weak oxygen emission lines and proves the H- and He-deficiency in this system, too. Nelemans & Jonker (2005) also performed VLT observations of this system (also in spring 2004) with a similar setup. They show a section of their spectrum and emphasize the similarity with 4U 0614+91.

In addition we present results from first attempts to model the observed spectra with non-LTE accretion-disk models. We derive upper limits for the H and He abundances and investigate the formation of neon lines. Detailed C and O line-formation calculations can already qualitatively explain the observed emission lines. The ultimate goal is to derive detailed abundances and other disk parameters from the observed line profiles.

**Table 1.** Log of the observations.

Date, UT	Grism	$T_{\text{exp}}$ (sec)	Airmass	Seeing (arcsec)
4U 0614+091				
2003 Nov. 04, 07:22:08	600B	1735	1.22	0.73
2003 Nov. 04, 07:54:57	600B	1735	1.20	0.78
2003 Nov. 03, 07:40:17	600R	1735	1.21	1.00
2003 Dec. 15, 06:25:42	600R	1735	1.28	0.52
2003 Dec. 15, 07:00:31	600R	1735	1.37	0.57
4U 1626-67				
2004 Mar. 23, 08:22:00	600B	1735	1.37	0.76
2004 Mar. 23, 09:01:42	600B	1735	1.36	0.77
2004 Mar. 21, 08:48:53	600R	1735	1.36	1.58
2004 Mar. 22, 08:19:40	600R	1735	1.37	0.87
2004 Mar. 22, 09:00:00	600R	1735	1.36	0.71
2004 Mar. 23, 07:41:51	600R	1735	1.40	0.57
EG 274				
2004 Mar. 23, 09:48:17	600B	50	1.05	0.67
2004 Mar. 23, 09:53:25	600R	40	1.05	0.67

The paper is organised as follows. We describe our observations in the following section. We then present our line identifications in Sect. 3. Section 4 contains a description of our disk model calculations and we summarise and conclude in Sect. 5.

## 2. Observations

We obtained optical medium-resolution long-slit spectra of 4U 1626-67 and 4U 0614+091. The V magnitude of both systems is 18.5 (Ritter & Kolb 2003). We used the FORS1 spectrograph attached to UT1 of ESO's Very Large Telescope (VLT) on Paranal in Chile. The slit width was 1''. We used two grisms (600B and 600R, the latter in combination with order separation filter GG435) and obtained spectra covering the regions 3600–6000 Å and 5400–7500 Å with a mean dispersion of 1.20 and 1.07 Å pix<sup>-1</sup>, respectively. Observations were performed in service mode between Nov. 2003 and Mar. 2004. Each target was observed at least twice, see Table 1 for details. For 4U 1626-67 the exposure time covers almost one orbital period so that any respective spectral variation is smeared out. The data were processed through the standard ESO reduction pipeline. In addition we performed a flux calibration using observations of the DA white dwarf EG 274 with the same instrumental setup. Since this flux standard was observed only once per wavelength range and since the science targets were mostly observed at different dates, this provides only a rough absolute flux calibration. For each object the spectra were co-added to obtain one final spectrum. The blue and red spectra are displayed in Figs. 1 and 2, respectively.

Archival spectra of 4U 1626-67 taken with the Hubble Space Telescope (HST) and the STIS instrument cover the complete UV/optical wavelength range (1150–10 000 Å). The FUV spectrum is described in detail by Homer et al. (2002)

K. Werner et al.: VLT spectroscopy of LMXBs 4U 0614+091 and 4U 1626-67

727

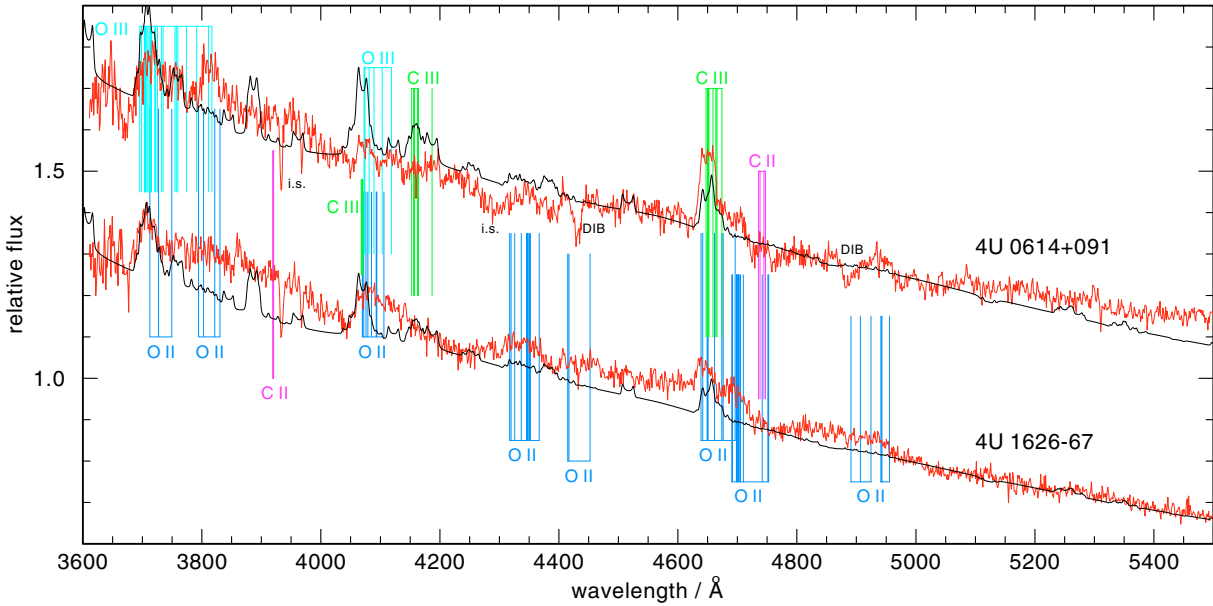


**Fig. 1.** Blue spectra of 4U 0614+091 and 4U 1626-67. H and He lines are lacking. The emission lines are identified as O II-III and C II-III (see also Table 2). All absorption features are of interstellar (i.s.) origin: Ca II 3934/3968 Å, the 4300 Å CH band, and two diffuse interstellar bands (DIB). Plotted over the two observed spectra is a synthetic accretion disk spectrum reddened with  $E(B-V) = 0.55$  and  $E(B-V) = 0.40$ , respectively.

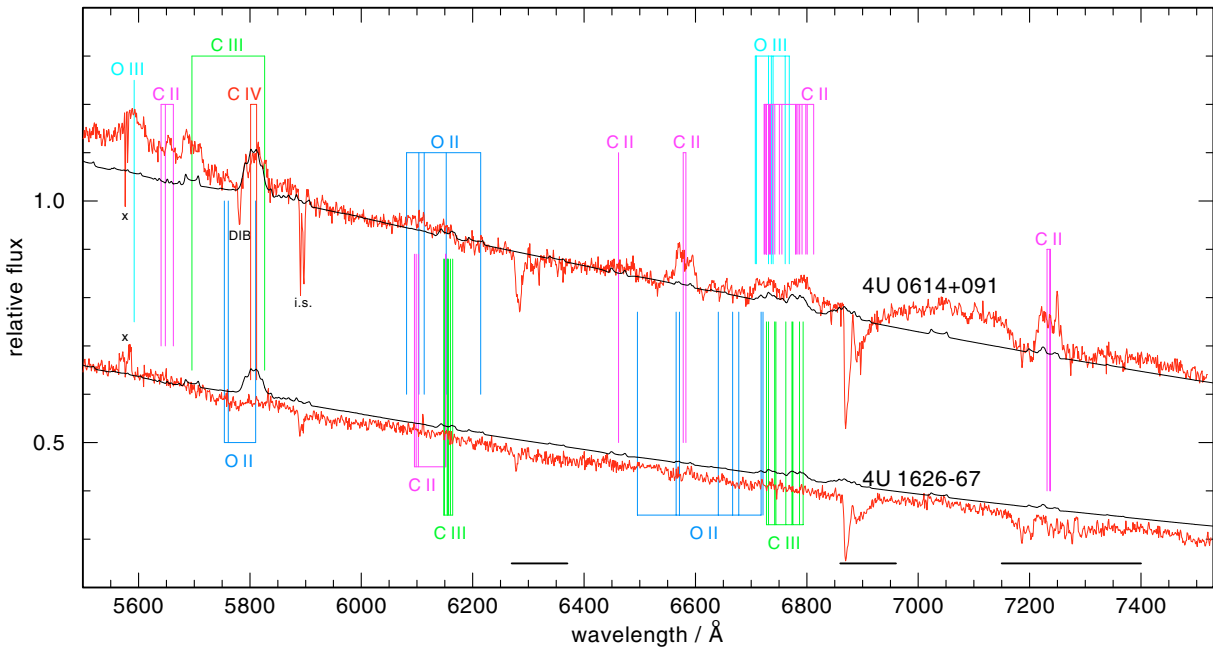


**Fig. 2.** Red spectra; 4U 0614+091 shows emission lines from C II-IV and O II-III, while the 4U 1626-67 spectrum is virtually featureless. All absorption features are either telluric (marked by horizontal bars) or of interstellar origin (Na I 5890/5896 Å and a DIB at 5780 Å). The features at 5575 Å are artifacts (“x”) due to an O I sky emission line. Overplotted is the synthetic accretion disk spectrum like in Fig. 1.

and a first comparison with synthetic accretion-disk spectra was presented by Werner et al. (2004). In Fig. 3 we compare the optical HST spectrum taken from the MAST archive with our VLT spectrum on an absolute flux scale. The blue and red sections of the VLT spectrum were scaled by a factor

of 1.65 and 1.45, respectively, to normalise them to the HST flux at 5600 Å. It is obvious that the VLT spectrum is not only weaker but also flatter than the HST spectrum. This can be attributed either to flux calibration problems or to source variability.

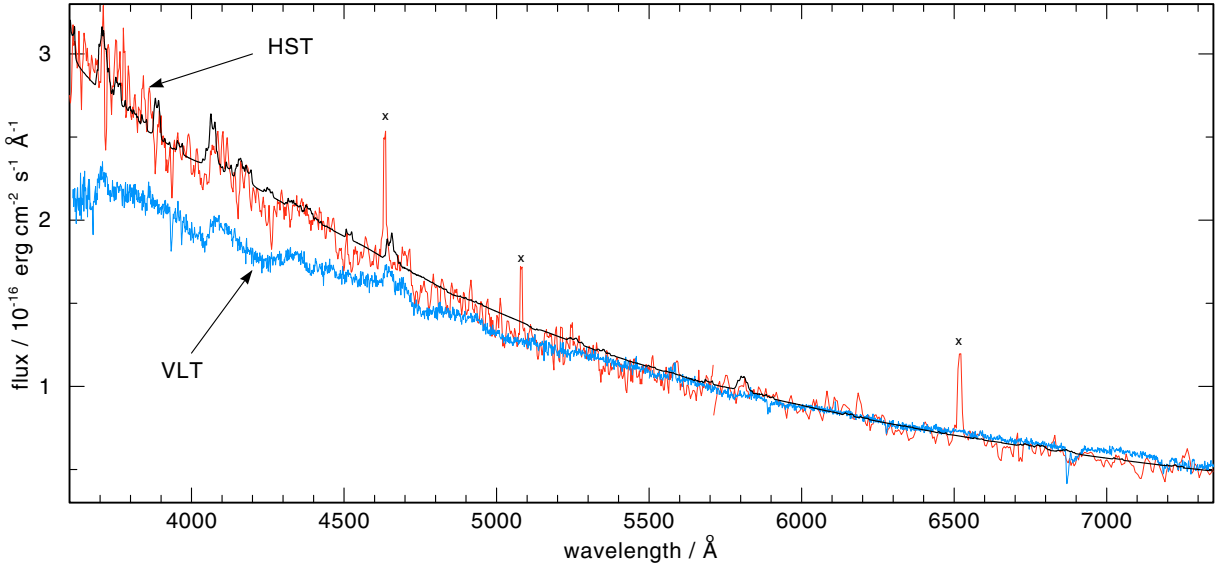


**Fig. 3.** Complete VLT spectrum of 4U 1626-67 compared to a spectrum taken with HST. The VLT spectrum, scaled to the HST spectrum at 5600 Å, is flatter possibly due to problems in absolute flux calibration. The HST spectrum has a poorer resolution and S/N-ratio, although some emission features at  $\lambda < 5000$  Å can be recognized in both datasets. Artificial emission spikes are marked by “x”. Overplotted is the synthetic accretion disk spectrum, like in previous figures, but now reddened with  $E(B - V) = 0.20$  to fit the continuum shape of the HST spectrum.

### 3. Line identification

Emission lines from hydrogen and helium are completely lacking in the VLT spectra of both systems. We detect neither Balmer lines nor lines from He I (e.g. 4471 or 5876 Å) or He II (e.g. 4686 Å), which are usually seen in optical spectra of interacting binaries. In the following two sections we discuss the line spectra of both systems in detail. Line identification is performed “by eye” without an equivalent-width estimation.

#### 3.1. 4U 0614+091

The spectrum of 4U 0614+091 shows numerous emission features that can be assigned to ionized carbon and oxygen, namely C II-IV and O II-III. The detected emission features are listed in Table 2 together with possible line identifications. Most features are blends of lines from at least two ions, making interpretation quite difficult, but some of them are probably unblended. These are the features at 5590 Å (O III), 5650 Å (C II), 5695 Å (C III), and 7235 Å (C II). The emission features at 4710 and 4940 Å are perhaps exclusively due to O II, but they are blends of four and two multiplets from this ion, respectively. Nelemans et al. (2004) present optical spectra of this star taken with VLT+FORST with slightly different wavelength coverage (4620–8620 Å). We essentially confirm the detection of their emission features and line identifications, however, our spectra extend to shorter wavelengths, down to 3600 Å, which allows us to detect some additional emission lines. On the other hand, we do not see four of the weak emission features identified in the Nelemans et al. (2004) spectra (at  $\lambda\lambda$  5140, 5190, 5280, and 6070 Å). This could be the consequence of line variability. In Fig. 4 we compare our single spectra of 4U 0614+091 in detail, and it is possible that the emission strength of the strongest

C II lines is variable on a time scale of weeks. In order to assess the significance of this variability, we simulated several times with different noise the strongest emission features observed on Nov. 3 and Dec. 15, applying the S/N ratio of the VLT spectra. We find a  $2\sigma$  probability that the variability is real. The line widths correspond to a projected rotational velocity of the order 1200 km s<sup>-1</sup>.

#### 3.2. 4U 1626-67

The spectrum of 4U 1626-67 clearly shows less features than does that of 4U 0614+091. Only five emission lines can be detected in the blue spectrum (see Table 2) and they are seen in both binaries. The red spectrum of 4U 1626-67 is virtually continuous. The strong C II emissions seen in 4U 0614+091 at 6580 Å and 7235 Å are lacking in 4U 1626-67. That could point to a higher ionisation of carbon in 4U 1626-67, although the C IV 5810 Å line is lacking, too. The presence of O II lines in the blue spectrum of 4U 1626-67 (e.g. at 4345 Å) also contradicts a higher ionisation, rather, it appears that the differences in the spectra of both binaries could be assigned to a different C/O ratio, being higher in 4U 0614+091. The entire set of emission lines in 4U 1626-67 could be due to oxygen alone, but in the UV spectrum C is clearly present (Homer et al. 2002). In addition, the line widths appear broader than in 4U 0614+091, however, this is difficult to quantify because of possible line blends and an uncertain identification of the continuum.

All absorption features seen in our optical spectra are either of interstellar origin or telluric. They are marked in Figs. 1 and 2.

**Table 2.** Emission features observed in the spectra of 4U 1626-67 and 4U 0614+091 and suggested line identifications. A plus sign in parentheses denotes an uncertain detection.

Feature (Å)	Observed in		Ion	Transition	Wavelength (Å)
	4U 0614+091	4U 1626-67			
3720	+	+	O III	3p <sup>3</sup> P – 3d <sup>3</sup> D <sup>o</sup>	3704–3732
			O III	3s <sup>5</sup> P – 3p <sup>5</sup> D <sup>o</sup>	3695–3735
			O II	3s <sup>4</sup> P – 3p <sup>4</sup> S <sup>o</sup>	3713–3749
3815	+		O II	3p <sup>2</sup> P <sup>o</sup> – 4s <sup>2</sup> P	3794–3830
			O III	3p <sup>1</sup> D – 3d <sup>1</sup> P <sup>o</sup>	3817
			O III	3s <sup>3</sup> P <sup>o</sup> – 3p <sup>3</sup> D	3755–3811
3920	(+)		C II	3p <sup>2</sup> P <sup>o</sup> – 4s <sup>2</sup> S	3919, 3921
4075			O II	3p <sup>4</sup> D <sup>o</sup> – 3d <sup>4</sup> F	4070–4111
			C III	4f <sup>3</sup> F <sup>o</sup> – 5g <sup>3</sup> G	4068–4070
			O III	3s <sup>3</sup> P – 3p <sup>3</sup> D <sup>o</sup>	4073–4119
4180	+		C III	4f <sup>1</sup> F <sup>o</sup> – 5g <sup>1</sup> G	4187
			C III	2p3p <sup>3</sup> D – 2s5f <sup>3</sup> F <sup>o</sup>	4153–4163
4345	+	+	O II	3s <sup>4</sup> P – 3p <sup>4</sup> P <sup>o</sup>	4317–4367
			O II	3s' <sup>2</sup> D – 3p' <sup>2</sup> D <sup>o</sup>	4347–4351
4410	+	(+)	O II	3s <sup>2</sup> P – 3p <sup>2</sup> D <sup>o</sup>	4415–4452
4650	+		C III	3s <sup>3</sup> S – 3p <sup>3</sup> P <sup>o</sup>	4647–4651
			C III	3s <sup>3</sup> P <sup>o</sup> – 3p <sup>3</sup> P	4651–4674
			O II	3s <sup>4</sup> P – 3p <sup>4</sup> D <sup>o</sup>	4639–4696
4710	+	+	O II	3p' <sup>2</sup> P <sup>o</sup> – 3d' <sup>2</sup> P	4691–4702
			O II	3p <sup>2</sup> D <sup>o</sup> – 3d <sup>2</sup> F	4699–4742
			O II	3p' <sup>2</sup> D <sup>o</sup> – 3d' <sup>2</sup> F	4698–4703
			O II	3p <sup>2</sup> D <sup>o</sup> – 3d <sup>4</sup> D	4710–4753
4745	(+)		C II	2s2p <sup>2</sup> P – 2s <sup>2</sup> 3p <sup>2</sup> P <sup>o</sup>	4735–4747
4940	+	(+)	O II	3p <sup>2</sup> P <sup>o</sup> – 3d <sup>2</sup> D	4941–4956
			O II	3p <sup>4</sup> S <sup>o</sup> – 3d <sup>4</sup> P	4891–4925
5590	+	(+)	O III	3s <sup>1</sup> P <sup>o</sup> – 3p <sup>1</sup> P	5592
5650	+		C II	3s <sup>4</sup> P <sup>o</sup> – 3p <sup>4</sup> S	5641–5662
5695	+		C III	3p <sup>1</sup> P <sup>o</sup> – 3d <sup>1</sup> D	5696
5810	+		O II	2p <sup>4</sup> <sup>2</sup> P – 3p' <sup>2</sup> D <sup>o</sup>	5754–5810
			C IV	3s <sup>2</sup> S – 3p <sup>2</sup> P <sup>o</sup>	5801, 5812
			C III	2s4d <sup>1</sup> D – 2p3d <sup>1</sup> F <sup>o</sup>	5826
6100	+		C II	3p <sup>2</sup> P – 3d <sup>2</sup> D <sup>o</sup>	6095–6103
			O II	3p <sup>2</sup> P <sup>o</sup> – 3s <sup>2</sup> S	6081, 6103
			O II	4s <sup>4</sup> P – 3s <sup>4</sup> S <sup>o</sup>	6113, 6153
6150	+		C III	2s4d <sup>3</sup> D – 2p3d <sup>3</sup> D <sup>o</sup>	6148–6164
			C II	4d <sup>2</sup> D – 6f <sup>2</sup> F <sup>o</sup>	6151
			O II	4s <sup>4</sup> P – 3s <sup>4</sup> S <sup>o</sup>	6113, 6153, 6214
6460	+		C II	4f <sup>2</sup> F <sup>o</sup> – 6g <sup>2</sup> G	6462
6580	+		C II	3s <sup>2</sup> S – 3p <sup>2</sup> P <sup>o</sup>	6578, 6583
			O II	3d <sup>2</sup> F – 4p <sup>2</sup> D <sup>o</sup>	6496, 6565, 6571
6730	+		C II	4d <sup>2</sup> D – 6p <sup>2</sup> P <sup>o</sup>	6723
			C II	3p <sup>4</sup> D – 3d <sup>4</sup> D <sup>o</sup>	6725–6755
			C III	3s <sup>3</sup> P <sup>o</sup> – 2p <sup>3</sup> D	6727–6773
6790	+		O II	3s <sup>2</sup> P – 3p <sup>2</sup> S <sup>o</sup>	6641, 6721
			O II	3d <sup>2</sup> P – 4p <sup>2</sup> P <sup>o</sup>	6667, 6678, 6718
			O III	4d <sup>3</sup> D <sup>o</sup> – 3s <sup>3</sup> D	6707–6768
7235	+		C II	3s <sup>4</sup> P <sup>o</sup> – 3p <sup>4</sup> D	6780–6812
			C III	2p3d <sup>3</sup> P <sup>o</sup> – 2s6s <sup>3</sup> S	6775–6793
7235	+		C II	3p <sup>2</sup> P <sup>o</sup> – 3d <sup>2</sup> D	7231–7237

#### 4. Exploratory disk models

We began the construction of accretion disk models to calculate synthetic spectra and report here on the current state of our

work. We use our accretion disk code AcDc, which is described in detail by Nagel et al. (2004). In essence, it assumes a radial  $\alpha$ -disk structure (Shakura & Sunyaev 1973). Then the disk is divided into concentric annuli. For each annulus we solve the

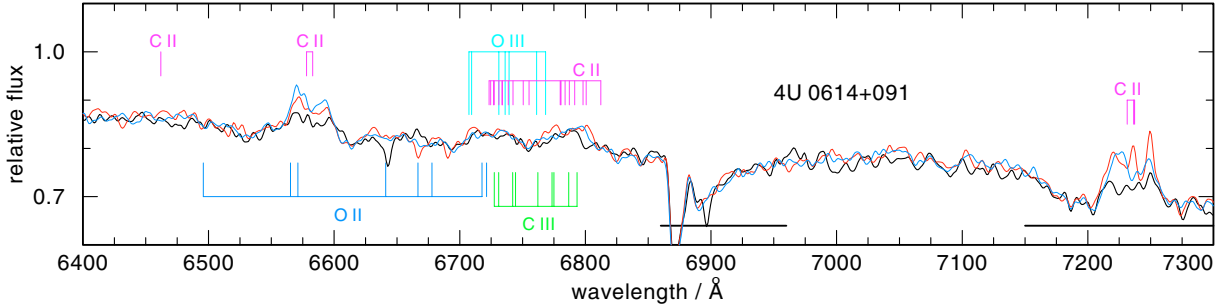


**Fig. 4.** Detail from three single spectra of 4U 0614+091. Thick line: spectrum taken on Nov. 03, 2003. Two thin lines: spectra taken consecutively on Dec. 15, 2003 (see Table 1). The strength of the two strongest emission features, the C II multiplets at 6580 Å and 7235 Å, show an increase over a time interval of several weeks.

radiation transfer equation (assuming plane-parallel geometry) together with the non-LTE rate equations for the atomic level populations, plus energy- and hydrostatic equations, in order to calculate a detailed vertical structure. The integrated disk spectrum is then obtained by co-adding the specific intensities from the individual annuli, accounting for inclination and Keplerian rotation.

It is not the aim of this paper to present a detailed fit to the emission line spectra of the two binaries. This requires extensive parameter studies that are extremely time consuming. We rather choose to calculate synthetic spectra from selected disk regions in which we believe the physical properties are representative for the formation of the observed optical spectra. This should at least give a rough idea of the relative strength of lines from different ionisation stages and, thus, is primarily thought to put our line identifications on firm ground. At present we neglect irradiation of the disk by the neutron star, because it would introduce new free parameters. We expect that the radial ionisation structure of the disk will be shifted to larger radii when irradiation is taken into account, but we hope that the relative line strengths are not affected to the extent that our identifications become completely wrong. Although the studied systems are strong X-ray sources, we do not see recombination lines from highly ionised species in the optical spectra as might be expected. It is conceivable that the outer parts of the disks in which the optical spectrum arises is shielded from X-ray irradiation by an inflated inner-disk region.

Since we do not compute the spectrum of the entire disk, we cannot expect to match the overall observed continuum flux, and we have already pointed out that there are problems with the absolute flux calibration. We use interstellar reddening as a free parameter in order to roughly fit the model to the observed flux level. The applied reddening is given in the figure captions.

The synthetic spectra presented here are based on the following choice of disk-model parameters. The central object is a neutron star with 10 km radius and a mass of  $1.4 M_{\odot}$ . The mass accretion rate is  $2 \times 10^{-10} M_{\odot}/\text{yr}$ . The disk extends from 1000 to 2000 stellar radii. The corresponding Keplerian velocities at these radii amount to 4300 and 3000 km s $^{-1}$ , and the effective temperatures to 47 000 K and 28 000 K,

**Table 3.** Summary of model atoms used in the disk model calculations. For each ion we list the number of NLTE levels and the number of line transitions. In brackets we give the number of lines in the wavelength range covered by our optical spectra after fine-structure splitting for detailed line-profile calculations.

Element	Ion	NLTE levels	Lines
H	I	10	45 (8)
	II	1	—
He	I	29	61 (16)
	II	14	91 (14)
C	III	1	—
	I	7	4 (0)
O	II	38	160 (42)
	III	58	329 (143)
	IV	9	17 (2)
	V	1	—
	I	1	—
Ne	II	29	82 (56)
	III	36	42 (47)
	IV	11	5 (0)
	V	6	4 (0)
	VI	1	—
Ne	I	3	0
	II	68	232 (49)
	III	4	0 (0)
	IV	1	—

respectively. The disk is divided into five annuli such that  $T_{\text{eff}}$  decreases almost linearly with radius steps. The inclination angle is set to 10°. The Reynolds number used to parametrise the disk viscosity was set to 10 000, which corresponds to  $\alpha \approx 0.5$ . The chemical composition is C = 50% and O = 50% (by mass).

For the opacity and emissivity calculations, it is essential to solve the non-LTE rate equations with detailed model atoms. Our main emphasis was put on the C II-III and O II-III ions. The number of non-LTE levels and radiative line transitions are summarised in Table 3. Level energies, oscillator strengths, and bound-free cross-sections for photoionisation are taken from

the Opacity Project (Seaton et al. 1994) TOPbase<sup>1</sup>. Electron collisional rates for (de-) excitation, ionisation, and recombination are computed with the usual approximate formulae. The neon model atom was taken from Dreizler (1993). For the final spectrum synthesis, fine structure splitting of atomic levels must be considered; level populations were taken from the models with appropriate statistical weights. Level energies were obtained from the NIST<sup>2</sup> database. The optical synthetic spectra finally include a total number of 377 lines from H I, He I-II, C II-IV, O II-III, and Ne II. They essentially contain most of the possible C and O line identifications given in Table 2, plus many others that turn out to be too weak to be seen in the rotationally broadened spectra.

As an example we present the vertical structure of the accretion disk model at a distance of 2000 stellar radii from the neutron star. The emergent flux at this location corresponds to  $T_{\text{eff}} = 28\,000$  K. Figure 5 shows the run of several quantities above the disk midplane on a column mass scale  $m$ . The Rosseland optical depth reaches unity at  $\log m = -0.9$ . Here the gravity amounts to  $\log g = 5.8$ . Mass and electron densities are  $6 \times 10^{-8} \text{ g cm}^{-3}$  and  $5 \times 10^{15} \text{ cm}^{-3}$ , respectively. Hence the physical conditions in the line-forming regions are comparable to those in the atmosphere of a subluminous B star. The vertical distribution of ionic fractions of C and O is shown in Fig. 6. There we also show the H, He, and Ne fractions that were taken from the test models that include these species in an amount of 10%. The dominant ionisation stages of oxygen at  $\tau_{\text{Ross}} = 1$  are O II and O III, giving rise to prominent emission lines of these ions in the spectra. In the case of carbon, C III dominates, closely followed by C II and C IV. This explains why we see lines from three C ions. The dominant neon ions in the line-forming regions are Ne II and Ne III. For helium we have He II dominating, followed by He I, so we would expect strong lines from these ions if neon and helium were abundant. Hydrogen is ionised by about 99.9%, but still, prominent emission lines are predicted if H were an abundant species (see below).

#### 4.1. C and O lines compared to observations

The synthetic spectrum is plotted together with the observed spectra in Figs. 1 and 2. Let us first consider 4U 0614+091. Generally, many of the observed features are also seen in the model, although they do not match the strength. This basically corroborates our line identifications. The C II lines of the model are too weak (e.g. at 6580 Å and 7235 Å), while the C III emissions are in some cases too weak (e.g. 4650 Å) or in other cases too strong (4180 Å). The C IV 5810 Å line matches well. The oxygen lines show a similar behaviour. The O II lines of the model are too weak (e.g. at 4940 Å). Some lines of O III match reasonably well (e.g. at 3720 Å), while others do not (e.g. at 5590 Å, which is much too weak in the model).

The model comparison with 4U 1626-67 confirms our ideas from the first inspection of the spectrum. The lines in the blue region can be explained qualitatively by the mere presence of oxygen lines. This, and the missing C IV 5810 Å line

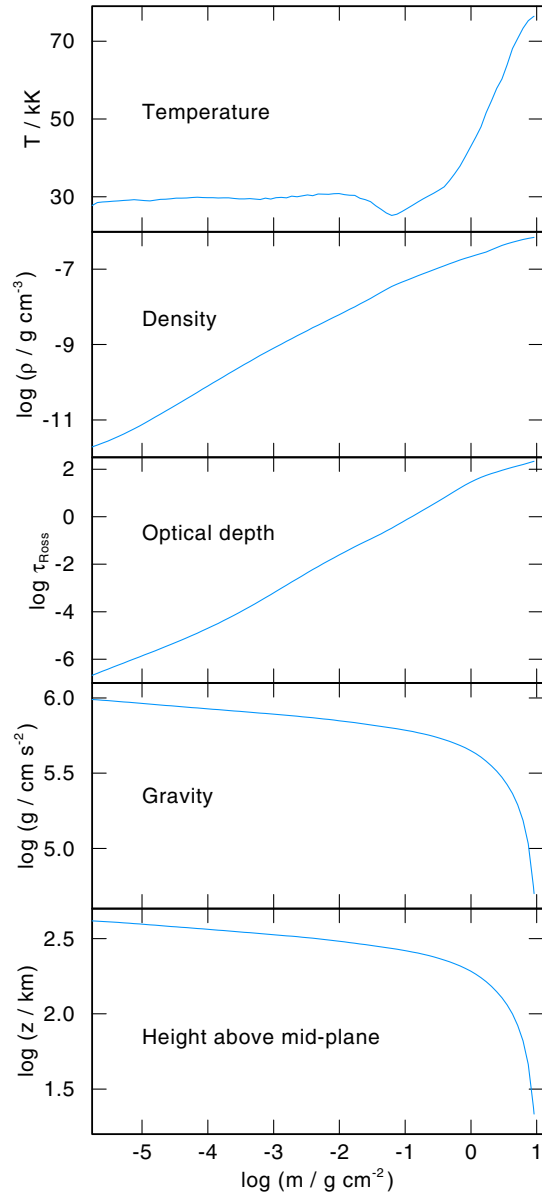


**Fig. 5.** Vertical structure of the C/O-disk model at a distance of 20 000 km from the neutron star. The emergent disk flux at this location corresponds to  $T_{\text{eff}} = 28\,000$  K. The physical variables are plotted against the column mass measured from the surface towards the mid-plane.

might originate in a relatively low C/O ratio when compared to 4U 0614+091.

It is disappointing that our NLTE disk model obviously gives a poorer fit to the observed line spectrum than the simple isothermal, constant-density, LTE slab model presented by Nelemans et al. (2004). However, that slab model can at best fit a limited spectral range, as it is emitted from a particular emission region with an assumed value for temperature and density and will never be able to simultaneously fit the observed spectra from the X-ray to the UV and optical ranges. In good agreement with the observation, our model exhibits lines from

<sup>1</sup> <http://vizier.u-strasbg.fr/topbase/topbase.html>

<sup>2</sup> <http://physics.nist.gov/>

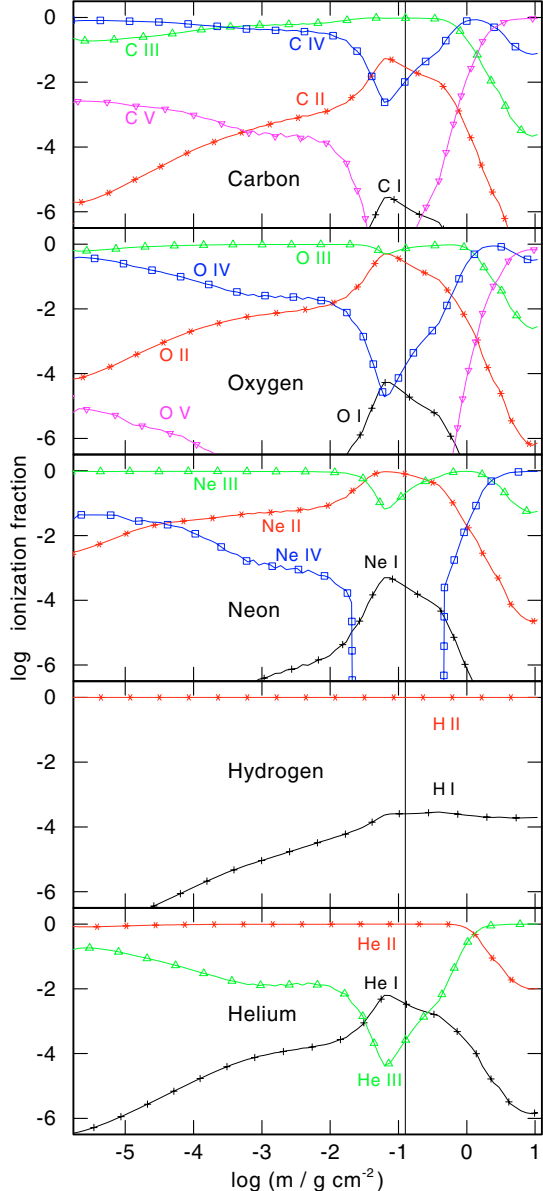


**Fig. 6.** Vertical ionisation stratification of chemical elements in the disk models at a distance of 20 000 km from the neutron star. The vertical line drawn at  $\log m = -0.9$  indicates  $\tau_{\text{Ross}} = 1$ .

three ionisation stages of carbon, indicating that temperature and density in the line-forming regions are reproduced reasonably well. The fact that the strength of many emission lines of a particular ion is either over- or underestimated may stem from drawbacks in the model atoms. One reason could be that the model ions are still too small and ignore the interlocking effects of neglected energy levels. A further extension of the model ions is hampered by the lack of atomic data, mostly oscillator strengths. Another reason for the poor line fits could be errors in the electron collisional rates. Only few are known from experiments or quantum mechanical calculations.

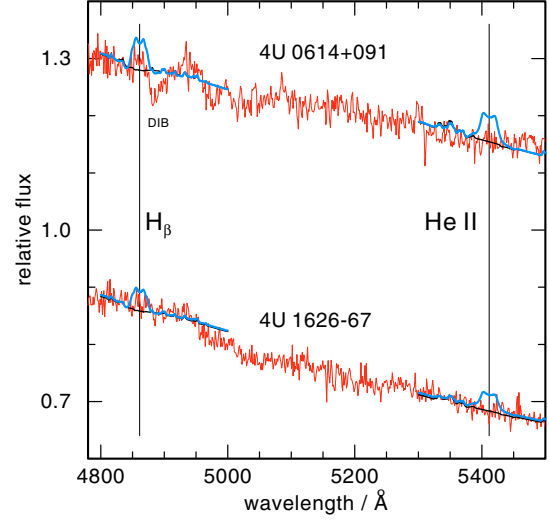


**Fig. 7.** Comparison of models with zero and 10% hydrogen and helium content to the observations. From the lack of  $H_{\beta}$  and  $He\text{ II}$  emission lines in the observed spectra, we conclude that the accretion disks are strongly H and He deficient. The model spectra were normalised to the local continuum flux.

These problems also might affect our neon line-formation calculations. However, the employed Ne model atom has been designed for the analysis of sdO stars and gave successful fits to observed Ne II lines (Dreizler 1993). Therefore we think that the predicted Ne emission lines in the model are more reliable than the majority of the C and O lines. Atomic data for H and He are accurately known and our model atoms have been employed with success to analyse many classes of stellar spectra, hence, we regard the computed line strengths of H and He as much more reliable than those of the metal lines. Another reason for the poor line fits might be that the assumed  $\alpha$ -disk does not describe the physics of the emitting region well.

#### 4.2. Limits on abundances of hydrogen, helium, and neon

The upper abundance limits we derive for H and He are regarded as realistic because of the above considerations, but the limit for neon is less secure.

In addition to the pure C/O disk model we also computed a model including 10% hydrogen and a model including 10% helium in order to see if this allows the H and He abundances to be constrained. In Fig. 7 we display the resulting emission lines of  $H_{\beta}$  and  $He\text{ II}$  5412 Å. From the lack of observed emission lines, it is evident that H and He are at most present at the 10% level. This excludes the possibility that the disks of 4U 1626-67 and 4U 0614+091 are dominated by hydrogen or helium and confirms the suspicion that they are in fact C/O-dominated.

We also computed a C/O model that includes 10% neon. It exhibits weak Ne II lines, but no such lines are detected in the VLT spectra (Fig. 8). We conclude that the neon abundance cannot be larger than  $\approx 10\%$ .

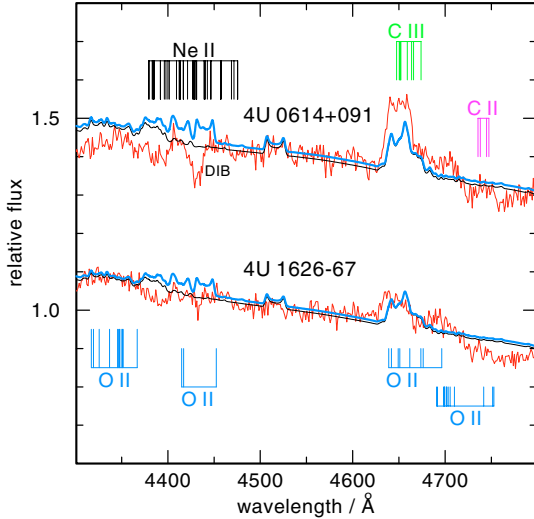


**Fig. 8.** Comparison of models with zero and 10% neon content to the observations. The model including neon exhibits weak Ne II lines in the region 4350–4450 Å, which cannot be detected in the observed spectra.

## 5. Summary

We have presented new high-quality optical spectra of the ultracompact low-mass X-ray binaries 4U 0614+091 and 4U 1626-67. They are pure emission line spectra and most probably stem from the accretion disk. The spectral lines are identified as due to C II–IV and O II–III. Line identifications are corroborated by first results from modeling the disk spectra with detailed non-LTE radiation transfer calculations. Hydrogen and helium lines are lacking and our models confirm the deficiency of H and He in the disk. Hence, the donor stars in these systems are in fact the eroded cores of C/O white dwarfs. There are indications that the O/C ratio in 4U 0614+091 is higher than in 4U 1626-67. This could suggest that the stripping process of the WD in 4U 0614+091 is more advanced.

It is hard to estimate the systematic error of the derived upper limit for the neon abundance so that the following conclusions are at the moment rather uncertain. From the lack of Ne II lines we find that the Ne abundance cannot exceed  $\approx 10\%$  or, in other words, the Ne/O ratio is at most of the order 0.2. The much higher Ne/O ratios ( $\approx 0.7$ ) derived from the ISM X-ray absorption edges of neutral Ne and O (Schulz et al. 2001; Juett et al. 2001) would produce detectable Ne II lines in the disk spectra. This confirms the conclusion of Juett & Chakrabarty (2005), that the determined ISM abundances of Ne and O are affected by ionisation effects and, hence, do not reflect the abundances of the donor stars.

For an initial solar metallicity the  $^{22}\text{Ne}$  abundance in an Ne-enriched crystallized and fractionated WD core can be estimated from theoretical models to  $\approx 0.07$ , but this value is very uncertain (Yungelson et al. 2002). It could be even higher by a factor of 3 (Isern et al. 1991). Such an Ne-rich core would have a mass of  $\approx 0.06 M_{\odot}$  (Yungelson et al. 2002). The mass of the WD donor in 4U 1626-67 is much smaller ( $0.01 M_{\odot}$ ; Yungelson et al. 2002). If we accept an upper limit of Ne = 0.1

for the observed neon abundance, then we may draw the following conclusion. Either the WD core has crystallized and fractionated, then our observation favors a relatively small Ne-enrichment as a result of the crystallization process. Or, if one accepts that fractionation would result in a high Ne abundance of 0.2 (unobserved), then the WD core in 4U 1626-67 had no time to crystallize which, depending on various details, lasts several Gyr (e.g. Hernanz et al. 1994).

Future work will concentrate on the disk modeling for the prototype 4U 1626-67, for which the observational database is the best of all such systems. Ultimately, the spectral properties (flux distribution and emission line strengths) over the complete wavelength range comprising spectral observations with Chandra, HST, and VLT, must be explained by a unique disk model.

*Acknowledgements.* T.R. is supported by the DLR under grant 50OR0201. We thank the referee for constructive criticism that helped to improve the paper.

## References

- Bildsten, L., Salpeter, E. E., & Wasserman, I. 1992, ApJ, 384, 143
- Cowley, A. P., Hutchings, J. B., & Crampton, D. 1988, ApJ, 333, 906
- Dreizler, S. 1993, A&A, 273, 212
- Hernanz, M., Garcia-Berro, E., Isern, J., et al. 1994, ApJ, 434, 652
- Homer, L., Anderson, S. F., Wachter, S., & Margon, B. 2002, AJ, 124, 3348
- In 't Zand, J. J. M., Cumming, A., Van der Sluys, M. V., Verbunt, F., & Pols, O. R. 2005, A&A, 441, 675
- Isern, J., Hernanz, M., Mochkovitch, R., & Garcia-Berro, E. 1991, A&A, 241, L29
- Jonker, P. G., van der Klis, M., & Homan, J. 2001, ApJ, 553, 335
- Juett, A. M., & Chakrabarty, D. 2003, ApJ, 599, 498
- Juett, A. M., & Chakrabarty, D. 2005, ApJ, 627, 926
- Juett, A. M., Psaltis, D., & Chakrabarty, D. 2001, ApJ, 560, L59
- Nagel, T., Dreizler, S., Rauch, T., & Werner, K. 2004, A&A, 428, 109
- Nelemans, G., & Jonker, P. G. 2005, in Interacting Binaries: Accretion, Evolution, and Outcomes, ed. L. Burderi et al., AIP Conf. Proc., 797, 396
- Nelemans, G., Jonker, P. G., Marsh, T. R., & van der Klis, M. 2004, MNRAS, 348, L7
- Ritter, H., & Kolb, U. 2003, A&A, 404, 301 (update RKcat7.4)
- Schulz, N. S., Chakrabarty, D., Marshall, H. L., et al. 2001, ApJ, 563, 941
- Seaton, M. J., Yan, Y., Mihalas, D., & Pradhan, A. K. 1994, MNRAS, 266, 805
- Shakura, N. I., & Sunyaev, R. A. 1973, A&A, 24, 337
- Sidoli, L., Parmar, A. N., & Oosterbroek, T. 2005, The INTEGRAL Universe, Proc. 5th INTEGRAL Workshop, ed. V. Schönenfelder, G. Lichti, C. Winkler, ESA SP-552, 389
- Strohmayer, T. E., & Brown, E. F. 2002, ApJ, 566, 1045
- Verbunt, F., & van den Heuvel, E. P. J. 1995, in X-ray Binaries, ed. W. H. G. Lewin, J. van Paradijs, & E. P. J. van den Heuvel (Cambridge: Cambridge University Press), 457
- Wang, Z., & Chakrabarty, D. 2004, ApJ, 616, L139
- Werner, K., Nagel, T., Dreizler, S., & Rauch, T. 2004, in IAU Coll. 194: Compact Binaries in the Galaxy and Beyond, ed. G. Tovmassian, & E. Sion, RevMexAA Conf. Ser., 20, 146
- Yungelson, L. R., Nelemans, G., & van den Heuvel, E. P. J. 2002, A&A, 388, 546

# Anhang D

## Non-LTE modeling of supernova-fallback disks

K. Werner, T. Nagel, and T. Rauch

### **Abstract**

We present a first detailed spectrum synthesis calculation of a supernova-fallback disk composed of iron. We assume a geometrically thin disk with a radial structure described by the classical  $\alpha$ -disk model. The disk is represented by concentric rings radiating as plane-parallel slabs. The vertical structure and emission spectrum of each ring is computed in a fully self-consistent manner by solving the structure equations simultaneously with the radiation transfer equations under non-LTE conditions. We describe the properties of a specific disk model and discuss various effects on the emergent UV/optical spectrum.

We find that strong iron-line blanketing causes broad absorption features over the whole spectral range. Limb darkening changes the spectral distribution up to a factor of four depending on the inclination angle. Consequently, such differences also occur between a blackbody spectrum and our model. The overall spectral shape is independent of the exact chemical composition as long as iron is the dominant species. A pure iron composition cannot be distinguished from silicon-burning ash. Non-LTE effects are small and restricted to few spectral features.

## Non-LTE modeling of supernova-fallback disks

Klaus Werner · Thorsten Nagel · Thomas Rauch

Received: 25 June 2006 / Accepted: 24 August 2006 / Published online: 22 March 2007  
 © Springer Science+Business Media B.V. 2007

**Abstract** We present a first detailed spectrum synthesis calculation of a supernova-fallback disk composed of iron. We assume a geometrically thin disk with a radial structure described by the classical  $\alpha$ -disk model. The disk is represented by concentric rings radiating as plane-parallel slabs. The vertical structure and emission spectrum of each ring is computed in a fully self-consistent manner by solving the structure equations simultaneously with the radiation transfer equations under non-LTE conditions. We describe the properties of a specific disk model and discuss various effects on the emergent UV/optical spectrum.

We find that strong iron-line blanketing causes broad absorption features over the whole spectral range. Limb darkening changes the spectral distribution up to a factor of four depending on the inclination angle. Consequently, such differences also occur between a blackbody spectrum and our model. The overall spectral shape is independent of the exact chemical composition as long as iron is the dominant species. A pure iron composition cannot be distinguished from silicon-burning ash. Non-LTE effects are small and restricted to few spectral features.

**Keywords** Radiative transfer; scattering · Neutron stars · Infall, accretion, and accretion disks

**PACS** 95.30.Jx · 97.60.Jd · 98.35.Mp

---

K. Werner (✉) · T. Nagel · T. Rauch  
 Institut für Astronomie und Astrophysik, Universität Tübingen,  
 Tuebingen, Germany  
 e-mail: werner@astro.uni-tuebingen.de

### 1 Introduction

Anomalous X-ray pulsars (AXPs) are slowly rotating ( $P_{\text{rot}} = 5\text{--}12$  s) young ( $\leq 100\,000$  yr) isolated neutron stars. Their X-ray luminosities ( $\approx 10^{36}$  erg/s) greatly exceed the rates of rotational energy loss ( $\approx 10^{33}$  erg/s). It is now generally believed that AXPs are magnetars with magnetic field strengths greater than  $10^{14}$  G and that their X-ray luminosity is powered by magnetic energy (Woods and Thompson 2006). As an alternative explanation the X-ray emission was attributed to accretion from a disk that is made up of supernova-fallback material (van Paradijs et al. 1995; Chatterjee et al. 2000; Alpar 2001). The fallback-disk model has difficulties to explain IR/optical emission properties of AXPs. When compared with disk models, the faint IR/optical flux suggests that any disk around AXPs must be very compact (e.g. Perna et al. 2000; Israel et al. 2004).

The discovery of optical pulsations in 4U 0142+61 which have the same period like the X-ray pulsations (Kern and Martin 2002) appears to be a strong argument against the disk model. It was argued that reprocessing of the pulsed NS X-ray emission in the disk cannot explain the high optical pulsed fraction, because disk radiation would be dominated by viscous dissipation and not by reprocessed NS irradiation (Kern and Martin 2002). Ertan and Cheng (2004), on the other hand, showed that these optical pulsations can be explained either by the magnetar outer gap model or by the disk-star dynamo model. Therefore, the observation of optical pulsations is not an argument against the disk model. A spectral break in the optical spectrum of 4U 0142+61 was discovered by Hulleman et al. (2004). This was also taken as an argument against the disk model because the authors do not expect such strong features from a thermally emitting disk. The recent discovery of mid-IR emission from this AXP (Wang et al. 2006), however, has strongly rekindled

the interest in studies of fallback-disk emission properties. While this mid-IR emission was attributed to a cool, passive (X-ray irradiated) dust debris disk by Wang et al. (2006) it was shown by Ertan on this conference that it can be explained with a model for an active, dissipating gas disk. If true, then the disk emission properties allow to conclude on important quantities, e.g., the magnetic field strength of the neutron star can be derived from the inner disk radius.

Independent hints for the possible existence of fallback disks come from pulsars with particular spin-down properties. For example, the discrepancy between the characteristic age and the supernova age of the pulsar B1757-24 was explained by the combined action of magnetic dipole radiation and accretion torques (Marsden et al. 2001). Even more, the presence of jets from pulsars such like the Crab and Vela can possibly be explained by disk-wind outflow interacting with and collimating the pulsar wind (Blackman and Perna 2004).

A fallback-disk model was proposed in order to explain the X-ray enhancement following a giant flare of the Soft Gamma Repeater SGR 1900+14 (Ertan and Alpar 2003). The X-ray light curve is interpreted in terms of the relaxation of a fallback disk that has been pushed back by the gamma-ray flare. This model can also explain the long-term X-ray and IR enhancement light curves of the AXP 1E 2259+58 following a major bursting epoch (Ertan et al. 2006).

The presence of a fallback disk around the stellar remnant of SN 1987A has been invoked in order to explain its observed lightcurve which deviates from the theoretical one for pure radioactive decay (Meyer-Hofmeister 1992). From the non-detection of any UV/optical point source in the supernova remnant, however, tight constraints for the disk extension can be derived (Graves et al. 2005).

To our best knowledge, the emission from fallback disks in all studies was hitherto modeled with blackbody spectra. In view of the importance of disk models for the quantitative interpretation of observational data it is highly desirable to construct more realistic models by detailed radiation-transfer calculations.

## 2 Radial disk structure

For the modeling we employ our computer code AcDc (Nagel et al. 2004), that calculates disk spectra under the following assumptions. The radial disk structure is calculated assuming a stationary, Keplerian, geometrically thin  $\alpha$ -disk (Shakura and Sunyaev 1973). As pointed out by Menou et al. (2001), for a comparison with observational data one probably has to use a more elaborate model, because near the outer disk edge the viscous dissipation and hence the surface mass density decline stronger with increasing radius than in an  $\alpha$ -disk. However, the purpose of the present paper is to

look for differential effects of various assumptions. Qualitatively, these effects can be expected to be independent of the detailed radial disk structure. In any case, it would be no problem to carry out the computations presented here with different radial structures.

The  $\alpha$ -disk model is fixed by four global input parameters: Stellar mass  $M_\star$  and radius  $R_\star$  of the accretor, mass accretion rate  $\dot{M}$ , and the viscosity parameter  $\alpha$ . For numerical treatment the disk is divided into a number of concentric rings. For each ring with radius  $R$  our code calculates the detailed vertical structure, assuming a plane-parallel radiating slab.

In contrast to a (planar) stellar atmosphere, which is characterized by  $T_{\text{eff}}$  and  $\log g$ , a particular disk ring with radius  $R$  is characterized by the following two parameters, which follow from the global disk parameters introduced above. The first parameter measures the dissipated and then radiated energy. It can be expressed in terms of an effective temperature  $T_{\text{eff}}$ :

$$T_{\text{eff}}^4(R) = [1 - (R_\star/R)^{1/2}]3GM_\star\dot{M}/8\sigma\pi R^3.$$

The second parameter is the half surface mass density  $\Sigma$  of the disk ring:

$$\Sigma(R) = [1 - (R_\star/R)^{1/2}]\dot{M}/3\pi\bar{w}.$$

$\sigma$  and  $G$  are the Stefan-Boltzmann and gravitational constants, respectively.  $\bar{w}$  is the depth mean of viscosity  $w(z)$ , where  $z$  is the height above the disk mid-plane. The viscosity is given by the standard  $\alpha$ -parametrization as a function of the total (i.e. gas plus radiation) pressure, but numerous other modified versions are used in the literature. We use a formulation involving the Reynolds number  $Re$ , as proposed by Kriz and Hubeny (1986). We chose  $Re = 15\,000$  which corresponds to  $\alpha \approx 0.01$ .

For the results presented here we selected the following input parameter values. The neutron star mass is  $1.4 M_\odot$ . The radii of the inner and outer disk edges are 2000 and 200 000 km, respectively. The disk is represented by nine rings or, more precisely, by nine radial grid points. The radiation integrated over the whole disk is then computed by assigning a weight to each point's spectrum that resembles the area fraction that it represents. The main characteristics of the disk at the radial grid points are given in Table 1. The mass-accretion rate was set to  $\dot{M} = 3 \times 10^{-9} M_\odot/\text{yr}$ . Figure 1 shows the radial run of  $T_{\text{eff}}$ . We also display the Keplerian rotation velocity for the later discussion of our results. The radial distance from the neutron star is expressed in units of the NS radius which is set to  $R_\star = 9.7$  km. But note from the above equations that the disk model is essentially independent of the stellar radius for large distances from the neutron star.

While  $\Sigma(R)$  and  $T_{\text{eff}}(R)$  in columns 3 and 4 of Table 1 follow from the  $\alpha$ -disk assumption, the quantities in the next

**Table 1** Characteristics of the nine rings that compose the disk model. Surface mass density  $\Sigma$  and emergent flux (expressed as  $T_{\text{eff}}$ ) follow from the  $\alpha$  disk prescription. The Rosseland optical depth  $\tau_{\text{Ross}}$  at the disk midplane, the mass density  $\rho$  and gravity  $\log g$  at optical depth unity follow from our computations of the detailed vertical ring structure. The last column denotes the fraction of the disk area that is made up by each ring model in order to compute disk-integrated spectra

Ring	$R$ [1000 km]	$\Sigma$ [g/cm <sup>2</sup> ]	$T_{\text{eff}}$ [1000 K]	$\log \tau_{\text{Ross}}^{\text{midplane}}$	$\log \rho(\tau_{\text{Ross}} = 1)$ [g/cm <sup>3</sup> ]	$\log g(\tau_{\text{Ross}} = 1)$ [cm/s <sup>2</sup> ]	% area fraction
1	2.0	2.9	305	3.1	-6.1	7.7	0.0025
2	2.5	2.8	258	3.2	-6.2	7.5	0.01
3	3.5	2.7	201	3.3	-6.4	7.2	0.034
4	6.0	2.6	135	3.5	-6.0	6.7	0.084
5	9.0	2.6	100	3.7	-5.9	6.4	0.19
6	14	2.5	72	3.3	-6.4	6.0	0.62
7	25	2.3	46	3.5	-6.9	5.5	1.70
8	40	2.2	33	3.9	-7.1	5.1	33
9	200	1.9	9.8	3.8	-7.6	3.6	64

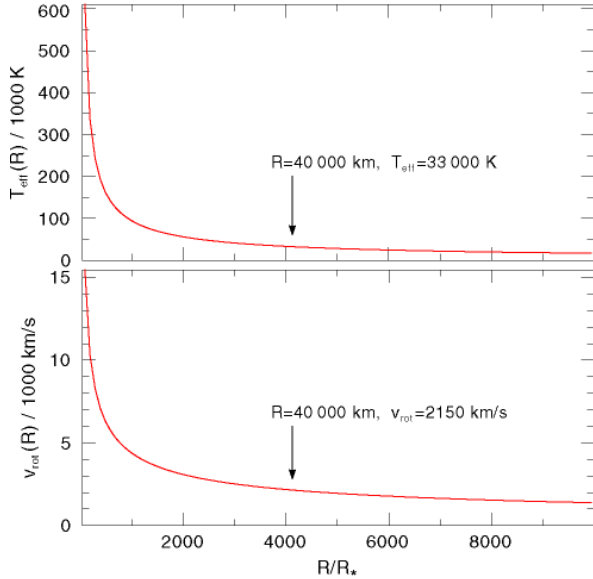


**Fig. 1** Radial disk structure: Effective temperature (top panel) and Keplerian rotation velocity (bottom panel). Arrows mark a reference point at a distance of  $R = 40000 \text{ km}$  (about 4000 stellar radii  $R_\star$ ) from the neutron star as discussed in the text

three columns are the result from our detailed vertical structure calculations described below. It shows that the entire disk model is optically thick. The Rosseland optical depth at the disk midplane  $\tau_{\text{Ross}}^{\text{midplane}}$  is  $> 1000$  at all radii. We also tabulate the mass density and the gravity at unity optical depth. That demonstrates that the conditions in the line forming regions of the disk resemble those in white dwarfs at the inner disk radii up to main sequence stars at the outer disk radii. The strength of Stark line broadening therefore strongly depends on the distance of the emitting region from the neutron star.

### 3 Vertical disk structure

The vertical structure of each disk ring is determined from the simultaneous solution of the radiation transfer equations plus the structure equations. The latter ones invoke radiative and hydrostatic equilibrium plus charge conservation. The structure equations also consist of the non-LTE rate equations for the atomic population densities. The solution of this set of highly non-linear integro-differential equations is performed using the Accelerated Lambda Iteration (ALI) technique (Werner and Husfeld 1985; Werner 1986; Werner et al. 2003).

The total observed disk spectrum, which depends on the inclination angle, is finally obtained by intensity integration over all rings accounting for rotational Doppler effects.

#### 3.1 Radiation transfer, hydrostatic and radiative equilibrium

We consider the radiation transfer equation for the intensity  $I_\nu$  at frequency  $\nu$ :

$$\mu \frac{\partial I_\nu(\mu, z)}{\partial z} = -\kappa_\nu(z) I_\nu(\mu, z) + \eta_\nu(z)$$

with the opacity  $\kappa_\nu$  and the emissivity  $\eta_\nu$ .  $z$  measures the geometrical height above the disk midplane and  $\mu$  is the cosine of the inclination angle  $i$ . The equation is solved using a short characteristics method. Opacities and emissivities are computed using atomic population densities that are obtained by solving the non-LTE rate equations. Our code allows for the irradiation of the disk by the central source, however, the results presented here are computed with zero incident intensity.

The radiation-transfer equations plus vertical structure equations are solved like in the stellar atmosphere case,

but accounting for two basic differences. First, the gravity (entering the hydrostatic equation for the total, i.e. gas plus radiation, pressure) is not constant with depth, but increases with  $z$ . The gravity is the vertical component of the gravitational acceleration exerted by the central object (self-gravitation of the disk is negligible):

$$g = zGM_{\star}/R^3.$$

Second, the energy equation for radiative equilibrium balances the dissipated mechanical energy and the net radiative losses:

$$9/4\rho wG\Sigma/R^3 = 4\pi \int_0^{\infty} (\eta_v - \kappa_v J_v) dv,$$

where  $\rho$  and  $J_v$  denote mass density and mean intensity, respectively. In the case of a stellar atmosphere the left-hand side of this equation vanishes and we get the usual radiative equilibrium equation. The solution is obtained by a generalized Unsöld-Lucy scheme and yields the vertical temperature structure.

Having calculated the vertical structures and spectra of the individual disk rings, the ring spectra are integrated to get the spectrum of the whole accretion disk:

$$I_v(i) = \cos(i) \int_{R_i}^{R_o} \int_0^{2\pi} I_v(i, \phi, r) r d\phi dr.$$

Here,  $R_i$  and  $R_o$  denote the inner and outer radius of the disk, and  $\phi$  is the azimuthal angle. At this stage, the Keplerian rotation velocity  $v_{\text{rot}}$  is taken into account by assigning a Doppler shift of  $\Delta v = \frac{v}{c} v_{\text{rot}} \sin \phi \sin i$  to the intensity emerging from a specific azimuthal ring sector.

### 3.2 Non-LTE rate equations

For each atomic level  $i$  the rate equation describes the equilibrium of rates into and rates out of this level and, thus, determines the occupation number  $n_i$ :

$$n_i \sum_{i \neq j} P_{ij} - \sum_{j \neq i} n_j P_{ji} = 0.$$

The rate coefficients  $P_{ij}$  have radiative and electron collisional components:  $P_{ij} = R_{ij} + C_{ij}$ . The radiative downward rate for example is given by:

$$R_{ji} = \left( \frac{n_i}{n_j} \right)^* 4\pi \int_0^{\infty} \frac{\sigma_{ij}(v)}{hv} \left( \frac{2hv^3}{c^2} + J_v \right) e^{-hv/kT} dv.$$

$\sigma_{ij}(v)$  is the photon cross-section and  $(n_i/n_j)^*$  is the Boltzmann LTE population ratio.

The blanketing by millions of lines from iron arising from transitions between some  $10^5$  levels can only be attacked with the help of statistical methods (Anderson 1989;

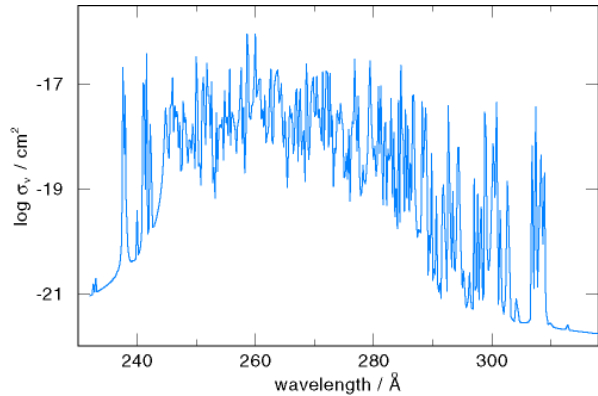


**Fig. 2** Photon cross-section for a superline in the Fe IV ion (between superlevels number 1 and 7)

Dreizler and Werner 1993). At the outset, model atoms are constructed by combining many thousands of levels into a relatively small number of superlevels. The respective line transitions are grouped into superlines connecting these superlevels. In this case, the population densities of the superlevels are computed from the rate equations, in which the photon cross-sections  $\sigma_{ij}(v)$  in the radiative rates  $R_{ij}$  do not contain only a single line profile but all individual lines that are combined into a superline. As an example we show such a cross-section in Fig. 2. The complete spectrum of our disk model ( $\lambda = 4$ – $300\,000$  Å) is sampled by 30 700 frequency points.

The model atoms that we have created for our disk calculations are summarized in Table 2. Most important is the iron model atom. It comprises the first eleven ionisation stages and a total number of more than 3 million lines. Atomic data are taken from Kurucz (1991) and the Opacity and Iron Projects (TIPTOPbase<sup>1</sup>).

### 3.3 Disk composition

The chemical composition of the supernova-fallback material in the disk is not exactly known. It depends on the amount of mass that goes into the disk. A disk with a small mass (say  $\leq 0.001 M_{\odot}$ ) will be composed of silicon-burning ash (Menou et al. 2001). For simplicity, the results presented here are obtained by assuming a pure-iron composition. It turns out that the emergent spectrum is insensitive against the exact composition as long as iron is the dominant species (Sect. 4.1). For a respective test run for one specific ring we assumed a composition that represents a silicon-burning ash. It contains iron (80% mass fraction) as well as silicon and sulfur by 10% each.

<sup>1</sup><http://vizier.u-strasbg.fr/topbase/>

**Table 2** Summary of non-LTE model atoms for silicon, sulfur, and iron. The numbers in brackets at the iron ions give the number of individual lines summed up into superlines. Employed for a specific test run, the silicon and sulfur model atoms are tailored to the conditions encountered in disk ring number 8

Element	Ion	NLTE levels	Lines
Si	III	6	4
	IV	16	44
	V	1	0
S	III	1	0
	IV	6	4
	V	14	16
Fe	VI	1	0
	I	7	(141 821)
	II	7	(218 490)
	III	7	(301 981)
	IV	7	(1 027 793)
	V	7	(793 718)
	VI	8	(340 132)
	VII	7	(86 504)
	VIII	7	(8 724)
	IX	7	(36 843)
	X	7	(45 229)
	XI	1	0

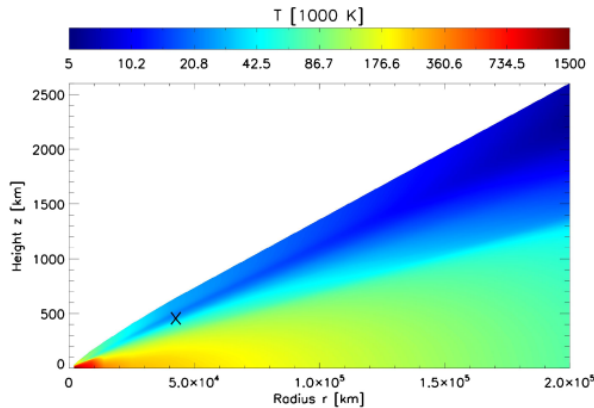


**Fig. 3** This cut perpendicular to the midplane shows the temperature structure of the disk. Note that the *vertical scale* (height above the midplane) is expanded. The height-to-radius ratio is about 0.015. The cross marks the depth at  $R = 40\,000$  km where  $\tau_{\text{Ross}} = 1$

### 3.4 Disk model properties

Figure 3 displays the temperature structure of the disk. The temperature varies between 1.5 million K at the midplane at the inner disk edge down to 6000 K in the upper layers at the outer disk edge. At all radii the vertical run of the temperature decreases almost monotonously with height above the

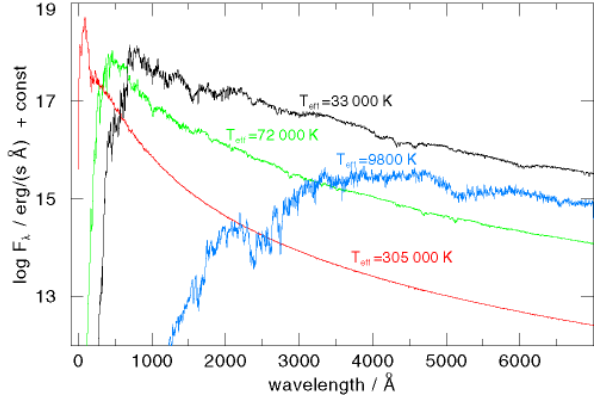


**Fig. 4** Relative contribution of single disk rings to the total disk flux. For clarity, we only show the fluxes from rings number 1, 6, 8, and 9. The flux from ring 8 at  $R = 40\,000$  km with  $T_{\text{eff}} = 33\,000$  K dominates the total disk spectrum at UV/optical wavelengths

midplane. A mild temperature reversal in the uppermost disk layers occurs. This turns out to be a non-LTE effect, because the respective LTE model has a strictly monotonous temperature run. We will discuss the consequences of this effect in Sect. 4.2.

Which disk regions contribute to the total disk spectrum and to what extent? In Fig. 4 we plot the emergent astrophysical flux from the area of four disk rings (rings 1, 6, 8, and 9, see Table 1), i.e., the computed flux per  $\text{cm}^2$  is weighted with the ring area. The spectral flux distribution of the innermost ring with  $T_{\text{eff}} = 305\,000$  K has its peak value in the soft X-ray region. The contribution of this innermost region to the optical/UV spectrum is negligible. Cutting off the disk at this inner radius ( $R = 2000$  km), therefore, is justified if this spectral range is of interest. The disk region that is dominating the UV/optical flux is represented by ring 8 with  $T_{\text{eff}} = 33\,000$  K. Its radius is 40 000 km, that is about 4000 neutron star radii. Its spectrum is dominated by strong blends of the numerous iron lines. Further out in the disk the effective temperature decreases and the flux contribution to the UV/optical spectrum decreases, too. Our outermost ring (number 9) has  $T_{\text{eff}} = 9800$  K, its flux maximum is at  $\lambda = 4000$  Å and it is fainter than the inner neighbor ring 8 over the whole spectral range. Cutting off the disk at this outer radius ( $R = 200\,000$  km) therefore does not affect the UV/optical spectral region.

## 4 Results

Because ring 8 is a representative disk region that determines the UV/optical spectrum, we will discuss its properties in more detail in the following three subsections, addressing the effects of chemical composition, non-LTE physics, and limb darkening on the spectrum. The radius of

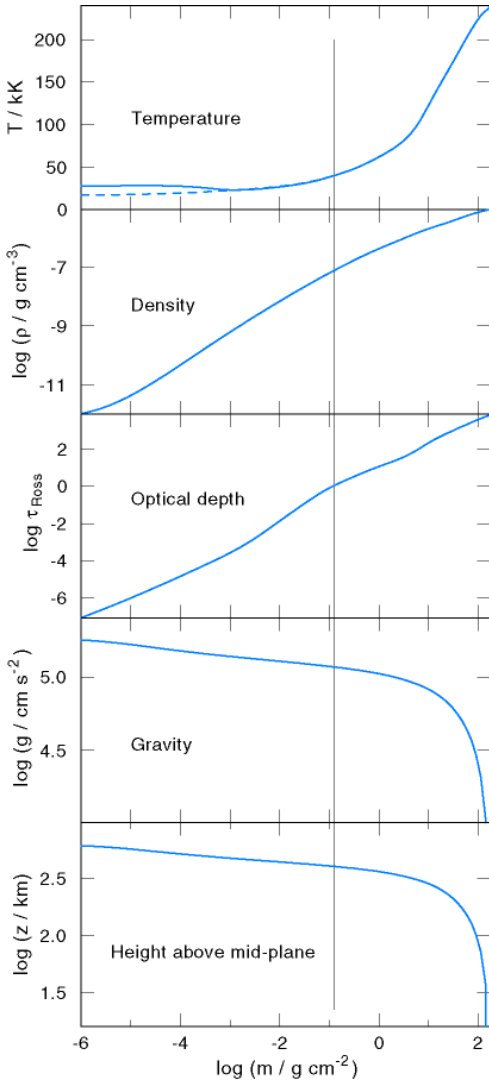


**Fig. 5** Vertical stratification of the disk at  $R = 40000$  km (ring 8,  $T_{\text{eff}} = 33000$  K). The quantities are plotted against the column mass density that is measured from the disk surface to the midplane (from left to right). The vertical line at  $\log m = -0.9$  denotes the depth where  $\tau_{\text{Ross}} = 1$ . The dashed curve in the top panel shows the temperature structure of a respective LTE model

this ring is marked by arrows in Fig. 1 and by a cross in Fig. 3.

In Fig. 5 we show the vertical structure of the disk at this radius ( $R = 40000$  km). We plot the run of several quantities on a column-mass scale, measured inward from the surface toward the midplane of the disk. The vertical line at  $\log m = -0.9$  marks the depth at which  $\tau_{\text{Ross}} = 1$ , i.e., the region of spectral line formation. The temperature shows a strong increase towards the midplane and, as already mentioned, a mild temperature reversal in the optically thin surface layers. Together with the temperature run,

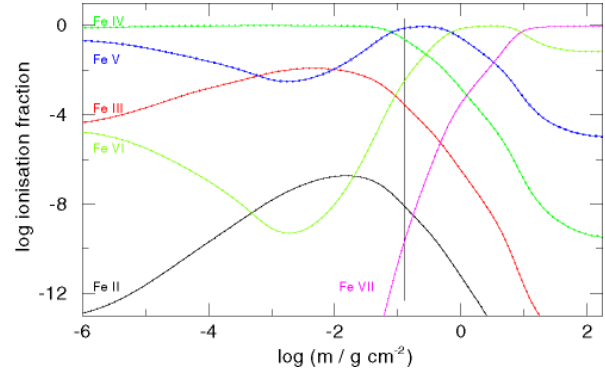


**Fig. 6** Vertical iron ionisation structure at  $R = 40000$  km (ring 8,  $T_{\text{eff}} = 33000$  K). The vertical line at  $\log m = -0.9$  denotes the depth where  $\tau_{\text{Ross}} = 1$ . The dominant iron opacities in the line forming regions are from Fe III–VI

the panels showing the mass density and gravity structure indicate that their values in the line forming region are comparable to those encountered in hot subdwarfs. The lowest panel shows that the disk height  $H$  at this distance from the NS is  $\approx 600$  km, i.e.  $R/H = 0.015$ .

In Fig. 6 we show the vertical ionisation structure of iron in the disk at  $R = 40000$  km. The dominant ionisation stages in the line forming regions are Fe III–VI. At the midplane Fe VII is dominant. The temperature at any depth is so high that Fe I–II do not significantly contribute to the spectrum.

#### 4.1 Effects of chemical composition

In Fig. 7 we show the flux spectrum of ring 8 in the wavelength range  $\lambda = 6200$ – $6500$  Å. It has been calculated for a pure iron composition as well as for a Fe/Si/S = 80/10/10 composition representing silicon-burning ash. The difference between the spectra is very small, because they are completely dominated by the extremely large number of iron lines. We conclude that the exact disk composition is not affecting the spectrum as long as iron is the dominant species.

While silicon and sulfur do not affect the overall spectrum by continuous background opacities, line features can be seen in the computed spectra, e.g. the Si IV resonance line in the UV. The line depth reaches about 50% of the continuum level but it would be difficult to detect even in medium resolution spectra when the disk inclination is high and the spectra are Doppler broadened by rotation.

#### 4.2 Significance of non-LTE effects

For our particular disk model we expect that non-LTE effects are not very large. This is because of the relatively high gravities in the line forming regions, ranging between  $\log g = 3.6$  in the outermost ring with  $T_{\text{eff}} = 9800$  K and

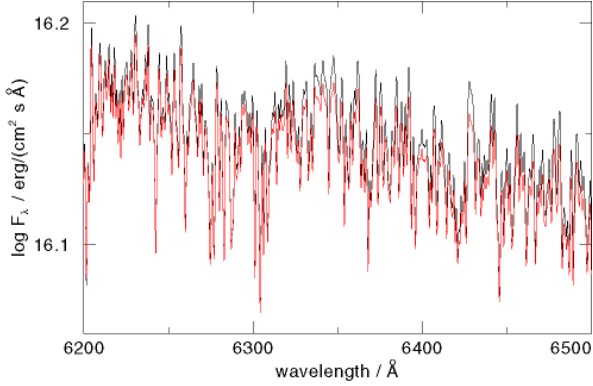


**Fig. 7** Detail from the emergent disk spectrum at  $R = 40\,000$  km (ring 8,  $T_{\text{eff}} = 33\,000$  K). We compare a pure iron composition (black line) with a silicon-burning ash composition (red line). The differences are marginal

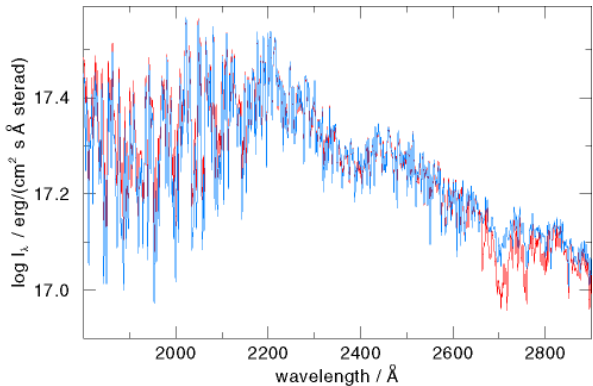


**Fig. 8** Comparison of LTE and NLTE emergent disk intensities (red and blue lines, respectively) at  $R = 40\,000$  km (ring 8,  $i = 87^\circ$ ,  $T_{\text{eff}} = 33\,000$  K)

$\log g = 7.7$  in the innermost region with  $305\,000$  K. In Fig. 8 we compare the spectra of an LTE and a non-LTE model of disk ring 8 in the wavelength range  $\lambda = 1800\text{--}2900$  Å, where the largest deviations were found. Indeed, non-LTE physics affects only narrow spectral regions. Only there, flux differences occur to an extent that the equivalent width of line blends changes by a factor of two. Accordingly, the temperature structures of both models deviate only in the uppermost layers of the disk (see top panel of Fig. 5) and, hence, only strong spectral lines that are still optically thick can be affected.

#### 4.3 Limb-darkening effects

Our model spectra show distinct limb-darkening effects. The situation is similar to the stellar atmosphere case (center-to-limb variation of the specific intensity). Looking face-on we see into deeper and hotter (and thus “brighter”) layers of the

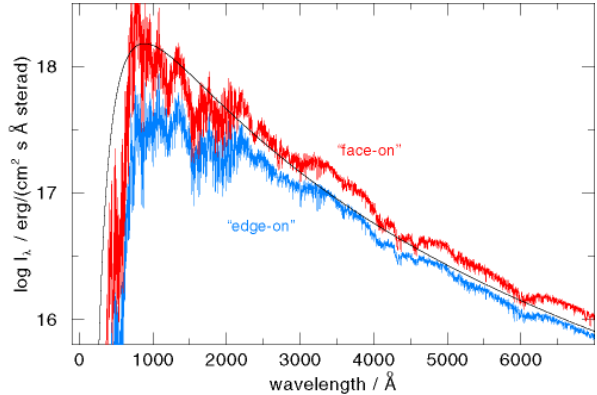


**Fig. 9** Effect of limb darkening: Specific intensity of the disk at  $R = 40\,000$  km (ring 8) seen under two inclination angles, namely  $87^\circ$  (i.e. almost edge-on, blue) and  $18^\circ$  (i.e. almost face-on, red). For comparison we also show a blackbody spectrum with  $T = T_{\text{eff}} = 33\,000$  K

disk when compared to a more edge-on view. In Fig. 9 we compare the specific intensity emitted by ring 8 (per unit area) for a high and a low inclination angle. Overall, the “edge-on” spectrum is roughly a factor of two fainter than the “face-on” spectrum in the optical region. The difference increases towards the UV and amounts to a factor of about three. We conclude that limb darkening effects are important when disk dimensions are to be estimated from magnitude measurements.

It is also interesting to compare the intensities with a blackbody spectrum (Fig. 9). Depending on the wavelength band, the blackbody over- or underestimates the “real” spectrum up to a factor of two in the optical and a factor of four in the UV.

#### 4.4 Rotational broadening

We have seen that the spectrum of an iron-dominated disk is characterized by strong blends of a large number of lines. At some wavelengths broad spectral features appear. It remains to be seen if Doppler effects from disk rotation smears out these features or if they could still be detectable. From the bottom panel of Fig. 1 we see that rotational broadening amounts to  $\approx \sin i \cdot 2000$  km/s at  $R = 40\,000$  km, corresponding to an orbital period of about two minutes. When seen almost edge-on, this rotational velocity is equivalent to a Doppler broadening of about  $\Delta\lambda = 25$  Å at  $\lambda 4000$  Å which clearly smears out any individual line profiles. In Fig. 10 we display the rotationally broadened spectrum of the entire disk model, seen under three different inclination angles. It is obvious that the broad line blends are so prominent that they do not disappear even for an almost edge-on view of the disk.

Among the strongest features is a 200 Å wide line blend at  $\lambda 1500$  Å with an absorption depth of about 50% relative to

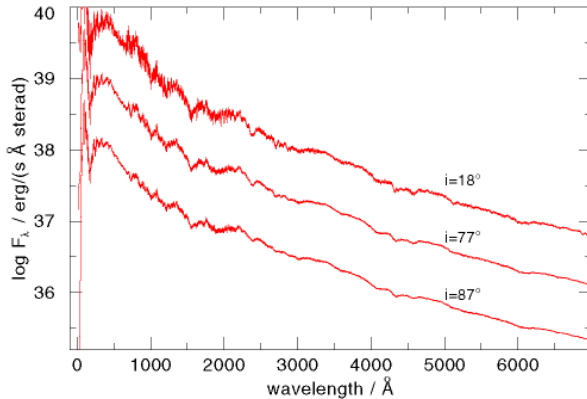


**Fig. 10** Complete disk spectrum including Kepler rotation broadening, seen under three inclination angles. The broad iron-line blends are detectable even in the almost edge-on case

the continuum. Should the disk be cooler, then disk regions with  $T_{\text{eff}} \approx 9000$  K could dominate the optical emission and the disk spectrum might look more like that emitted by ring 9 in our model (Fig. 4). Strong iron-line blanketing could cause a spectral break. This contrasts with a statement in Hulleman et al. (2004), where the spectral break observed in the optical energy distribution of the AXP 4U 0142+61 is suggested as an argument against disk emission.

## 5 Summary and outlook

We have computed a model for a supernova-fallback disk in order to study its structure and optical/UV emission properties. We assumed an  $\alpha$ -disk for the radial structure and performed detailed non-LTE radiation transfer calculations for the vertical structure and spectrum synthesis. The input parameters were:

Neutron star mass:  $1.4 M_{\odot}$

Inner and outer disk edge radii:  $R = 2000$  and  $200\,000$  km

Mass-accretion rate:  $\dot{M} = 3 \times 10^{-9} M_{\odot}/\text{yr}$ .

We have identified that the disk region in the vicinity of  $R = 40\,000$  km is the main contributor to the total disk spectrum at UV/optical wavelengths. We therefore investigated in some detail the disk properties at this radius.

We summarize our results as follows:

- The overall disk spectrum is independent of the detailed chemical composition as long as iron is the dominant species. In particular, a pure-iron composition is spectroscopically indistinguishable from a silicon-burning ash composition.
- The overall disk spectrum is hardly influenced by non-LTE effects, however, equivalent widths of individual line blends can change by a factor of two.

- Limb darkening affects the overall disk spectrum (in addition to the geometric foreshortening factor  $\cos i$ ). Depending on inclination and spectral band, the disk intensity varies up to a factor of three.
- Depending on the inclination, the disk flux can be a factor of two higher or lower compared to a blackbody radiating disk.
- Strong iron line blanketing causes broad ( $>100$  Å) spectral features that could be detectable even from almost edge-on disks. Disks that are cooler than our model (because of a lower mass-accretion rate) could even exhibit a spectral break in the optical band due to massive line blanketing.

We stress that these results hold strictly only for our particular disk model. In order to arrive at more general results a systematic parameter study (disk extent, accretion rate) of the disk emission is necessary. Also, it needs to be investigated in detail how fine the subdivision of the disk in a number of rings is necessary in order to achieve a computed spectrum with a certain accuracy. In addition, deviations from the  $\alpha$ -disk model must be studied. Another important point will be the inclusion of disk irradiation by the X-ray emission from the neutron star. This will reveal the relative importance of viscous dissipation and reprocessed irradiation that is discussed in the context of simultaneous optical and X-ray pulsations in the AXP 4U 0142+61. At the moment we do not dare to make any prediction how this affects the results presented here.

The innermost disk ring has a very high effective temperature and its flux distribution peaks in the soft X-ray band. It needs to be investigated systematically under which conditions (inclination, inner disk radius, accretion rate) the innermost disk regions can contribute to the thermal spectrum of the magnetars.

**Acknowledgements** T.R. was supported by the German Ministry of Economy and Technology through the German Aerospace Center (DLR) under grant 50 OR 0201.

## References

- Alpar, M.A.: *Apophys. J.* **554**, 1245 (2001)  
 Anderson, L.S.: *Apophys. J.* **339**, 558 (1989)  
 Blackman, E.G., Perna, R.: *Apophys. J.* **601**, L71 (2004)  
 Chatterjee, P., Hernquist, L., Narayan, R.: *Apophys. J.* **534**, 373 (2000)  
 Dreizler, S., Werner, K.: *Astron. Astrophys.* **278**, 199 (1993)  
 Ertan, Ü., Alpar, M.A.: *Apophys. J.* **593**, L93 (2003)  
 Ertan, Ü., Cheng, K.S.: *Apophys. J.* **605**, 840 (2004)  
 Ertan, Ü., Göögüç, E., Alpar, M.A.: *Apophys. J.* **640**, 435 (2006)  
 Graves, G.J.M., Challis, P.M., Chevalier, R.A., et al.: *Apophys. J.* **629**, 944 (2005)  
 Hulleman, F., van Kerwijk, M.H., Kulkarni, S.R.: *Astron. Astrophys.* **416**, 1037 (2004)  
 Israel, G.L., Rea, N., Mangano, V., et al.: *Apophys. J.* **603**, L97 (2004)



# Anhang E

Spectral modeling of gaseous metal disks around DAZ white dwarfs

K. Werner, T. Nagel, and T. Rauch

## Abstract

We report on our attempt for the first non-LTE modeling of gaseous metal disks around single DAZ white dwarfs recently discovered by Gänsicke et al. and thought to originate from a disrupted asteroid. We assume a Keplerian rotating viscous disk ring composed of calcium and hydrogen and compute the detailed vertical structure and emergent spectrum. We find that the observed infrared Ca II emission triplet can be modeled with a hydrogen-deficient gas ring located at  $R = 1.2 R_{\odot}$ , inside of the tidal disruption radius, with  $T_{\text{eff}} \approx 6000$  K and a low surface mass density of  $\approx 0.3 \text{ g/cm}^2$ . A disk having this density and reaching from the central white dwarf out to  $R = 1.2 R_{\odot}$  would have a total mass of  $7 \cdot 10^{21}$  g, corresponding to an asteroid with 160 km diameter.

## Spectral modeling of gaseous metal disks around DAZ white dwarfs

Klaus Werner, Thorsten Nagel and Thomas Rauch

Institute for Astronomy and Astrophysics, Kepler Center for Astro and Particle Physics,  
University of Tübingen, Germany

E-mail: [werner@astro.uni-tuebingen.de](mailto:werner@astro.uni-tuebingen.de)

**Abstract.** We report on our attempt for the first non-LTE modeling of gaseous metal disks around single DAZ white dwarfs recently discovered by Gänsicke et al. and thought to originate from a disrupted asteroid. We assume a Keplerian rotating viscous disk ring composed of calcium and hydrogen and compute the detailed vertical structure and emergent spectrum. We find that the observed infrared Ca II emission triplet can be modeled with a hydrogen-deficient gas ring located at  $R = 1.2 R_{\odot}$ , inside of the tidal disruption radius, with  $T_{\text{eff}} \approx 6000$  K and a low surface mass density of  $\approx 0.3 \text{ g/cm}^2$ . A disk having this density and reaching from the central white dwarf out to  $R = 1.2 R_{\odot}$  would have a total mass of  $7 \cdot 10^{21}$  g, corresponding to an asteroid with  $\approx 160$  km diameter.

### 1. Introduction: Dust around DAZ white dwarfs

More than two decades ago Zuckerman & Becklin (1987) announced the discovery of an IR excess around the DAZ white dwarf G29–38. The white dwarf itself is enriched in metals. Considering the short sedimentation timescales in the photosphere this implies that the star is accreting matter at a relatively high rate (Koester et al. 1997). Since no cool companion has been found at G29–38, the hypothesis was put forward that a dust cloud around the white dwarf causes the IR excess. In fact, the presence of dust has been confirmed by *Spitzer* observations (Reach et al. 2005). Graham et al. (1990) concluded that the dust is located in the equatorial plane. Subsequently, further DAZ white dwarfs with potential dust disks were found (Becklin et al. 2005, Kilic et al. 2005, 2006). As a possible origin of these disks tidally disrupted comets were discussed (Debes & Sigurdsson 2002) and, more likely because of the absence of H and He, disrupted asteroids (Jura 2003).

### 2. Gas disks around DAZ white dwarfs

Recently, signatures of a gas disk were discovered in Sloan Digital Sky Survey (SDSS) spectra of two DAZ white dwarfs (Gänsicke et al. 2006, 2007). The spectra display double-peaked emission lines of the infrared Ca II triplet  $\lambda\lambda 8498, 8542, 8662 \text{ \AA}$ .

In the present paper, we concentrate on one of these two white dwarfs, namely SDSS 1228+1040, because its emission line profiles are more prominent. The white dwarf's atmospheric parameters are  $T_{\text{eff}} = 22\,020$  K and  $\log g = 8.24$ . The derived stellar mass  $M_{\text{WD}} = 0.77 M_{\odot}$  and radius  $R_{\text{WD}} = 0.011 R_{\odot}$  are quantities that enter our disk model. The photospheric magnesium abundance is 0.8 times solar. The spectrum neither exhibits radial

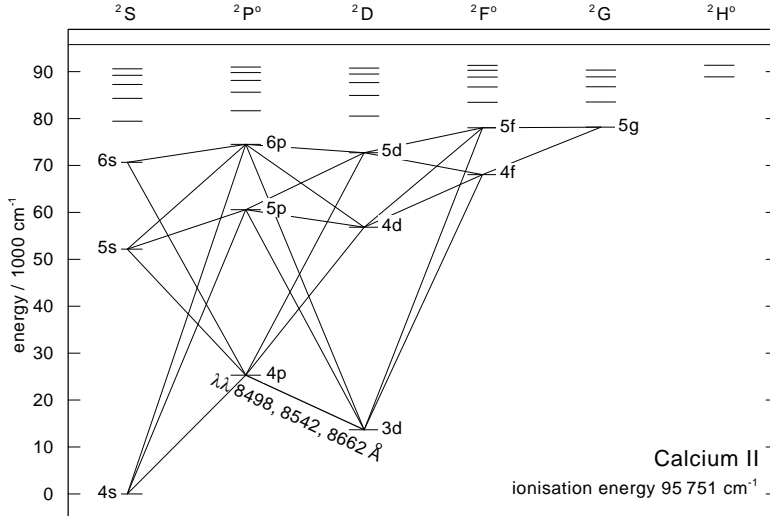


**Figure 1.** Grotrian diagram of our Ca II model ion. All highly excited levels that are not linked by radiative line transitions are treated in LTE. The 3d–4p transition causes the observed IR triplet.

velocity variations nor photometric variability. Besides the calcium emission lines only two other weaker emission features are seen (Fe II  $\lambda\lambda$  5018, 5169 Å). In particular, hydrogen and helium emissions are not discovered. It is concluded that the Ca and Fe emission lines stem from a metal-rich Keplerian disk around a single white dwarf. The Ca II line profiles are double peaked emission lines with a peak-to-peak separation of 630 km/s, i.e., the Keplerian rotation velocity is  $v \sin i = 315$  km/s. There is a clear violet/red asymmetry in the double-peaked profiles, well known from a similar phenomenon in Be star disks that is ascribed to one-armed spiral waves.

From a spectral analysis with a kinematical LTE emission model Gänsicke et al. (2006) conclude that we see a geometrically thin, optically thick disk at high inclination ( $i = 70^\circ$ ). The inner and outer disk radii are  $R_{\text{in}} = 0.64 R_\odot$  and  $R_{\text{out}} = 1.2 R_\odot$ , respectively. While the outer disk radius is quite sharply confined because of the steep line wings, the value derived for the inner disk radius possibly just marks the inner edge of the Ca II line emission region and not the physical inner disk edge, i.e.,  $R_{\text{in}}$  could reach down to the white dwarf's surface. They also conclude that the gas temperature in the disk is around 4500–5500 K. Since the tidal disruption radius for a rocky asteroid at the white dwarf is  $R \approx 1.5 R_\odot$ , it is possible that the material in the gas disk may be a disrupted asteroid whose dust was sublimated by the white dwarf's radiation field. It seems that SDSS 1228+1040 could be the hot counterpart to G29–38 and other cool DAZ stars harboring dust disks, but in the meantime DAZ white dwarfs with a dust disk and as hot as SDSS 1228+1040 were discovered (e.g., Jura et al. 2007).

It is our aim to compute a more realistic model for the gas disk around SDSS 1228+1040 and we are reporting here very first provisional results.

### 3. A viscous disk ring model

Basically we assume a Shakura & Sunyaev (1973)  $\alpha$ -disk model, i.e., a geometrically thin Keplerian disk heated by viscosity. For numerical calculations we employ AcDc, our *Accretion Disk code* that we developed for modeling disks in cataclysmic variables and low-mass X-ray binaries (Nagel et al. 2004). The code computes a detailed vertical structure and the spectrum of

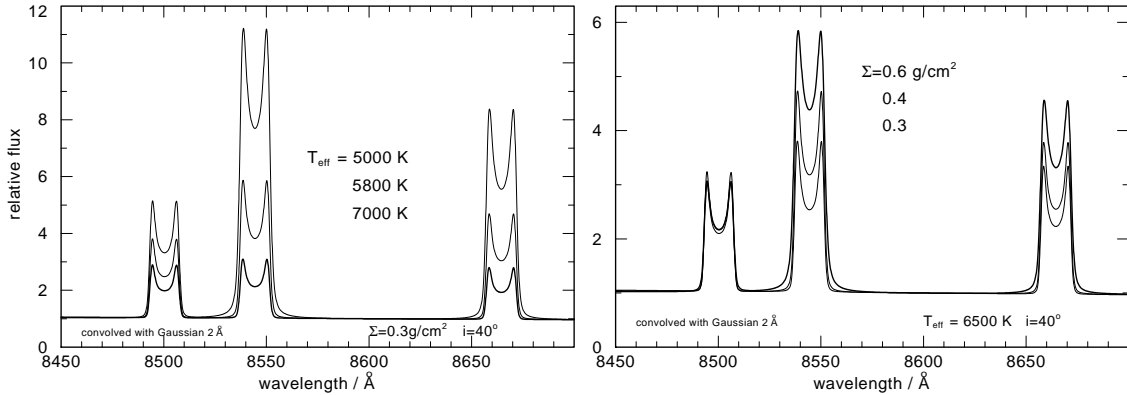


**Figure 2.** *Left:*  $T_{\text{eff}}$  dependence of the Ca II triplet emitted by a Keplerian rotating gas ring seen at an inclination angle  $i = 40^\circ$ . The emission becomes weaker with increasing  $T_{\text{eff}}$ . At the same time, the relative strengths of triplet components become equal. *Right:* A similar effect is seen when the surface mass density  $\Sigma$  decreases. Values for the ring parameters  $T_{\text{eff}}$  and  $\Sigma$  are given in the panels. All profiles are convolved with a 2 Å FWHM Gaussian.

a disk which is being built from radial-symmetric annuli. For any disk annulus we assume that it radiates like a plane-parallel slab in non-LTE, and in radiative and hydrostatic equilibrium. We are presenting here the results of a single disk ring using different values for the input parameters  $T_{\text{eff}}$  (as a measure for the viscously dissipated energy) and surface mass density  $\Sigma$  (the vertical mass column from the disk midplane to the surface). Further input parameters, which are kept fixed, are white dwarf's mass and radius as given above, and  $R_{\text{in}} = 91 \text{ R}_{\text{WD}}$  and  $R_{\text{out}} = 109 \text{ R}_{\text{WD}}$  for the inner and outer disk radii, respectively. The chemical composition is calcium dominated with an admixture of hydrogen with varying H/Ca abundance ratios in order to determine the extent of H-deficiency.

The principal problem for any modeling attempt is posed by the question: what heats the Ca II emission line region? Although being hot, it cannot be the white dwarf because it is too distant. Also, it cannot be gravitational energy released through viscosity because the required mass-accretion rate would be  $\approx 10^{-8} M_{\odot}/\text{yr}$  which is by many orders of magnitude larger than the accretion rate invoked for the presence of settling metals in DAZ photospheres ( $\approx 10^{-15} M_{\odot}/\text{yr}$ , Koester & Wilken 2006). A speculation by Jura (2008) is additional heating by energy dissipation through disk asymmetries, being driven by some external unseen planet. As mentioned above, such an asymmetry is obvious from the line profiles. Whatever, at the moment we do not know the heating mechanism. Therefore we need to use  $T_{\text{eff}}$  as a free parameter for the disk ring. *In praxi* this means that we set the accretion rate  $\dot{M}$ , which is related to  $T_{\text{eff}}$  through

$$T_{\text{eff}}^4(R) = [1 - (R_{\text{WD}}/R)^{1/2}] 3GM_{\text{WD}}\dot{M}/8\sigma\pi R^3,$$

to an artificially high value.

The calcium model atom used for the non-LTE calculations comprises three ionisation stages, Ca I – III with 7, 12, 1 non-LTE levels and 3, 26, 0 radiative line transitions, respectively. For the disk model calculations we do not account for level fine structure splitting. For the Ca II IR triplet this is done in the final formal solution of the transfer equation by distributing the level populations over the fine structure levels according to their statistical weight. Fig. 1 is a Grotrian diagram of our Ca II model ion with all implemented levels and lines, indicating the transition responsible for the observed IR triplet.

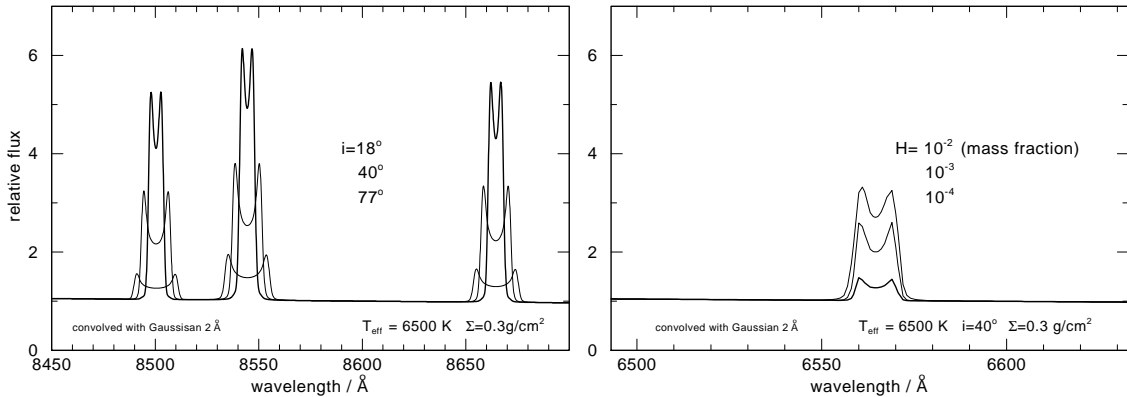


**Figure 3.** *Left:* The Ca II line shape of a particular model ( $T_{\text{eff}} = 6500 \text{ K}$ ,  $\Sigma = 0.3 \text{ g/cm}^2$ ) seen under different inclination angles  $i$ . The relative strength of the profile depression between double peaks increases with  $i$ . *Right:* H $\alpha$  line shape of the same model but with different hydrogen content. H > 1% would be detectable in SDSS 1228+1040.

Energy levels were taken from NIST, and oscillator strengths and photoionisation cross-sections from the Opacity and Iron Projects. Electron collisional rates are computed from usual approximation formulae. Rates for collisions with H are currently neglected, probably without consequences. That is because, first, Mashonkina et al. (2007) have shown that these collisions are unimportant in F/G type stars (having similar physical conditions in their photospheres) and, second, we are faced here with a H-deficient environment. Collisions of Ca with heavy ions are neglected, too. Their rates are unknown but probably unimportant because of the low thermal velocities of the perturbers. For the spectral lines we assume Voigt profiles with radiation damping parameters. Future improvement should include Van der Waals damping, although we don't expect it to be important in the disk environment. The hydrogen model atom is a standard configuration with ten non-LTE levels that we use routinely for stellar spectral modeling.

#### 4. Results

We present first results from disk ring models for SDSS 1228+1040, discussing:

- the influence of  $T_{\text{eff}}$ ,  $\Sigma$ , and inclination  $i$  on emergent line profiles of the Ca II IR triplet;
- an upper limit for hydrogen content from H $\alpha$ ;
- the characteristics of one representative model, in particular its vertical structure;
- a comparison of the computed spectrum with observation.

##### 4.1. Influence of $T_{\text{eff}}$ , $\Sigma$ , $i$ on the infrared Ca II triplet

In Fig. 2 (left panel) we see that the emission strength of the Ca II triplet decreases with increasing  $T_{\text{eff}}$  (with  $\Sigma = 0.3 \text{ g/cm}^2$  kept fixed). This is because of the shifting Ca II/Ca III ionisation balance. A closer comparison of the three triplet components shows that the relative strengths of the components become equal with increasing  $T_{\text{eff}}$ , a behaviour that constrains  $T_{\text{eff}}$  from the observed line strengths. A similar trend is seen (Fig. 2, right panel) when  $\Sigma$  is reduced (with  $T_{\text{eff}} = 6500 \text{ K}$  kept fixed). We stress that the models have a considerable continuum flux compared to line emission peak heights.

In Fig. 3 (left panel) we demonstrate that in principle the inclination angle can be constrained from the Ca II triplet line shape. Obviously, the relative strength of the profile depression between

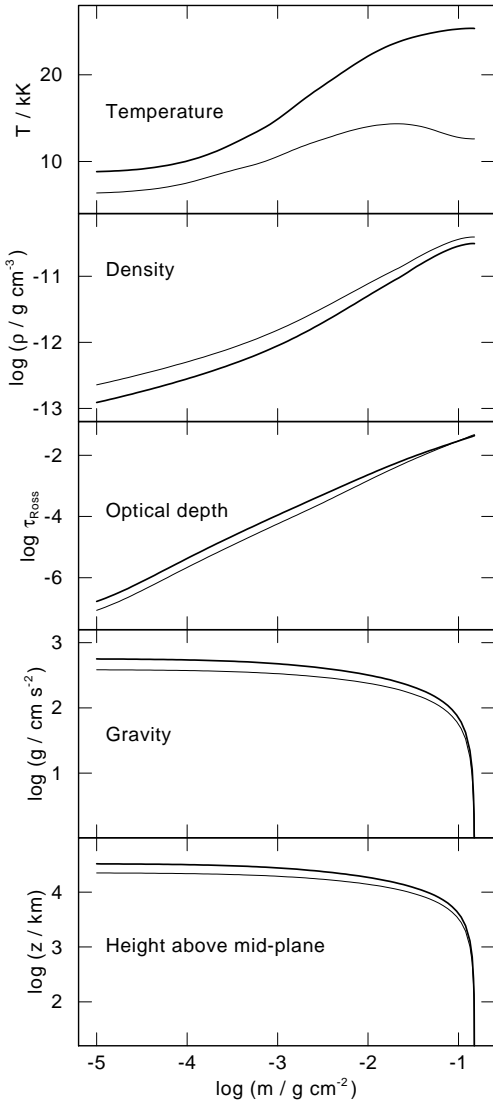


**Figure 4.** *Left:* Vertical structure of two models ( $T_{\text{eff}} = 5000\text{ K}$ , thick lines, and  $7000\text{ K}$ ) with  $\Sigma = 0.3\text{ g/cm}^2$ . The run of various physical quantities is shown on a column-mass scale measured from the disk surface (left) to the disk midplane (right); see discussion in the text (Sect. 4.3). The disks are optically thin ( $\tau_{\text{Ross}} < 0.1$ ).

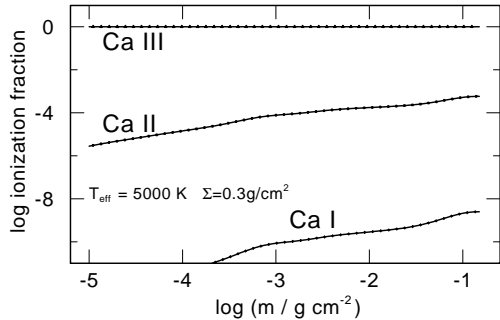


**Figure 5.** *Above:* Vertical run of the calcium ionisation fractions in the model with  $T_{\text{eff}} = 5000\text{ K}$  and  $\Sigma = 0.3\text{ g/cm}^2$ . Ca III is the dominant ionisation stage.

the double peaks increases with inclination.

#### 4.2. Upper limit for hydrogen

From the lack of H $\alpha$  emission in the spectrum of SDSS 1228+1040 we can make a quantitative estimate of the hydrogen-deficiency in the gas disk. Fig. 3 (right panel) depicts the H $\alpha$  line shape of a particular model in which we varied the H content (H = 1%, 0.1%, 0.01%; mass fraction). With an abundance of 1% the H $\alpha$  peak height is comparable to that of the Ca II triplet and, hence, would be detectable in the spectrum of SDSS 1228+1040.

#### 4.3. Vertical structure of disk ring

Let us inspect the vertical structure of two representative ring models with different effective temperature displayed in Fig. 4. The range of temperature  $T$  and mass density  $\rho$  is comparable to the circumstances encountered in the atmospheres of F/G-type giants. Accordingly, the gravity increases from the disk midplane toward the disk surface, up to  $\log g \approx 2.5$ . The run

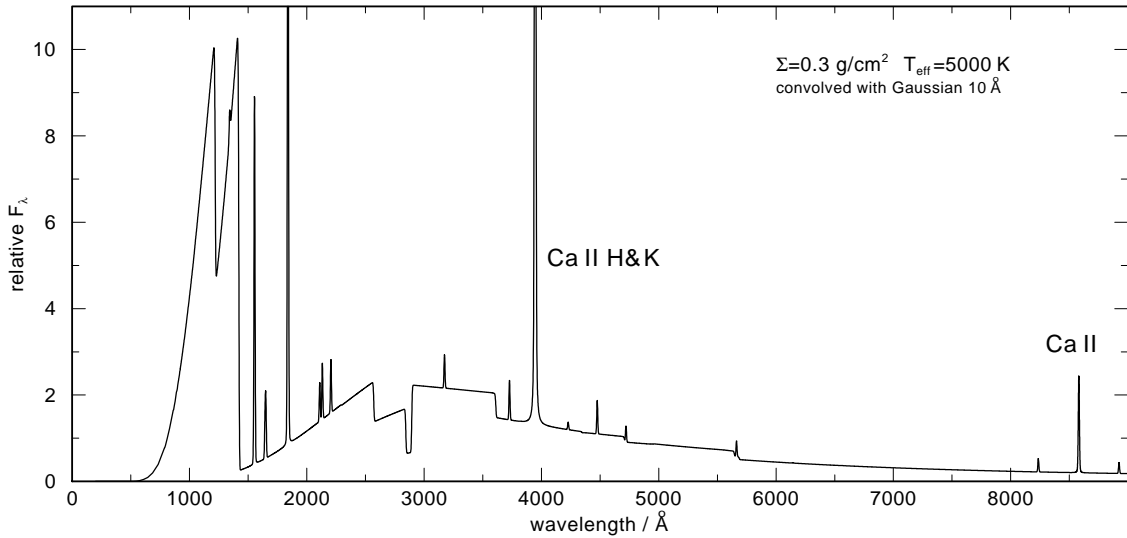


**Figure 6.** Flux distribution in the UV/optical range of the  $T_{\text{eff}} = 5000 \text{ K}$ ,  $\Sigma = 0.3 \text{ g/cm}^2$  model (no fine structure splitting applied to lines). The spectrum is dominated by Ca II emission lines and bound-free emission edges. The strongest feature is the H&K line. For the sake of clarity, the spectrum is convolved with a  $10 \text{ \AA}$  FWHM Gaussian.

of the Rosseland optical depth  $\tau_{\text{Ross}}$  shows that the disks are optically thin. The geometrical height  $z$  above the midplane shows that the thickness of the disk ring is about  $\Delta R = 50000 \text{ km}$ , hence,  $\Delta R/R \approx 15$ . The non-LTE departure coefficients (not plotted) of the atomic population numbers in these two models deviate significantly from the LTE value  $b = 1$ . For the lower levels of the Ca II IR triplet in the  $T_{\text{eff}} = 5000 \text{ K}$  model, for example, they range between  $b \approx 0.001$  in the upper layers of the disk and  $b \approx 50$  in deeper regions.

Fig. 5 shows the vertical calcium ionisation stratification for the cooler ( $T_{\text{eff}} = 5000 \text{ K}$ ) of these two models. Ca III is by far the dominant ionisation stage everywhere in the model. This advises us to extend the model atom to include the next higher ionisation stage in future calculations, although we do not expect a dramatic depopulation of Ca III (and Ca II) because its ionisation potential is rather high (50.9 eV).

It is interesting to look at the overall flux spectrum of the models, e.g., Fig. 6. The spectrum is dominated by Ca II emission lines. The Ca II H&K resonance doublet is by far the strongest emission feature that should be detectable in the spectrum of SDSS 1228+1040, although the WD flux increases by about an order of magnitude from the location of the IR triplet to the H&K line. A close inspection of the residual disk spectrum of SDSS 1228+1040 (i.e., observation minus WD model spectrum) presented by Gänsicke et al. (2008) indeed displays an emission feature at the location of the H&K line, although not explicitly described by the authors. In a new high-quality spectrum of SDSS 1228+1040 (Gänsicke, this meeting) the presence of this emission line is clearly confirmed. It seems, however, that the observed strength is strongly overestimated by our models, a result that also holds for the LTE emission models presented by Gänsicke.

Another remarkable feature of the overall model flux spectrum in Fig. 6 is the occurrence of two prominent Ca II *emission edges* at  $1219 \text{ \AA}$  and  $1420 \text{ \AA}$ , created by recombination processes into the first and second excited states, respectively. These features should be easily detectable in UV spectra as well as many other emission lines from other metals as predicted and presented

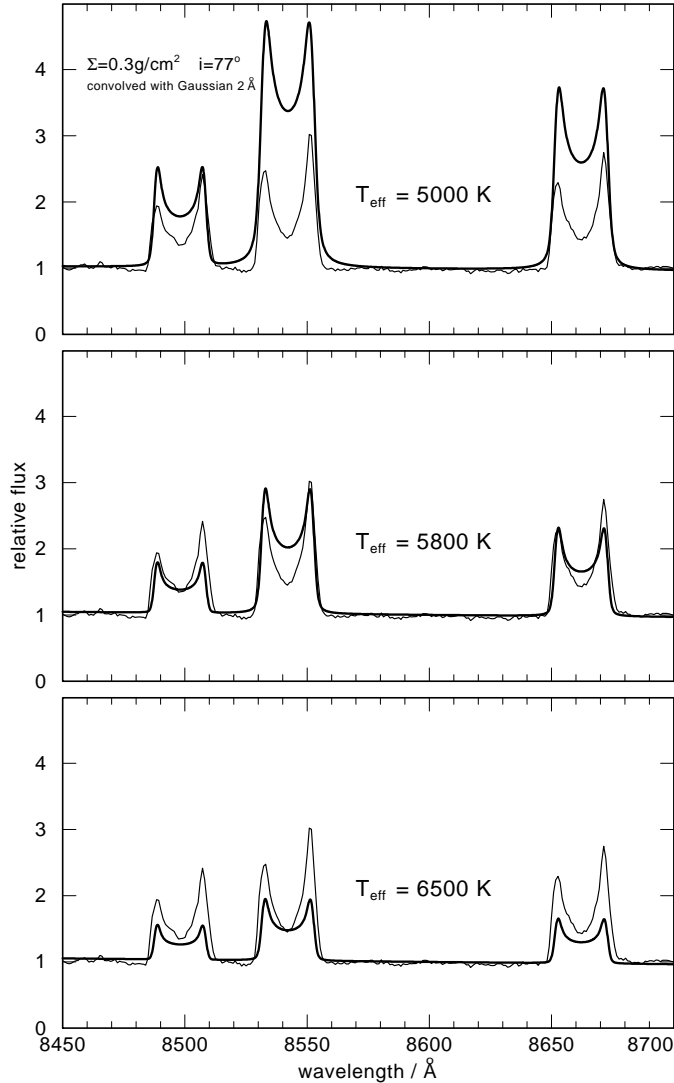


**Figure 7.** Normalized spectra of three models (thick lines) with different  $T_{\text{eff}}$  compared to the observed spectrum of SDSS 1228+1040. The fitting procedure is ambiguous because the observation is normalized to the continuum that is probably dominated by the white dwarf. All models have  $\Sigma = 0.3 \text{ g/cm}^2$  and are viewed at an inclination of  $i = 77^\circ$ .

by Gänsicke at this meeting. Our models promise that the proposed (and approved) HST/COS spectroscopic observation of SDSS 1228+1040 by Gänsicke and collaborators will deliver an exciting dataset that will allow important conclusions on the chemical composition of the gas disk.

#### 4.4. Models vs. observation

In Fig. 7 we show a direct comparison of the normalised spectrum of SDSS 1228+1040 to three models with different effective temperatures. This comparison is, however, complicated by the fact that Gänsicke et al. (2006) suggest that the continuous radiation in the vicinity of

the Ca II triplet stems from the white dwarf alone, while in contrast our models predict a non-negligible contribution by the disk. What we compare in Fig. 7 is the observed spectrum normalized to the WD (+disk) continuum and the computed disk spectrum alone, normalized to its emission continuum. In any case, it can be seen that the effective temperature of the disk at SDSS 1228+1040 is well constrained by the three models, being  $T_{\text{eff}} \approx 5800$  K. The cooler model ( $T_{\text{eff}} = 5000$  K) is perhaps more favorable because of the larger line-to-continuum emission ratio, while the hotter model ( $T_{\text{eff}} = 6500$  K) has the advantage that the relative strengths of the three line components are matched better.

## 5. Summary and conclusions

The infrared Ca II emission triplet in the spectrum of the DAZ white dwarf SDSS 1228+1040 can be modeled with a geometrically and optically thin, Keplerian viscous gas disk ring at a distance of  $1.2 R_{\odot}$  from the WD, with  $T_{\text{eff}} \approx 6000$  K and a low surface mass density  $\Sigma \approx 0.3 \text{ g/cm}^2$ . One serious open problem is the unknown disk-heating mechanism. The disk is hydrogen-deficient ( $H \leq 1\%$  by mass) and it is located within the tidal disruption radius ( $R_{\text{tidal}} = 1.5 R_{\odot}$ ). If one assumes that the disk reaches down to the WD and that it has uniformly this surface density, then its total mass would be  $7 \cdot 10^{21}$  g. A rocky asteroid ( $\bar{\rho} = 3 \text{ g/cm}^3$ ) with this mass would have a diameter of about 160 km. An asteroid of this size in our solar system is, e.g., 22 Kalliope.

Future work will include other abundant metal species, with a composition appropriate for asteroids. However, at the moment there are only two Fe II lines detected. Real progress for an abundance analysis of the gas disk around SDSS 1228+1040 is only possible with future UV spectroscopy.

While the determination of the composition of accreted material from abundance analyses in DAZ atmospheres is an indirect method that depends on our theoretical knowledge about metal settling timescales, the analysis of the gas disks has the obvious advantage that is a direct composition measurement.

## Acknowledgments

We thank Boris Gänsicke for sending us his SDSS 1228+1040 spectrum in electronic form and for useful discussions. T.R. is supported by the *German Astrophysical Virtual Observatory* project of the Federal Ministry of Education and Research (grant 05 AC6VTB).

## References

- Becklin E E Farihi J Jura M Song I Weinberger A J & Zuckerman B 2005 *ApJ* **632** L119
- Debes J H & Sigurdsson S. 2002 *ApJ* **572** 556
- Gänsicke B T Marsh T M Southworth J & Rebassa-Mansergas A 2006 *Science* **314** 1908
- Gänsicke B T Marsh T M & Southworth J 2007 *MNRAS* **380** L35
- Gänsicke B T Marsh T M Southworth J & Rebassa-Mansergas A 2008 *Preprint ArXiv:0710.2807v1*
- Graham J R Matthews K Neugebauer G & Soifer B T 1990 *AJ* **357** 216
- Jura M 2003 *ApJ* **584** L91
- Jura M Farihi J & Zuckerman B 2007 *ApJ* **663** 1285
- Jura M 2008 *AJ* **135** 1785
- Kilic M von Hippel T Leggett S K & Winget D E 2005 *ApJ* **632** L115
- Kilic M von Hippel T Leggett S K & Winget D E 2006 *ApJ* **646** 474
- Koester D & Wilken D 2006 *A&A* **453** 1051
- Koester D Provencal J & Shipman H L 1997 *A&A* **320** L57
- Mashonkina L Korn A J & Przybilla N 2007 *A&A* **461** 261
- Nagel T Dreizler S Rauch T & Werner K 2004 *A&A* **428** 109
- Reach W T Kuchner M J von Hippel T et al. 2005 *ApJ* **635** L161
- Shakura N I & Sunyaev R A 1973 *A&A* **24** 337
- Zuckerman B & Becklin E E 1987 *Nature* **330** 138